View metadata, citation and similar papers at core.ac.uk

brought to you by CORE

provided by Clemson University: TigerPrints

Clemson University
TigerPrints

All Dissertations | Dissertations

12-2009

Atom Scattering from Metals

William Hayes
Clemson University, wayne.hayes@gvltec.edu

Follow this and additional works at: https://tigerprints.clemson.edu/all_dissertations

 Part of the Physics Commons

Recommended Citation
Hayes, William, "Atom Scattering from Metals" (2009). *All Dissertations*. 458.
https://tigerprints.clemson.edu/all_dissertations/458

This Dissertation is brought to you for free and open access by the Dissertations at TigerPrints. It has been accepted for inclusion in All Dissertations by an authorized administrator of TigerPrints. For more information, please contact kokeefe@clemson.edu.

Atom Scattering from Metals

A Dissertation
Presented to
the Graduate School of
Clemson University

In Partial Fulfillment
of the Requirements for the Degree
Doctor of Philosophy
Physics

---

by
W. W. Hayes
December 2009

Accepted by:
Dr. J. R. Manson, Committee Chair
Dr. Murray Daw
Dr. Catalina Marinescu
Dr. Terry Tritt

Abstract

In the initial portion of this dissertation studies of Ar scattering from Ru(0001) at thermal and hyperthermal energies are compared to calculations with classical scattering theory. These data exhibited a number of characteristics that are unusual in comparison to other systems for which atomic beam experiments have been carried out under similar conditions. The measured energy losses were unusually small. Some of the angular distributions exhibited an anomalous shoulder feature in addition to a broad peak near the specular direction and quantum mechanical diffraction was observed under conditions for which it was not expected. Many of the unusual features observed in the measurements are explained, but only upon using an effective surface mass of 2.3 Ru atomic masses, which implies collective effects in the Ru crystal. The large effective mass, because it leads to substantially larger Debye-Waller factors, explains and confirms the observations of diffraction features. It also leads to the interesting conclusion that Ru is a metal for which atomic beam scattering measurements in the purely quantum mechanical regime, where diffraction and single-phonon creation are dominant, should be possible not only with He atoms, but with many other atomic species with larger masses.

A useful theoretical expression for interpreting and analyzing observed scattering intensity spectra for atomic and molecular collisions with surfaces is the differential reflection coefficient for a smooth, vibrating surface. This differential reflection

coefficient depends on a parameter, usually expressed in dimensions of velocity, that arises due to correlated motions of neighboring regions of the surface and can be evaluated if the polarization vectors of the phonons near the surface are known. As a part of this dissertation experimental conditions are suggested under which this velocity paramenter may be more precisely measured than it has been in the past.

Experimental data for scattering of argon, neon and xenon atoms from molten gallium, indium and bismuth surfaces are compared to calculations with classical scattering theory. The results of the theory are in reasonable agreement with observed energy resolved spectra taken at fixed angles, with in-plane angular distribution distributions, and with the first available out-of-plane angular distribution spectra for these systems. For all three of the rare gases, only scattering from liquid Ga required the use of an effective surface mass equal to 1.65 times the mass of a single Ga atom. The need for a larger effective mass has been noted previously for Ar/Ga scattering and is indicative of collective effects in the liquid Ga. Comparisons with data taken at low incident energies enables estimates of the physisorption well depth in the interaction potentials for many of the gas-metal combinations.

Surface corrugation is considered in a theory for which the surface corrugation amplitude is estimated from the temperature dependence of the most probable intensity for energy resolved scattering distributions. The theory is applied to an approximation for a sinusoidal surface corrugation. Final energy resolved spectra, in-plane and out-of-plane angular spectra are examined that exhibit reasonable agreement with data for scattering of rare argon from liquid metals. This establishes benchmark results for the behavior of this theory. Rainbow scattering is also considered.

Dedication

I would like to dedicate this dissertation to my wife for her support and encouragement.

Acknowledgments

I would like to thank Greenville Technical College for support through professional development funds. Haile Ambaye and Guoqing Fan have been good friends and very helpful colleagues. Finally, I would like to thank Dr. J. R. Manson for much patience and instruction during the lengthy process leading to this dissertation.

Table of Contents

List of Tables

List of Figures

Chapter 1

Introduction

The study of surfaces has been valued by civilization since the ancients practiced lecanomancy to foretell events [1]. Many important processes occur at the interface of solid, or liquid and gas phases. From the epitaxial growth of metal layers on substrates, to catalytic processes, to atmospheric drag on surfaces, the details of the atom-surface or molecule-surface interactions are important in modelling these processes that affect daily life.

This can be seen in the long line of researchers who have contributed to our understanding of the complicated processes at surfaces. Early on, in 1833, Faraday developed a theory of the reaction of hydrogen and oxygen in the presence of a platinum surface, or a catalytic reaction [2]. Braun advanced speculations on the rectification due to a thin surface layer at the interface of Cu and FeS in 1874 [3, 4]. Shortly thereafter, J. W. Gibbs completely deciphered the thermodynamics of surface phases [5] in 1877. Maxwell was the first to realize the significance of surface structure in the scattering process [6].

The first atom-surface scattering experiments were carried out by Stern [7, 8, 9, 10] and by Johnson [11, 12] after the discovery of quantum mechanics in the

early 1900's, using helium atoms. Aside from verifying important theoretical aspects of the wave nature of atoms, it was seen that important information about surfaces could be obtained. Around this time an early experimental attempt to understand atom-surface collisions was carried out by Roberts [13]. Quickly, the theory of the interaction of atoms and crystals was developed [14, 15]. Of historical significance, Langmuir was to receive the Nobel prize in 1932 for work in surface chemistry [16, 17, 18].

Lennard-Jones and coworkers submitted physisorption and chemisorption to scrutiny as well as critical and cooperative phenomena [19]. Bardeen elaborated the theory of the free metal surface in 1936 [20]. The international aspect of the study of the semiconductor surface is manifest in the study of the metal-semiconductor interface [21, 22, 23], as well as the interdisciplinary approach involving physics and chemistry.

While condensed matter physics and physical chemistry provided the tools, modern surface science sprang from the cooperation of technology and science and is thus a truly interdisciplinary science. During the 1960s, when surface science became a distinct research area, studying the surface was a difficult task. Prior to this time the ability to perform the necessary experimental measurements was hampered by the vacuum systems available [24]. According to Duke [25], ``The intrinsic interest in an empty box is limited, however difficult the task of emptying it may be. It is the new vistas in science and technology opened by the ability routinely to produce ultra-high vacua as a controlled environment that excite our interest.´´ Surface science was still a part of the physics and chemistry of materials.

Characterization of surfaces was enabled by the appearance of ultra-high vacuum technology coupled with the use of electron spectroscopy and time-of-flight machines. Reliable semiconductor devices gave rise to surface probes. The mystery of

low energy electron diffraction, or LEED, of backscattered electrons was sorted out. It was found that electrons elastically scattered by a solid must have scattered from the top few atomic layers of the sample [26, 27]. Now, a tool to probe the geometry of the surface was in hand. Also, the discovery of Laue [28] of x-ray diffraction by single crystals and the work of Bragg [29] eventually led to the study of structure functions of materials [30]. Inelastic x-ray scattering has been used in recent years to study the dynamic structure factor of liquid metals [31]. Many of the details of the further development of surface science were chronicled in [32]. The ultra-high vacuum technology also made possible the study of atomic beam-surface interactions.

In the study of atomic beam-surface interactions the energy exchange between an incident particle and a surface is of central interest in a great variety of experimental phenomena. Often, a significant portion of the incident translational energy may be lost on collision with the surface. The early experiments of Roberts [13] were measurements of the energy transfer between rare gas atoms and a tungsten surface, as well as effects of surface roughness. Jackson and Mott carried out calculations in what later became known as the single-phonon distorted wave Born approximation and were the first to describe energy transfer to the surface by that method [33, 34]. Lennard-Jones and co-workers also investigated the significance of the energy transfer to phonons, although the multi-phonon contributions they studied are now known not to be the dominant contribution to the energy exchange. Final energy and angular spectra give details of the exchange of translational energy and momentum. These phenomena range in incident energy from low energy, small mass atom, purely quantum mechanical interactions [35] to the classical realm of keV heavy ion scattering [36]. Also, the interaction of heavy neutral atoms with surfaces has been the subject of extensive experimental study [37, 38]. Of critical importance in interpretation of experimental results are theoretical descriptions of the many possible

beam-surface interactions.

Several approaches have been used in the theoretical description of projectile-surface interaction in the classical realm, which often involves the exchange of large numbers of quanta of energy. Originally, the methods used in neutron scattering were applied to particle-surface systems [39]. The molecular dynamics approach uses a computer simulation of the trajectories of the incident projectile as it interacts with the surface, the many-body aspects of the surface being treated in the simulation as well [40, 41, 42, 43]. The molecular dynamics approach often requires large amounts of computer time for even a modicum of success. It is also possible to use analytical methods [44, 45, 46, 47].

Analytical expressions may be derived for the energy resolved scattering intensities. Two different limiting solutions have been found, depending upon whether the surface is considered to be a collection of uncorrelated, discrete scattering centers, or a highly correlated smooth, vibrating surface. This surface can be considered to be the locus of classical turning points for the incident particle.

In this work is presented a theory and calculations of the interaction of an atomic beam with a corrugated surface. The theory is compared to several aspects of scattering from metal and liquid metal surfaces: energy resolved spectra, in-plane and out-of-plane scattering, temperature dependence, incident energy and angle dependence and the effect of mass ratio. The depth of the interaction potential well is estimated for the various gas-liquid metal systems that have been experimentally measured. The corrugation of the locus of classical turning points is estimated with this theory for the first time. This is accomplished by examination of the temperature dependance of the most probable intensity for the energy-resolved scattering spectra of the gas-liquid metal systems for which the necessary data were available. This is a relatively simple measurement that yields a valuable understanding of the nature

of the scattering surface. Out-of-plane scattering data is examined for this theory for the first time.

Chapter 2

Theory

2.1 Discrete and Continuum Models

The scattering of atomic and molecular particles has proven to be a useful method for obtaining a wide variety of information on the structure and dynamics of surfaces. In many cases such experiments are carried out under classical conditions involving a combination of large incident energies, heavy atomic masses and high surface temperatures, conditions for which large numbers of phonons are transferred in the collision process. In the classical scattering limit, two closed-form expressions for the differential reflection coefficient have been shown to be useful in explaining observed distributions of scattered particles, which typically consist of both total angular distributions and energy-resolved intensity spectra taken at fixed incident and final angles. The first of these expressions, called the discrete model, assumes that the incoming projectile collides with a surface of discrete atoms having an initial equilibrium distribution of thermal energies and whose vibrational motions are uncorrelated. Its differential reflection coefficient $dR(\mathbf{p}_f, \mathbf{p}_i)/d\Omega_f dE_f$, which expresses the fractional probability per unit final energy dE_f and per unit final solid angle $d\Omega_f$

of a beam of particles initially prepared with well defined momentum $\mathbf{p}_i$ making a transition to momentum state $\mathbf{p}_f$ after a single collision, is [39, 44, 48]

$$\frac{dR(\mathbf{p}_f,\mathbf{p}_i)}{d\Omega_f dE_f} = \frac{m^2\left|\mathbf{p}_f\right|}{8\pi^3\hbar^4 p_{iz}}|\tau_{fi}|^2\left(\frac{\pi}{k_B T_S \Delta E_0}\right)^{1/2}\exp\left\{-\frac{\left(E_f - E_i + \Delta E_0\right)^2}{4k_B T_S \Delta E_0}\right\}, \quad (2.1)$$

where p_{iz} is the surface normal component of $\mathbf{p}_i$, T_S is the surface temperature, k_B is Boltzmann's constant, the recoil energy is $\Delta E_0 = (\mathbf{p}_f - \mathbf{p}_i)^2/2M_C$ with M_C the surface atomic mass, m the mass of the incident atom, $E_{i,f} = p_{i,f}^2/2m$, and $|\tau_{fi}|^2$ is a form factor that depends on the interaction potential. If $|\tau_{fi}|^2$ is chosen to be a constant, the value appropriate for hard sphere scattering, then Eq. (2.1) contains no undefined parameters.

The second of these two expressions, called the smooth surface model, describes scattering from a potential which is on average flat but has vibration induced corrugations due to the thermal motions of the underlying atoms. Its differential reflection coefficient is given by [45, 46, 47, 48]

$$\frac{dR(\mathbf{p}_f,\mathbf{p}_i)}{d\Omega_f dE_f} = \frac{m^2 v_R^2\left|\mathbf{p}_f\right|}{8\pi^3\hbar^2 p_{iz} S_{u.c.}}\left|\tau_{fi}\right|^2\left(\frac{\pi}{k_B T_S \Delta E_0}\right)^{3/2}\exp\left\{-\frac{\left(E_f - E_i + \Delta E_0\right)^2 + 2v_R^2\mathbf{P}^2}{4k_B T_S \Delta E_0}\right\}, \quad (2.2)$$

where S_{uc} is the area of a surface unit cell and $\mathbf{P}$ is the projection of the scattering momentum $\mathbf{p_f} - \mathbf{p_i}$ parallel to the surface. The differences with respect to Eq. (2.1) are the appearance of an additional Gaussian-like factor in parallel momentum transfer $\mathbf{P}$ and the envelope prefactor varies as the power 3/2 instead of 1/2. This behavior is due to the effects of correlations in vibrations of closely neighboring parts of the surface and as a result of the fact that the law of conservation of momentum applies

only to components parallel to the surface.

Both Eq. (2.1) and (2.2) have been shown to explain certain types of experiments. The discrete model of Equation (2.1), with the form factor $|\tau_{fi}|^2$ taken as a constant has been shown to explain the shape as well as the temperature and energy dependence of the single scattering peak observed in the collisions of low energy ions with metal surfaces [49, 50]. It has also been useful for describing energy-resolved spectra for heavy rare gas scattering from molten metal surfaces [51, 52]. The smooth surface model of Eq. (2.2) explains the temperature and incident energy dependence of He atom scattering from a metal surface at high temperatures and energies [53, 54] and describes the angular distributions and energy-resolved spectra observed in rare gas scattering from liquid metals and metal alloys [51, 52, 55].

The smooth surface model depends on a parameter v_R usually expressed in dimensions of velocity which is a weighted average of all phonon speeds at the surface. It can be expressed in terms of the surface phonon polarization vectors at the classical turning point, and for highly symmetric crystals has the form [45, 46]

$$\frac{1}{v_R^2} = \frac{1}{2k_B T_S \mathbf{k}^2} \sum_{\mathbf{Q}} \sum_{\nu} \frac{\hbar \mathbf{Q}^2}{N\omega_\nu(\mathbf{Q})} \left|\mathbf{k}\cdot\mathbf{e}(\mathbf{Q},\nu)\right|^2 \left[2n(\omega_\nu(\mathbf{Q}))+1\right] , \tag{2.3}$$

where the scattering wave vector is $\mathbf{k} = (\mathbf{p}_f - \mathbf{p}_i)/m$, $\omega_\nu(\mathbf{Q})$ is the frequency of a phonon mode with parallel wave vector $\mathbf{Q}$ and perpendicular index ν, N is the number of modes, $n(\omega)$ is the Bose-Einstein occupation number, and $\mathbf{e}(\mathbf{Q},\nu)$ is the polarization vector of the $(\mathbf{Q},\nu)$ phonon mode. Although v_R is completely defined through Eq. (2.3) if the phonon spectral density is known, it is usually treated as an adjustable parameter for fitting calculations of the differential reflection coefficient of Eq. (2.2) to experimental data [45, 46, 47] .

The typical experiments for which Eqs. (2.1) and (2.2) have been useful are scattering of beams of the heavy rare gas atoms. The measured energy-resolved intensity spectra for fixed incident and scattering angles usually consist of a single broad peak whose width increases and whose maximum intensity decreases with increasing surface temperature. The measurements are usually made at angles that maximize the intensity observed in the peak. Under such conditions, calculations using Eqs. (2.1) and (2.2) will produce peaks with maxima located at close to the same energy positions (i.e., located at nearly the same most probable final energies) but Eq. (2.1) gives peaks that are typically broader in energy width than those observed experimentally. Eq. (2.2), because it contains an additional Gaussian-like term in the parallel momentum transfer $\mathbf{P}$ will produce a peak with an increasingly narrow energy width as v_R is increased and the value of v_R is usually chosen by matching the width of the scattered distribution to that of the experimental data.

In the case of the smooth, vibrating surface, the statistical mechanical parameter, v_R, that arises is a kind of correlation speed. This parameter may be determined from the surface phonon spectral density, but it is difficult to obtain. There are experimental conditions under which information concerning the value of v_R may be more easily obtained, and such conditions as discussed in the following subsection.

2.2 Suggested Experiment to Determine v_R

The quantity v_R is expected to be on the order of magnitude of the surface phonon velocity in the case of smooth solid surfaces [45]. It has been found to be smaller than the Rayleigh phonon velocity for many solids [56]. Due to decreased vibrational correlation, v_R is expected to be smaller for smooth surfaces than for rough surfaces. For the same reason, there is expected to be an even larger differ-

ence between the value of v_R and the bulk velocity of sound. There are experimental conditions, that may be easily obtained, under which the parameter v_R can be more accurately extracted from the energy-resolved spectra. It should be possible to compare calculations with data taken at angles that differ from maximum intensity conditions, because at such angles there will be a difference between predictions of Eqs. (2.1) and (2.2) for the most probable energy position of the peak and that energy shift will be strongly dependent on v_R [57].

An example is shown in Fig. 2.1 which gives calculations for Ar with an incident energy of $E_i = 40$ kJ/mol (415 meV) scattered from a liquid In surface at a temperature of 436 K, slightly higher than its melting point [57]. The incident angle is $\theta_i = 46^\circ$ and the final angle is $\theta_f = 44^\circ$ corresponding to a fixed source-to-detector angle $\theta_{SD} = 90^\circ$ which is a commonly found experimental geometry. The dashed curve is the calculation of the discrete model of Eq. (2.1) and the solid curve is the calculation of the smooth surface model of Eq. (2.2) and there is a clear shift in energy denoted by δE_{mp} between their most probable energy positions. This shift is a function of v_R which in this case is chosen to be 2000 m/s. The origin of the δE_{mp} shift between the two calculations is the Gaussian-like term in $\mathbf{P}$ appearing in the smooth surface model. For the discrete model of Eq. (2.1) the most probable energy position is very nearly given by the condition that the argument of the exponential vanishes, i.e., $E_f - E_i + \Delta E_0 = 0$. This condition is equivalent to the well-known Baule relation $E_f = f(\mu, \theta) E_i$ for the final energy as a function of total scattering angle θ for an elastic collision between an incoming particle of mass m and energy E_i and a stationary particle with mass M_C. The function $f(\mu, \theta)$ of Eq. (3.2) is determined by the conditions of conservation of energy and momentum and depends on mass ratio $\mu = m/M_C$ and total scattering angle θ, the angle between $\mathbf{p}_f$ and $\mathbf{p}_i$.

For given incident and final angles the most probable intensity of the smooth

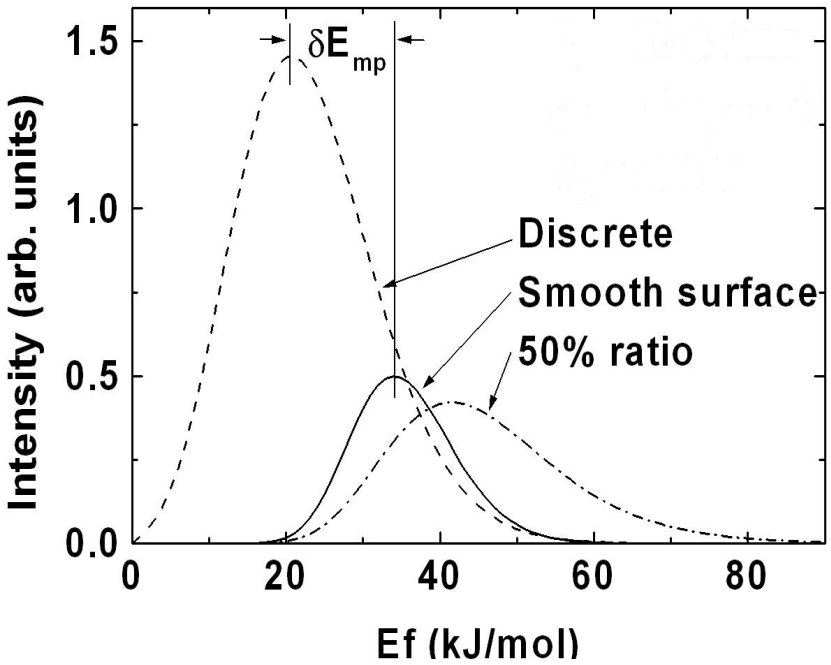

Figure 2.1: Energy resolved intensity spectra of Ar scattered from liquid In for $E_i =$ 40 kJ/mol and $T_S = 436$ K. The solid curve is the smooth-surface calculation of Eq. (2.2) for $\theta_i = 46°$, $v_R = 2000$ m/s and $\theta_f = 44°$, conditions corresponding to 50 per cent of the maximum of most probable intensity as shown in Fig. 2.2. The dashed curve is the discrete model calculation of Eq. (2.1), and the dash-dotted curve is the ratio of Eq. (2.2) to Eq. (2.1).

surface model of Eq. (2.2) occurs near the energy that minimizes the argument of the exponential. However, only at certain angles will this minimum argument actually vanish, because this requires the simultaneous conditions of $E_f - E_i + \Delta E_0 = 0$ and $\mathbf{P} = 0$. Close to these critical angles of most probable energy the most probable intensity will tend to achieve local maximum values. For example, under the initial conditions of Fig. 2.1 this occurs at the angle $\theta_i \approx 37^\circ$ (and consequently $\theta_f \approx 53^\circ$) [57]. Another way of describing the smooth surface model is to view it as the product of the discrete model differential reflection coefficient multiplied by the following Gaussian-like function in parallel momentum transfer

$$S(\mathbf{p}_f, \mathbf{p}_i) \;=\; \frac{\pi}{k_B T_S \Delta E_0} \exp\left\{ -\frac{2 v_R^2 \mathbf{P}^2}{4 k_B T_S \Delta E_0} \right\} \; . \tag{2.4}$$

The function $S(\mathbf{p}_f, \mathbf{p}_i)$ is not a true Gaussian function because ΔE_0 depends upon the initial and final momentum vectors. This dependence can result in skewed distributions. The function $S(\mathbf{p}_f, \mathbf{p}_i)$ is also plotted in Fig. 2.1 with the matrix element given by

$$\tau'_{fi} = 4 p_{fz} p_{iz} / m \; , \tag{2.5}$$

the Jackson-Mott matrix element taken in the limit for a strongly repulsive barrier, an approximate form that has been very useful in the analysis of atomic and molecular scattering data [52, 55].

It is now clear from Fig. 2.1 that the energy-resolved spectrum of the smooth surface model can be viewed as the product of Eq. (2.1) for the discrete model and the Gaussian-like function of Eq. (2.4) in parallel momentum $\mathbf{P}$. The resulting product is also roughly Gaussian in shape and of similar width, but its intensity is substantially reduced with respect to that of the discrete model and its most probable energy is

shifted. The suggestion is that comparing this energy shift δE_{mp} with experimental measurements taken at wide range scattering angles will be a much more sensitive way of choosing the parameter v_R than simply fitting the shape of the curve for the energy-resolved intensity spectrum in the region of angles where that spectrum is maximized [57]. This suggestion will also be applicable to to determining the scaling parameter of other theories of surface scattering that contain product Gaussian functions of parallel momentum transfer [58].

As implied above, most experimental studies of energy-resolved spectra have been carried out with incident and detection angles adjusted near to the critical conditions of maximum intensity, which closely corresponds to the positions where the argument of the exponential of Eq. (2.2) vanishes. The calculations presented in Fig. 2.1 show that when the observation conditions deviate from those optimal critical angles the intensity strongly decreases [57]. This effect, in fact, has been indirectly noted in measurements of angular distributions [59, 60] , both those measured with fixed incident angle and those measured by varying the incident angle in a detector with a fixed source-detector angle θ_{SD} [61, 62] . For both types of angular distributions, calculations using the discrete model predict scattered distributions that have full widths at half maximum that are much too broad. In contrast, the smooth surface model with appropriate choice of the parameter v_R gives a good fit to the observed scattered angular distributions [52, 63, 64].

Because the observable intensity decreases rapidly as incident and detector angles deviate from the optimum angles, this gives rise to the question of whether there will be sufficient intensity to measure when the energy shift δE_{mp} becomes appreciable. This question is addressed in Fig. 2.2 which is carried out for the same incident conditions as Fig. 2.1 with a fixed $\theta_{SD} = 90^\circ$ and $v_R = 2000$ m/s [57].

The solid curve shows the predictions of the smooth surface model at the

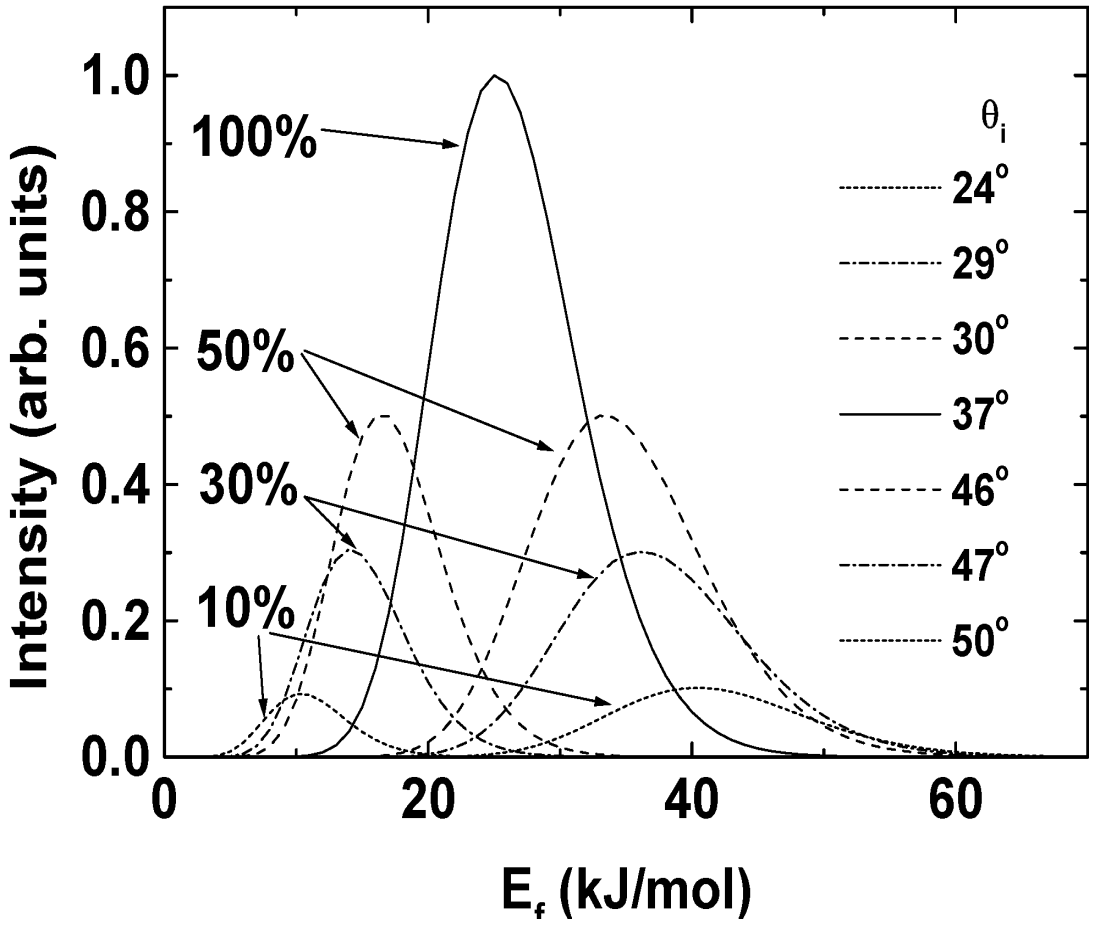

Figure 2.2: Energy resolved spectra of Ar scattered from liquid In for $T_S = 436$ K and $E_i = 40$ kJ/mol with a fixed $\theta_{SD} = 90°$ and $v_R = 2000$ m/s. Critical angular conditions for a maximum of the most probable scattered intensity occur at $\theta_i = 37°$ as indicated by a solid curve. Pairs of other curves are drawn for angular conditions at which the most probable intensity is 50%, 30% and 10% of this maximum, as marked. In each pair, the smaller angle corresponds to the peak shifted to lower energy than that for $\theta_i = 37°$.

critical maximum intensity angle $\theta_i = 37°$. The two long-dashed curves, one on each side of the solid curve, show calculations for incident angles at which the predicted intensity is 50% of the maximum. One of these two peaks, for $\theta_i = 46°$, is the same calculation shown in Fig. 2.1 where it is clear that the energy shift is $\delta E_{mp} \approx 14$ kJ/mol or about a third of the incident energy. Two further pairs of curves are given in Fig. 2.2 that show calculations for incident angles at which the predicted most probable intensity is 30% and 10% of the maximum. For these latter curves the energy shift δE_{mp} is even larger, as large as one third of the incident energy for the 10% case. Thus, the calculations in Fig. 2.2 imply that substantial energy shifts can be obtained while still retaining sufficient intensity for measurement.

The question of expected energy shift dependency on incident angle and on the parameter v_R is addressed in Fig. 2.3 [57]. This shows, for the same incident conditions as in Fig. 2.2 and with $\theta_{SD} = 90°$, calculations of δE_{mp} as a function of $\cos\theta_i$ for several selected values of v_R. For small values of v_R the energy shifts are not large, but for v_R as large as 2000 m/s the energy shift can become comparable to the incident energy. Note that at the critical point of maximum intensity, at $\cos\theta_i = 0.8$ for this case, there is a small energy shift between the two calculations due to the different prefactors in Eqs. (2.1) and (2.2). Also shown in Fig. 2.3 are a pair of solid curves, one on either side of the critical angle, marked 50% and another similar pair marked 10%. These two pairs of curves mark the locus of points where the most probable intensity predicted by the smooth surface model is 50% and 10%, respectively, of the maximum value at the critical angle. Thus, if at least 50% of the maximum observable intensity is required for measurements, this calculation implies that measurements can be made for all angles between the two solid curves labelled 50%. These calculations indicate that energy shifts as large as 20 kJ/mol, or up to half the incident energy in this case, can in principle be measured. Such sizeable shifts,

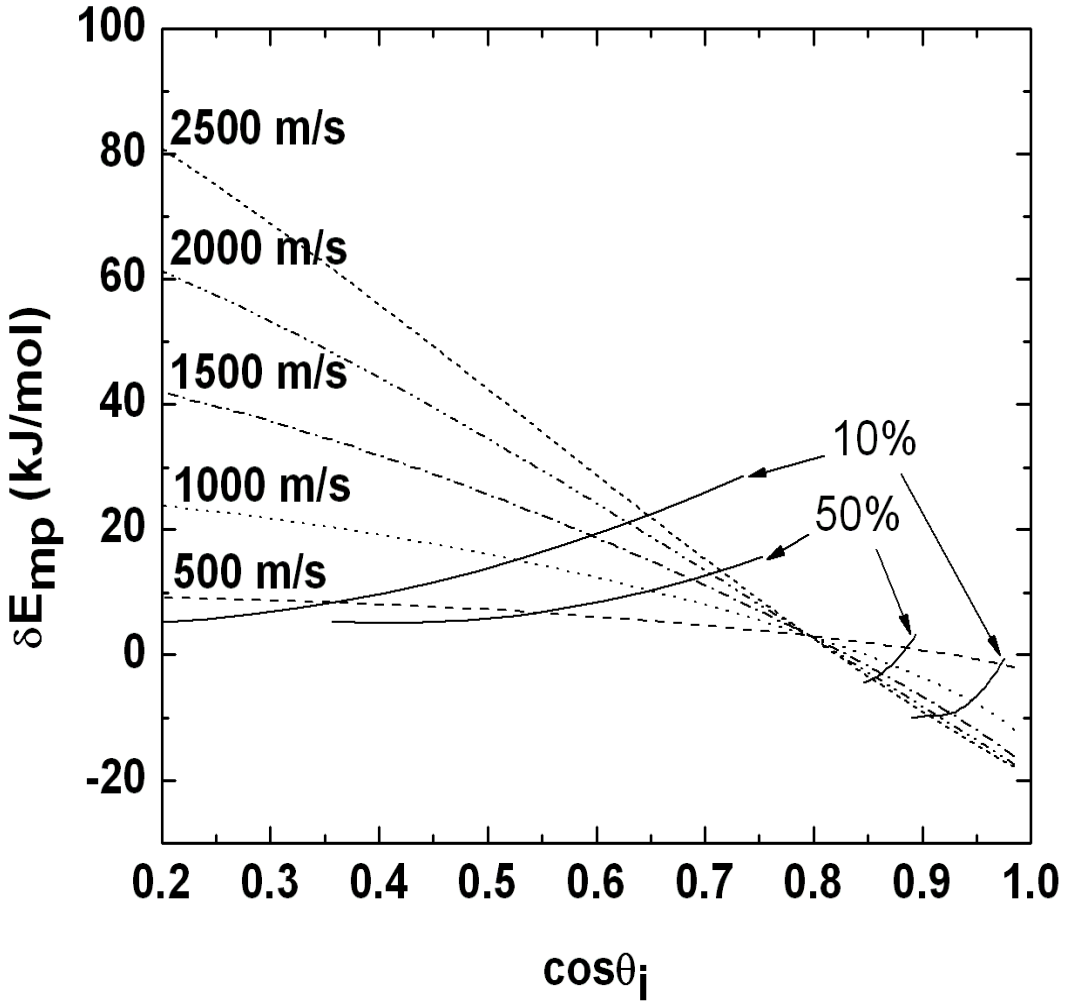

Figure 2.3: The energy shift δE_{mp} versus $\cos\theta_i$ for the same conditions as in Fig. 2.2, calculated for several different values of v_R as indicated. The solid curves are the loci of points for which the most probable scattering intensity is 50% and 10%, respectively, of the maximum most probable intensity.

together with the prediction that the corresponding intensities are readily observable, would indicate that rather precise values of v_R could be obtained by fitting data to the smooth surface theory.

The smooth surface theory of Eq. (2.2) has proven to be quite useful in the interpretation and analysis of data for atom and molecule scattering from surfaces, but it does depend on the velocity parameter v_R. However, precise knowledge of v_R can be important because it provides physical information on the system dynamics, in particular it can be related to the polarization vectors of the phonons at the classical turning point through its defining equation (2.3). In the past, the method of determining the parameter v_R has been to measure energy-resolved intensity spectra at angles close to conditions that maximize the observed intensities, and then fit Eq. (2.2) to the width of the observed experimental peak using v_R as a variable parameter. This suggests that a much more precise way of determining v_R is to make measurements over a range of incident and final angles that deviate from the critical conditions of maximum intensity, and then determine v_R by fitting the energy shifts δE_{mp} with respect to the parameter-free discrete model predictions of Eq. (2.1). Calculations for a wide range of systems and initial conditions, of which specific examples are shown here, indicate that such measurements should be feasible [57].

2.3 Introduction of Multiple Collisions and Potential Wells

2.3.1 Multiple Collisions

The case of multiple scattering due to successive collisions of the incoming projectile with different surface atoms can be treated as convolutions of successive single

collisions using the discrete model. The differential reflection coefficient including both single and double scattering terms is

$$\frac{dR^{(2)}(\mathbf{p}_f,\mathbf{p}_i)}{d\Omega_f dE_f} = \frac{dR^{(1)}(\mathbf{p}_f,\mathbf{p}_i)}{d\Omega_f dE_f} + \left\langle \sum_{n=1}^{N} \int_0^\infty dE_q \int_{\Delta\Omega_n} d\Omega_q \frac{dR^{(1)}(\mathbf{p}_f,\mathbf{p}_q)}{d\Omega_f dE_f} \frac{dR^{(1)}(\mathbf{p}_q,\mathbf{p}_i)}{d\Omega_f dE_f} \right\rangle . \tag{2.6}$$

The summation is over a set of surface atoms with which the second collisions occur. For a liquid the angular brackets signify the average over the positions of the number N of neighboring surface atoms, and $\Delta\Omega_n$ is the solid angle subtended by the second atom as viewed from the initial collision,

$$\frac{\Delta\Omega_n}{4\pi} = \frac{\pi(a_1+a_2)^2}{4\pi d^2}, \tag{2.7}$$

where a_1 and a_2 are the radii of the projectile and substrate atoms and d is the average interatomic distance in the liquid metal. The differential reflection coefficient does not vary strongly over the area subtended by each of the second substrate atoms so the angular integration is replaced by a multiplicative factor of $\Delta\Omega_n$. This approximation has been checked by carrying out exact integrations over intermediate angles, and differences in the final results were small. For the calculations presented here, N includes the six nearest neighbor atoms in the surface plane. Higher-order multiple scattering terms may be treated by adding multiple convolutions of the single scattering differential reflection coefficient to Eq. (2.6) and have been done so with great success [65, 66, 67, 68].

The solid angles subtended by the surface atoms involved in the second collisions are usually small. The angular dependence of the intermediate differential reflection coefficient in the double collision may be ignored. The angular integration in Eq. (2.6) may be replaced by a multiplicative factor, $\Delta\Omega_n$. The multiple scattering

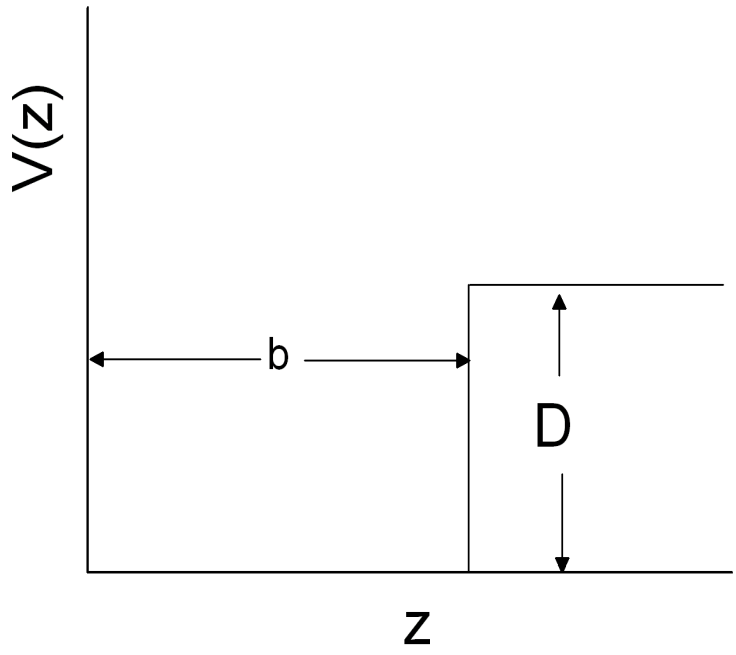

Figure 2.4: A square-well potential in front of a surface. The width of the well is b, the depth D.

of Eq. (2.6) depends on only a single parameter, the classical cross-section of of the target atom, $\Delta\Omega/4\pi$. This is the fractional solid angle subtended by the cross-section at the distance of the nearest neighbor surface atom.

2.3.2 Interaction Potential Wells

An important aspect of the description of the interaction of incident gas atoms and a surface is the nature of the potential well of the interaction potential. The simplest model of the potential well has been used, the square well of depth D, in front of the repulsive surface, Fig. 2.4. The primary effect of an attractive well is to increase the translational energy and to refract the incident particle. This causes the

incident particle to collide with the surface at a higher translational momentum and a scattering angle closer to normal. If the well width is greater than the region bounded by the maximum and minimum of the corrugation of the hard repulsive surface then the width of the well is unimportant. The effect in the collision with the surface is to enhance the perpendicular component of the momentum.

In Fig. 2.5 the momenta and angles inside and outside the well are shown. With the presence of a potential well the translational energy is replaced by

$$\begin{aligned} E_i^{'} &= E_i + |D| \\ E_f^{'} &= E_f + |D|. \end{aligned} \tag{2.8}$$

The increase in energy caused by the well changes the normal momentum,

$$\begin{aligned} {p_{iz}^{'}}^2 &= p_{iz}^2 + 2m|D| \\ {p_{fz}^{'}}^2 &= p_{fz}^2 + 2m|D|, \end{aligned} \tag{2.9}$$

while the parallel components are unchanged,

$$\begin{aligned} p_{ix}^{'} &= p_{ix} \\ p_{fx}^{'} &= p_{fx}. \end{aligned} \tag{2.10}$$

The remaining relation between $\cos(\theta_f^{'})$ and $\cos(\theta_f)$ is found to be

$$\cos(\theta_f^{'}) = \sqrt{\frac{E_f^T \cos(\theta_f) + |D|}{E_f^T + |D|}}. \tag{2.11}$$

The differential reflection coefficient in the asymptotic region, at the detector

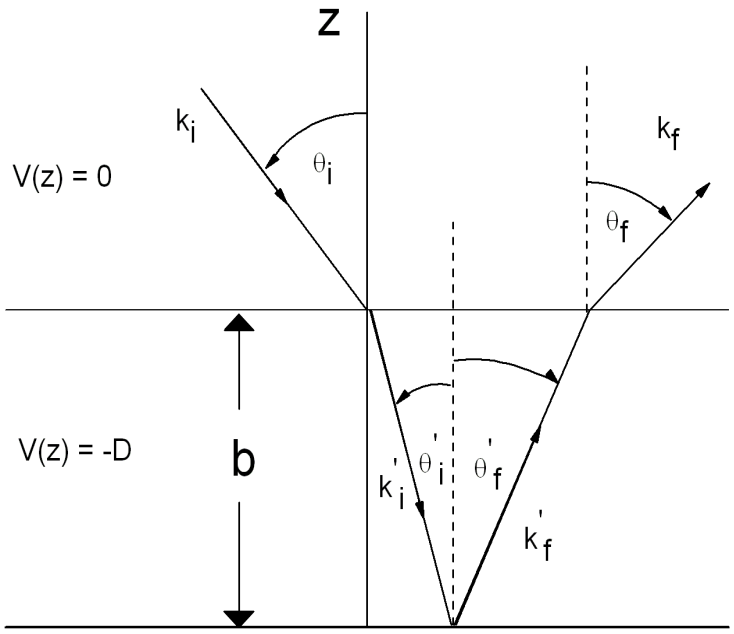

Figure 2.5: A square-well potential in front of a surface showing the effect of refraction. The width of the well is b, the depth D.

position, is

$$\frac{dR(\mathbf{p}_f, \mathbf{p}_i)}{d\Omega_f dE_f^T} = J \frac{dR'}{d\Omega_f' dE_f'}, \tag{2.12}$$

with the Jacobian

$$J = \frac{E_f^T \cos(\theta_f)}{\sqrt{\left(E_f^T \cos^2(\theta_f) + |D|\right)\left(E_f^T + |D|\right)}}. \tag{2.13}$$

2.4 Derivation of the Discrete and Smooth Surface Models

Both the smooth and discrete models may be derived from a single approach [69] that also yields a model that accounts for surface corrugation. A generalization of the Fermi Golden Rule for the transition rate w_{fi} [70], originally derived by Dirac [71],

$$w_{fi} = \frac{2\pi}{\hbar} \langle \sum_{n_f} |T_{fi}|^2 \delta(\mathcal{E}_f - \mathcal{E}_i) \rangle, \tag{2.14}$$

where T_{fi} is the transition matrix for the initial and final states of the projectile plus target system. The $\mathcal{E}_f$ and $\mathcal{E}_i$ are the final and initial energies of the entire system. The $\langle \dots \rangle$ indicate the average over all initial target states and the summation $\sum_{n_f}$ is over all final target states.

The van Hove-Glauber transformation, in which the Dirac delta is written in its time-integral Fourier transform, and the interaction picture is used [72, 73]:

$$\delta\left(E_f - E_i\right) = \frac{1}{2\pi\hbar} \int_{-\infty}^{+\infty} dt \exp \frac{\imath \left(\mathcal{E}_f - \mathcal{E}_i\right) t}{\hbar}. \tag{2.15}$$

Then the Hamiltonian of the target governs the time dependence, and we have

$$w\left(\underline{k}_f, \underline{k}_i\right) = \frac{1}{\hbar^2}\int_{-\infty}^{+\infty} dt \exp\left(\frac{\imath(E_f - E_i)t}{\hbar}\right)\langle T_{if}\left(t\right) T_{fi}\left(0\right)\rangle, \tag{2.16}$$

with E_i and E_f the initial and final translational energies of the incident atom.

The approximation will be made that the transition operator separates into two parts,

$$\hat{T} = \hat{T}_z \hat{T}_R, \tag{2.17}$$

and is a product of an operator in the normal direction, $\hat{T}_z$, and an operator in the direction parallel to the surface, $\hat{T}_R$. The transition operator then becomes

$$T_{fi} = [\Phi_f\left(z\right)|\hat{T}_z|\Phi_i\left(z\right)][\Psi_f\left(x,y\right)|\hat{T}_{xy}|\Psi_i\left(x,y\right)]. \tag{2.18}$$

The probability of a transition from k_{iz} to k_{fz} is proportional to $|[\Phi_f\left(z\right)|\hat{T}_z|\Phi_i\left(z\right)]|^2$.

The $\hat{T}_{xy}$ will be evaluated by means of the eikonal approximation [74]. For completely elastic scattering from a hard, repulsive wall potential the wave function is

$$\Psi_i\left(\underline{r}\right) = \exp\imath\left(\underline{k}_i \cdot \underline{r}\right) - \sum_{\underline{K}} A\left(\underline{K}\right)\exp\imath[(\underline{K}_i + \underline{K})\cdot\underline{R} + \imath k_{fz} z]. \tag{2.19}$$

The component of the incident wave vector, $\underline{k}_i$, parallel to the surface is $\underline{K}_i$ with $\underline{K} = \underline{K}_f - \underline{K}_i$. From conservation of energy, for elastic scattering in which there is no energy transfer to the surface,

$$k_{fz}^2 = k_{iz}^2 - k^2 - 2\underline{K}\cdot\underline{K}_i. \tag{2.20}$$

The $A(\triangle\underline{K})$ is proportional to the transition matrix

$$[\Psi_f(x,y)|\hat{T}_{xy}|\Psi_i(x,y)] = \imath\left(\frac{\hbar^2 k_{fz}}{mL}\right)\exp(\imath\delta_f)A(\underline{K}), \tag{2.21}$$

with m the incident atom mass, L a quantization length and δ_f a phase .

In order to apply the eikonal approximation, the Rayleigh anzatz [75], which assumes that the wave function in the asymptotic region of Eq. (2.19) is valid near the surface, is used along with the hard wall boundary conditions

$$\Psi(\underline{R}, z = \xi(\underline{R})) = 0, \tag{2.22}$$

with $\xi(\underline{R})$ the corrugation function of the hard wall. Assuming weak dependence of k_{fz} upon $\underline{K}$, the eikonal approximation, allows the $A(\underline{K})$ to be written as

$$A(\triangle\underline{K}) = \frac{1}{L^2}\int d\underline{R}\exp(-\imath\underline{K}\cdot\underline{R} - \imath\triangle k_z\xi(\underline{R})), \tag{2.23}$$

with $\triangle k_z = k_{fz} + k_{iz}$.

Equation (2.23) is the result of the eikonal approximation for a purely elastic scattering problem. A potential with thermal vibrations is treated by use of the surface displacement function $\underline{u}(\underline{R}, t)$ in Eq. (2.23) by the transformations

$$\underline{R} \rightarrow \underline{R} - \underline{u}_{\|}(\underline{R}, t) \tag{2.24}$$

$$\xi(\underline{R}) \rightarrow \xi(\underline{R}) - u_z(\underline{R}, t). \tag{2.25}$$

This results in a transition rate of

$$
\begin{aligned}
w\left(\underline{k}_f, \underline{k}_i\right) = \frac{1}{\hbar^2}\left(\frac{\hbar^2 k_{fz}}{mL}\right)^2 \left|\left[\Phi_f(z)|\hat{T}_z|\Phi_i(z)\right]\right|^2 \int_{-\infty}^{+\infty} dt \exp(\frac{\imath(E_f - E_i)t}{\hbar}) \\
\frac{1}{L^4}\int d\underline{R}_1 \int \underline{R}_2 \exp(-\imath \underline{K}\cdot(\underline{R}_1 - \underline{R}_2)) \exp(-\imath \triangle k_z[\xi(\underline{R}_1) - \xi(\underline{R}_2)]) \\
\langle \exp(\imath \triangle \underline{k}\cdot u(\underline{R}_1, t)) \exp(-\imath \triangle \underline{k}\cdot u(\underline{R}_2, 0))\rangle
\end{aligned}
\tag{2.26}
$$

with $\underline{k} = \underline{k}_f - \underline{k}_i$.

Using the harmonic approximation and calculating the average $\langle \dots \rangle$ yields

$$
\begin{aligned}
w\left(\underline{k}_f, \underline{k}_i\right) = \frac{1}{\hbar^2}\left(\frac{\hbar^2 k_{fz}}{mL}\right)^2 \left|\left[\Phi_f(z)|\hat{T}_z|\Phi_i(z)\right]\right|^2 \int_{-\infty}^{+\infty} dt \exp(\frac{\imath(E_f - E_i)t}{\hbar}) \\
\frac{1}{L^4}\int d\underline{R}_1 \int d\underline{R}_2 \exp(-\imath \underline{K}\cdot(\underline{R}_1 - \underline{R}_2)) \exp(-\imath \triangle k_z[\xi(\underline{R}_1) - \xi(\underline{R}_2)]) \\
\exp\left(-2W\left(\triangle \underline{k}\right)\right) \exp\left(2\mathcal{W}\left(\triangle \underline{k}; \underline{R}_1 \underline{R}_2, t\right)\right),
\end{aligned}
\tag{2.27}
$$

after taking account of the commutation relations between displacement operators at different positions and times [48, 76]. The $\exp\left(-2\,W(\triangle \underline{k})\right)$ is the Debye-Waller factor and its argument may be evaluated to

$$
\begin{aligned}
2W\left(\triangle \underline{k}\right) &= \langle (\triangle \underline{k}\cdot \underline{u})^2 \rangle \\
&= \triangle \underline{k}^2 \langle u_z^2 \rangle \\
&= \frac{3\hbar^2 \triangle \underline{k}^2 T_S}{M_C k_B \Theta_D^2}.
\end{aligned}
\tag{2.28}
$$

The second equality of Eq. (2.28) is dependent upon there being high crystal symmetry, such as in FCC, BCC, or HCP crystal structure. The third equality of Eq. (2.28) is due to use of the Debye approximation [77], where Θ_D is the Debye temperature.

Under these standard approximations all cross terms average to zero and the mean-square displacements in all directions are all assumed to be equal. The introduction of a surface destroys the symmetry. However, these are standard assumptions that have been found to work well even in the presence of a surface.

The position and time dependent correlation function in the exponential for a periodic surface will also exhibit the periodicity, so may be expanded in normal modes of vibration [48, 76], and may be written

$$\begin{aligned} 2\mathcal{W}\left(\triangle\underline{k};\underline{R}_1,\underline{R}_2,t\right) &= \langle\triangle\underline{k}\cdot\underline{u}\left(\underline{R}_1,t\right)\triangle\underline{k}\cdot\underline{u}\left(\underline{R}_2,0\right)\rangle \\ &= \sum_{\alpha,\alpha'=1}^{3}\triangle k_\alpha\triangle k_{2\alpha'}\sum_{\underline{Q},\nu}\frac{\hbar}{2N_C M_C\omega_\nu\left(\underline{Q}\right)} \\ &\quad e_\alpha\left(\underline{Q},\nu\right)e_{\alpha'}\left(\underline{Q},\nu\right) \\ &\quad \exp\imath\left(\underline{Q}\cdot\left(\underline{R}_1-\underline{R}_2\right)\right)\left\{\left[n_\nu\left(\underline{Q}\right)+1\right]\right. \\ &\quad \left.\exp\left(-\imath\omega_\nu\left(\underline{Q}\right)t\right)+n_\nu\exp\left(\imath\omega_\nu\left(\underline{Q}\right)t\right)\right\}, \end{aligned} \tag{2.29}$$

where $e_\alpha\left(\underline{Q},\nu\right)$ is the α component of the polarization vector of a mode with $\underline{Q}$ the parallel wave-vector for that mode, ν is the discrete quantum number for surface modes and is continuous for bulk modes. The number of modes is N_C, the crystal mass M_C, and $\omega_\nu\left(\underline{Q}\right)$ is the frequency of that mode. The Bose-Einstein function

$$n\left(\omega_\nu\left(\underline{Q}\right)\right)=\left[\exp\left(\hbar\omega_\nu\left(\underline{Q}\right)/k_BT_S\right)-1\right]^{-1}. \tag{2.30}$$

It is important to note that the Debye-Waller exponent of Eq. (2.28) is $W\left(\triangle\underline{k}\right)=\mathcal{W}\left(\triangle\underline{k};\underline{R}_1=\underline{R}_2,t=0\right)$, and is important in the classical multiphonon limit of the transition rate. Its value is a measure of the number of phonons transferred in a scattering event. It will be large when either $\triangle\underline{k}$ is large, or the surface temperature,

T_S is large. Large T_S implies effectively large mean-square displacements. When $2W$ is large the Debye-Waller factor is negligible indicating that a large number of phonons has been transferred in the scattering event. This is completely incoherent, classical scattering and the coherence of the beam is destroyed.

When $2W$ becomes large the correlation function Eq. (2.29) is also important. The position correlation function is not always large since it is an oscillatory function. The leading terms in the correlation function come from contributions involving small t and small separations, $\underline{R}_1 - \underline{R}_2$. Equation (2.29) can be expanded, showing only the leading terms,

$$\begin{aligned} 2\mathcal{W}\left(\triangle\underline{k};\underline{R}_1,\underline{R}_2,t\right) \approx 2W\left(\triangle k\right) + \sum_{\alpha,\alpha'=1}^{3} \triangle k_\alpha \triangle k_{\alpha'} \Bigg\{ & -\imath t \sum_{\underline{Q},\nu} \frac{\hbar}{2N_C M_C} e_\alpha\left(\underline{Q},\nu\right) e_{\alpha'}\left(\underline{Q},\nu\right) \\ & - t^2 \sum_{\underline{Q},\nu} \frac{\hbar\omega_\nu\left(\underline{Q}\right)}{2N_C M_C} e_\alpha\left(\underline{Q},\nu\right) e_{\alpha'}\left(\underline{Q},\nu\right)\left[2n_\nu\left(\underline{Q}\right)+1\right] \\ & - \sum_{\underline{Q},\nu} \frac{\hbar[\underline{Q}\cdot(\underline{R}-\underline{R}')]^2}{4N_C M_C \omega_\nu\left(\underline{Q}\right)} e_\alpha\left(\underline{Q},\nu\right) e_{\alpha'}\left(\underline{Q},\nu\right)\left[2n_\nu\left(\underline{Q}\right)+1\right] \Bigg\} + \ldots, \end{aligned} \tag{2.31}$$

with $2W\left(\triangle k\right)$ the Debye-Waller factor of Eq. (2.29).

Under the assumption of a Debye model and symmetry similar to the bulk material the correlation function is, again showing only the leading terms,

$$\begin{aligned} 2\mathcal{W}\left(\triangle\underline{k};\underline{R}_1,\underline{R}_2,t\right) \approx & \; 2W\left(\triangle\underline{k}\right) - \imath\triangle E_0 t \\ & - \triangle E_0 k_B T_S t^2 - \frac{\triangle E_0 k_B T_S \left(\underline{R}_1 - \underline{R}_2\right)^2}{2\hbar^2 v_R^2} + \ldots . \end{aligned} \tag{2.32}$$

The classical recoil energy is

$$\triangle E_0 = \frac{\hbar^2 \triangle\underline{k}^2}{2M_C}. \tag{2.33}$$

The v_R is the weighted average of the phonon speeds of phonons parallel to the surface. This has been evaluated for simple models of the surface phonon density resulting in values on the order of the bulk acoustic phonon velocities, or the Rayleigh wave velocity [45, 78].

From purely quantum mechanical scattering to completely incoherent classical scattering, Eq. (2.27) is the point of departure and development. It is from Eq. (2.27) that the various surface models used in this work may be derived with the use of Eq. (2.32).

The discrete model Eq. (2.1) may be obtained from Eq. (2.27) by taking $v_R \gg$ than the numerator in the argument of the exponential. This gives, with Eq. (2.32)

$$w\left(\underline{k}_f, \underline{k}_i\right) = \frac{2\pi}{\hbar^2}\left(\frac{\hbar^2 k_{fz}}{mL}\right)^2 |[\Phi_f(z)|\hat{T}_z|\Phi_i(z)]|^2 |A\left(\underline{K}\right)|^2 \\ \frac{1}{\sqrt{4k_B T_S \triangle E_0}} \exp\left(-\frac{\left(E_f - E_i + \triangle E_0\right)^2}{4k_B T_S \triangle E_0}\right). \tag{2.34}$$

As it is, this describes a single classical collision. If

$$\left(\frac{\hbar^2 k_{fz}}{mL}\right)^2 |[\Phi_f(z)|\hat{T}_z|\Phi_i(z)]|^2 |A\left(\underline{K}\right)|^2 = constant, \tag{2.35}$$

hard sphere scattering, or the discrete model of Eqs. (2.1) is obtained after application of Eq. (2.46), an expression encountered in neutron scattering [39].

The smooth surface, or Brako-Newns, model of Eq. (2.2) may be obtained from Eq. (2.27) by again setting the same prefactors equal to a constant and using a corrugation function, $\xi(\underline{R})$ for a flat surface. This usually involves setting a parameter

for corrugation height equal to zero, with the result

$$w\left(\underline{k}_f, \underline{k}_i\right) \propto \frac{1}{\sqrt{4k_B T_S \triangle E_0}} \frac{1}{4k_B T_S \triangle E_0} \exp\left(-\frac{\left(E_f - E_i + \triangle E_0\right)^2 + 2\hbar^2 v_R^2 \underline{K}^2}{4k_B T_S \triangle E_0}\right). \tag{2.36}$$

Again applying Eq. (2.46) results in the differential reflection coefficient of Eq. (2.2).

2.5 Derivation of Models With Corrugation

The purpose of developing Eq. (2.27) is to enable the extraction of information about the corrugation function $\xi(\underline{R})$ and thus the corrugation experienced by the incident atom. It has been suggested that the surface temperature dependence of the most probable intensity of energy resolved spectra for gas-surface systems my be used to extract such information [79]. As may be seen in Eqs. (2.1), the surface temperature dependence of the envelope function of the discrete model is proportional to $T_S^{-1/2}$, while that of Eqs. (2.2) is approximately proportional to $T_S^{-3/2}$. The surface temperature dependence of the most probable intensity of energy resolved spectra for experimental data is expected to lie between these two limiting cases.

In order to account for corrugation of a surface it is necessary to evaluate

$$w\left(\underline{k}_f, \underline{k}_i\right) = w\left(\underline{k}_f, \underline{k}_i\right)_{discrete} S\left(\triangle \underline{K}\right), \tag{2.37}$$

with

$$S\left(\triangle \underline{K}\right) = \frac{1}{L^4} \int d\underline{R}_1 \int \underline{R}_2 \exp(-\imath \triangle \underline{K} \cdot (\underline{R}_1 - \underline{R}_2)) \exp(-\imath \triangle k_z [\xi(\underline{R}_1) - \xi(\underline{R}_2)]) \exp\left(-\frac{\triangle E_0 k_B T_S \left(\underline{R}_1 - \underline{R}_2\right)^2}{2\hbar^2 v_R^2}\right), \tag{2.38}$$

where $w\left(\underline{k}_f, \underline{k}_i\right)_{discrete}$ is the transition rate of the discrete model. The necessary expression for the corrugation is $\xi(\underline{R})$, for the surface to be studied. This will be applied to a one-dimensional surface,

$$\xi\left(\underline{R}\right) = ha\cos\left(\frac{2\pi}{a}x\right), \tag{2.39}$$

and in-plane scattering, $\triangle\underline{K} = \triangle K_x$. The periodicity condition is $\xi\left(x+na\right) = \xi\left(x\right)$, with a the corrugation period, and the interaction potential for a corrugated surface is defined by

$$V\left(x,z\right) = \begin{cases} \infty, & z < \xi(x) \\ 0, & z \geq \xi(x). \end{cases}$$

Classical scattering requires integration over only one period of the corrugation, since there is no coherent scattering. Equation Eq. (2.38) may be evaluated in Cartesian coordinates:

$$\begin{aligned} S\left(\triangle\underline{K}\right) = \frac{1}{L^4}\int_{-\frac{a}{2}}^{\frac{a}{2}} dxdx' \int_{-\infty}^{+\infty} dydy' \exp\left(-\imath\triangle K_x\left(x-x'\right)\right) \\ \exp(-\imath\triangle k_z[\xi(x)-\xi(x')]) \\ \exp\left(-\alpha^2[(x-x')^2+(y-y')^2]\right), \end{aligned} \tag{2.40}$$

with

$$\alpha^2 = \frac{\triangle E_0 k_B T_S}{2\hbar^2 v_R^2}. \tag{2.41}$$

The integrals over y and y' are

$$\int_{-\infty}^{+\infty} dydy' = L\frac{\sqrt{\pi}}{\alpha}. \tag{2.42}$$

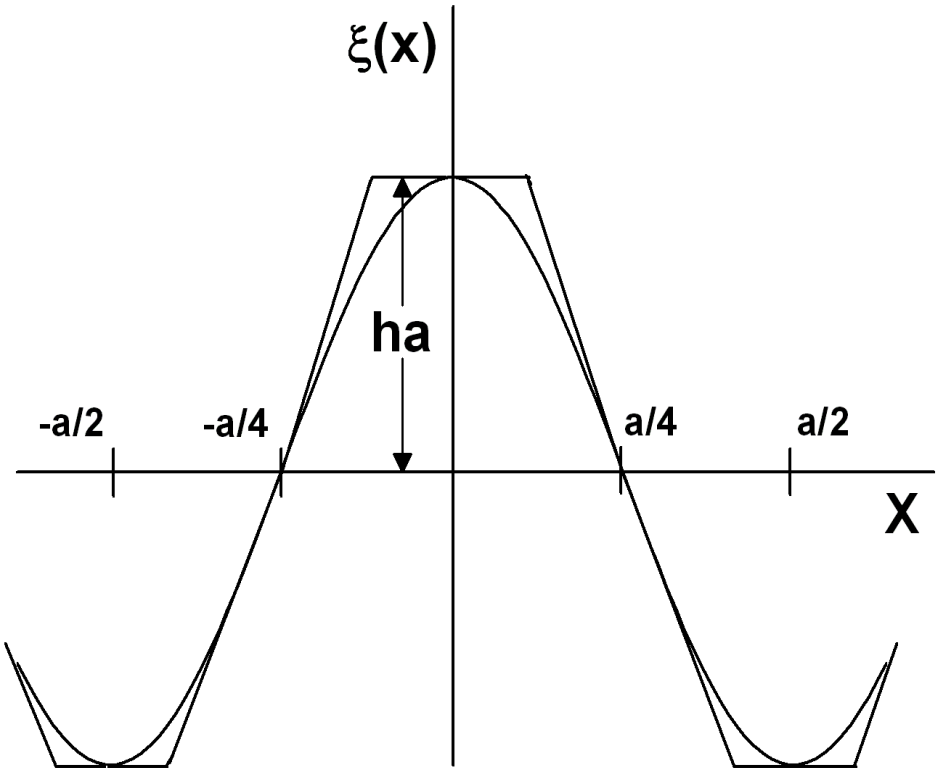

Figure 2.6: Approximation to the sinusoidal corrugation function. The corrugation amplitude is h. The interparticle spacing is a, which is also the period. The points of inflection are at $x = \pm a/4$

This gives a transition rate of

$$w\left(\underline{k}_f, \underline{k}_i\right) = w\left(\underline{k}_f, \underline{k}_i\right)_{discrete} \frac{L}{L^4} \frac{\sqrt{\pi}}{\alpha} \int_{-\frac{a}{2}}^{\frac{a}{2}} dx dx' \exp(-\imath \triangle K_x (x - x')) \exp(-\imath \triangle k_z [\xi(x) - \xi(x')]) \exp\left(-\alpha^2 \left(x - x'\right)^2\right). \tag{2.43}$$

An analytic approximation for Eq. (2.43) may be obtained for the sinusoidal corrugation as shown in Fig. 2.6. The flat part, tangent to the sinusoid at its maximum

and minimum, results in a contribution identical to that of the smooth model. The contributions from the sloped segments passing through the points of inflection may integrated exactly, being linear in $x - x'$.

The slopes at the inflection points must first be determined:

$$\begin{aligned} \xi(x) &= ha\cos\left(\frac{2\pi}{a}x\right) \\ &\approx ha\cos\left(\frac{2\pi}{a}x\right)\Big|_{\frac{a}{4}} - ha\sin\left(\frac{2\pi}{a}x\right)\Big|_{\frac{a}{4}}\delta x + \ldots . \end{aligned} \tag{2.44}$$

So

$$\xi(x) = \begin{cases} \approx -2\pi h\left(x - \frac{a}{4}\right) & \text{at } x = \frac{a}{4} \\ \approx 2\pi h\left(x - \frac{a}{4}\right) & \text{at } x = -\frac{a}{4} \end{cases}$$

This gives

$$\xi(x) - \xi(x') = \begin{cases} -2\pi h\left(x - x'\right) & \text{for } x \approx \frac{a}{4} \\ 2\pi h\left(x - x'\right) & \text{for } x \approx -\frac{a}{4} \end{cases}$$

Using this in Eq. (2.43), to a very good approximation when α is large results in

$$w^{\mp}\left(\underline{k}_f, \underline{k}_i\right) = \begin{cases} w_{discrete}\frac{a\pi^2}{L^3\alpha^2}\exp\left(-\frac{(\triangle K_x - 2\pi h\triangle k_z)^2}{4\alpha^2}\right) & \text{negative slope} \\ w_{discrete}\frac{a\pi^2}{L^3\alpha^2}\exp\left(-\frac{(\triangle K_x + 2\pi h\triangle k_z)^2}{4\alpha^2}\right) & \text{positive slope} \end{cases} \tag{2.45}$$

The differential reflection coefficients may be obtained from

$$\frac{dR(\mathbf{p}_f, \mathbf{p}_i)}{d\Omega_f dE_f} = \frac{L^4 m^2\left|\underline{k}_f\right|}{\left(2\pi\hbar\right)^3 k_{iz}} w\left(\underline{k}_f, \underline{k}_i\right). \tag{2.46}$$

An approximation to the sinusoidal corrugation function may be obtained by means of a linear combination of the differential reflection coefficients for the positive

and negative slope transition rates of Eq. (2.45) and that of a flat, smooth surface Eq. (2.36). This gives a transition rate for the combination model,

$$w\left(\underline{k}_f, \underline{k}_i\right) = \frac{2w_{smooth}\left(\underline{k}_f, \underline{k}_i\right) + Aw^{+}\left(\underline{k}_f, \underline{k}_i\right) + Aw^{-}\left(\underline{k}_f, \underline{k}_i\right)}{2 + 2A}, \tag{2.47}$$

where w^{+} and w^{-} are the transition rates for the positive and negative slope parts of Eq. (2.45), respectively, and w_{smooth} is the smooth surface result of Eq. (2.36).

The A is the relative lengths of the smooth and sloped parts used to approximate the cosine corrugation. In order to determine the value of A the cosine corrugation is be expanded about $x = 0$ and $x = a/4$,

$$\cos\left(\frac{2\pi h}{a}\right) \approx -ha[1 - \frac{2\pi^2}{a^2}\delta x^2], \tag{2.48}$$

for $x = 0$, and

$$\cos\left(\frac{2\pi h}{a}\right) \approx -2\pi h\delta x[1 - \frac{2\pi^2}{3a^2}\delta x^2] \tag{2.49}$$

for $x = a/4$. This gives a ratio of $\delta x_{x=a/4} = \sqrt{3}\delta x_{x=0}$, since these expansions are valid over a neighborhood $\sqrt{3}$ larger than near $x \approx 0$. Thus, $A = \sqrt{3}$.

Chapter 3

Argon on Ruthenium

3.1 Introduction

Transition metals have received much attention because of their unusual structural and electronic properties. These originate in the effects of d-electrons upon electronic structure. These metals also have phonon anomalies due to the complex geometry of their Fermi surfaces. Surface phonon dispersion and associated anomalies reveal changes in the bonding properties of atoms near the surface. The high catalytic activity of ruthenium, an hcp metal, makes it one of the most active metals and important in heterogeneous catalysis. The synthesis of NH_3, for example, may be Ru-based. This has been a stimulus for many investigations into the interaction of the ruthenium surface with gasses. Clean crystal surfaces and especially the interaction of hydrogen with ruthenium have been investigated. Most attention has been given to the (0001) surface. Surface phonon dispersion curves have been measured for clean Ru(0001) surface and hydrogen covered ruthenium surfaces, Ru(0001)+H(1×1) along the high symmetry directions, $[11\bar{2}0]$ and $[1\bar{1}00]$, by means of high resolution helium atom scattering [80]. These experiments also determined the Rayleigh phonon

velocities for the clean ruthenium surface along the $[11\bar{2}0]$ and $[1\bar{1}00]$ directions, 3608 m/s and 3494 m/s, respectively.

Experiments on the Ar/Ru system have been carried out resulting in time-of-flight and in-plane angular spectra [81, 82, 83]. An unusual aspect of these experiments was that the width of the incident beam was nearly that of the resulting energy-resolved spectra. Usually, these beams are considerably more narrow. Also, unusual features in the angular spectra appeared that indicated the presence of diffraction in cases where none was to be expected. While energy-resolved spectra calculated from theory compared well with the data, such agreement required the use of an effective target mass of 2.3 Ru atomic mass. The calculated angular distributions were consistently broader then the data even with the larger effective mass.

3.2 Experiment

In these experiments argon scattering from Ru(0001) was examined for a range of incident beam energies. The experiments were carried out in an ultra-high vacuum chamber consisting of a main chamber with the sample mounted on a three-axis goniometer, a sample manipulator with six degrees of freedom, which allows the study of azimuthal dependence during experiments [84]. A supersonic beam source having an 80 mm alumina nozzle was attached to the main chamber. The beam source had three stages with a rotating chopper in the second stage. Translational energy of the argon beam was varied from 0.065 to 2.5 eV. These beam energies were determined by measuring the time-of-flight of a 10 ms pulse of gas from the chopper to a differentially pumped, rotatable quadrupole mass spectrometer in the scattering chamber. The final energy of the scattered atoms was obtained by deconvolution of their time-of-flight signals with the direct beam profiles. The QMS could be rotated

in a horizontal plane around the sample, placed in the middle of the vacuum chamber. The ruthenium sample was aligned and polished to within 0.1° of the (0001) crystal face. Electron bombardment (600 V, 80 mA) was the heat source, with a rate of up to 25 K/s, and cooled to ≈ 100 K with liquid nitrogen. Cleaning was performed in situ by repeated cycles of flashing in a background pressure of oxygen at $2 \cdot 10^{-8}$ mbar to 1500 K. An oxygen free surface could be obtained by a single flash to 1600 K in ultra-high vacuum (UHV).

3.3 Results

3.3.1 Energy Resolved Spectra

A series of five measured energy-resolved intensity spectra as functions of final energy for argon scattering from Ru(0001) are shown in Fig. 3.1, converted from time-of-flight data, for an incident energy $E_i = 0.08$ eV, and incident polar angle $\theta_i = 40°$ and with the detector positioned at the final angle $\theta_f = 20°$. The surface temperatures range from 140 K to 850 K as marked. These spectra are characterized as smooth, broad, single-peaked structures which get broader with a longer high-energy tail at increasing temperature. The position of the peak, or most probable energy, remains essentially at the same position for all temperatures.

These energy resolved spectra exhibit no evidence of quantum mechanical features such as sharp diffuse elastic or single surface phonon peaks. The expected classical nature under these conditions can be verified by calculating the Debye-Waller factor $\exp\{-2W\}$ where the simplest approximation gives

$$2W \;=\; \frac{6\Delta E_0 T_S}{k_B \Theta_D^2} \;\approx\; \frac{24m(\sqrt{E_i}\cos\theta_i + \sqrt{E_f}\cos\theta_f)^2 T_S}{M_C k_B \Theta_D^2}\,, \tag{3.1}$$

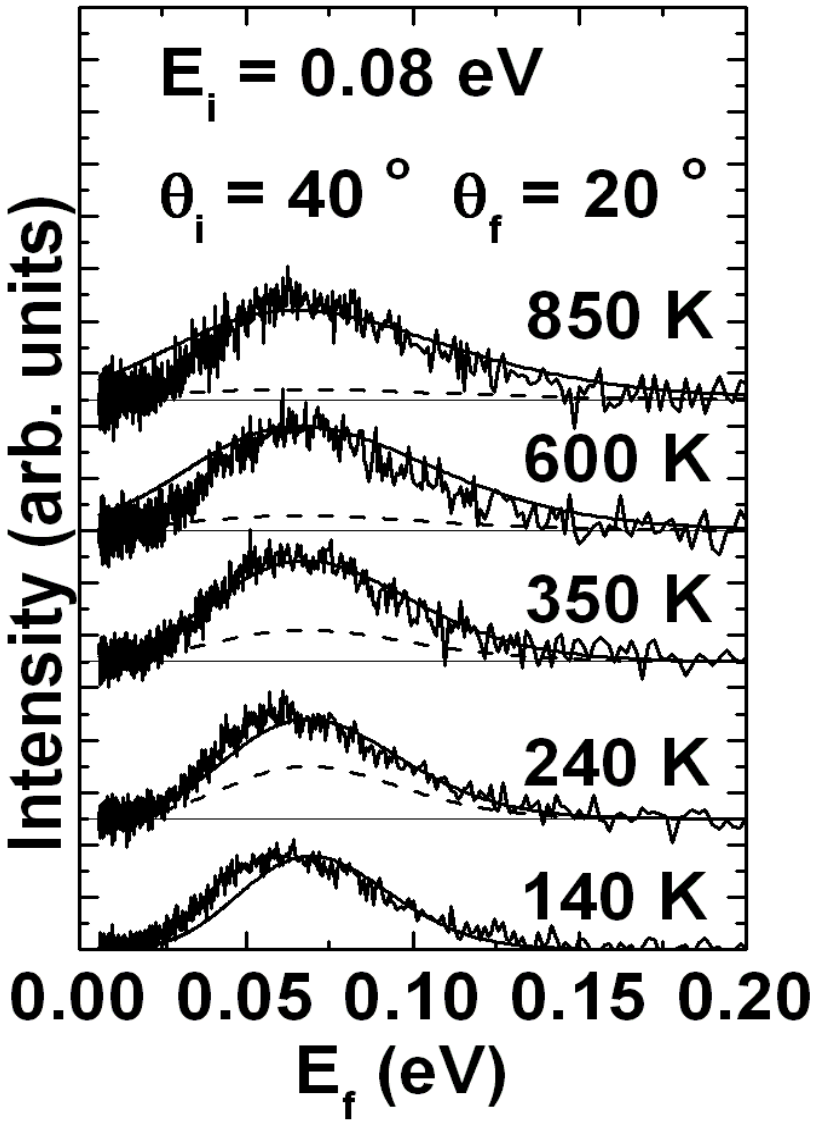

Figure 3.1: Energy resolved spectra of Ar scattered from Ru(0001) at surface temperatures T_S ranging from 140 to 850 K as marked. The incident energy is $E_i = 0.08$ eV, the incident angle is $\theta_i = 40°$ and the final angle is $\theta_f = 20°$. The theoretical calculations, normalized to the data at each temperature, are shown as smooth solid curves and the calculated intensities relative to that at 140 K are shown as dashed curves.

where the approximate evaluation is obtained by neglecting the parallel momentum transfer. The exponent $2W$ is a measure of the approximate number of phonons created or destroyed in a collision and when it is large the scattering is purely classical. Using for the surface mass M_C the mass of a single Ru atom and a value of 216 K for the Debye temperature Θ_D [82], the value of $2W$ in the region of the most probable final energy is about 16 even at the lowest temperature. Such a large value would reduce all quantum features to negligible intensity, and indicate clear classical conditions.

Calculations from Eq. (2.2) are shown as solid lines and for each temperature the calculations were normalized to the data at one point near the most probable intensity [85, 86, 87, 88]. The experimental data were reported in arbitrary units, and information about relative intensities at different temperatures was not determined. The theory of Eq. (2.2) predicts a decrease in the most probable intensity with surface temperature, and these relative theoretical calculations are shown as the dashed lines, normalized to the data at the lowest temperature of 140 K. The calculations match the general features of the data reasonably well, the increase in the high-energy tail is well predicted, but the calculations predict a larger increase of broadening with temperature than that observed.

However, as mentioned above, all calculations presented in this paper were carried out with an effective surface mass of 2.3 Ru atomic masses [85, 86, 87, 88]. The reason for this is that a smaller effective mass produces too much energy loss and gives curves that are too broad and do not match the most probable final energies observed in the data of Fig. 3.1. Without this larger effective mass, the calculated most probable final energy is less than half that observed. The need for an effective mass is indicative of a collective effect in which several Ru atoms are involved in the collision process, and this is discussed further below in Sec. 4.4. The value of

the effective mass will also affect the Debye-Waller factor, implying that the value of $2W$ should be divided by 2.3. This would change the typical value calculated above to $2W \approx 6$ at the lower temperature and ranging up to over 30 at the higher temperatures, but these values are still large and within the range indicating classical scattering conditions.

It is of interest to examine the temperature dependence of the widths of the energy resolved peaks of Fig. 3.1 because the theory of Eq. (2.2) predicts that the width should increase approximately as the square root of the temperature. These are shown in Fig. 3.2 which plots the squared full width at half maximum (FWHM) as a function of T_S [85, 86, 87, 88]. The data points taken from Fig. 3.1 are shown as open circles and the calculations are filled squares. The least-squares best fit to the data is shown as a solid line.

The square root dependence of the FWHM is obtained from Eq. (2.2) by making a Gaussian expansion of the argument about its minimum point. This gives the resulting approximations

$$(FWHM)^2 \approx 16 \ln(2)\, g(\theta)\, E_i k_B T_S \,, \tag{3.2}$$

where

$$g(\theta) = \frac{g_{TA}(\theta)}{\left[1 + \mu - \mu \cos\theta / \sqrt{f(\theta)}\right]^2} \,, \tag{3.3}$$

with $g_{TA}(\theta)$ given by

$$g_{TA}(\theta) = \mu \left[1 + f(\theta) - 2\sqrt{f(\theta)} \cos(\theta)\right] . \tag{3.4}$$

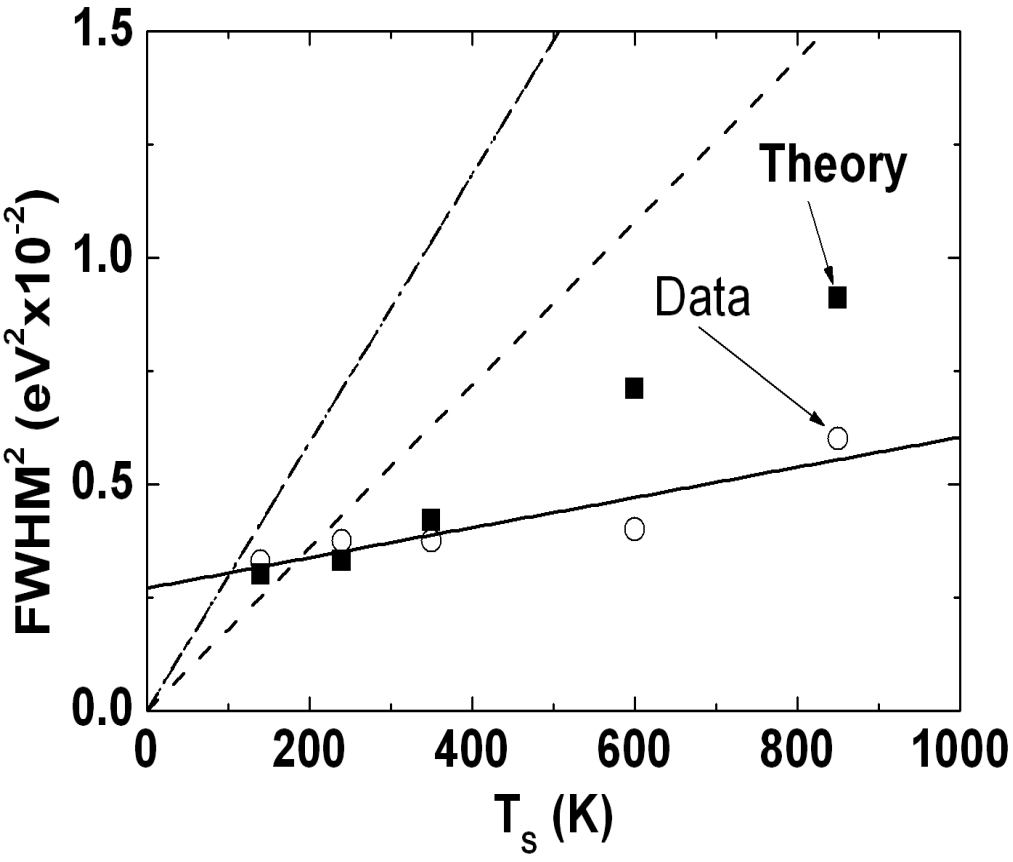

Figure 3.2: The squared FWHM plotted as a function of surface temperature for the same data as shown in Fig. 3.1. Experimental points are shown as circles and calculations are shown as squares. The solid line is the least-squares fit to the data. The dashed line is the Gaussian approximation to the present theory, and the dash-dotted line is the trajectory approximation.

and θ is the total scattering angle (the angle between $\mathbf{p}_f$ and $\mathbf{p}_i$). The function

$$f(\theta) = \left(\frac{\sqrt{1 - \mu^2 \sin^2 \theta} + \mu \cos \theta}{1 + \mu} \right)^2 , \tag{3.5}$$

is obtained by setting $E_f - E_i + \Delta E_0 = 0$ which produces the well-known Baule expression for the energy transfer in a hard-sphere collision,

$$E_f = f(\theta) E_i \tag{3.6}$$

The linear approximation of Eq. (3.2) is shown in Fig. 3.2 as a dashed line. Also shown is the trajectory approximation, the dash-dot line, which is obtained by replacing $g(\theta)$ in Eq. (3.2) by $g_{TA}(\theta)$.

It is seen that the theoretical points deviate from the Gaussian approximation of Eq. (3.2), exhibiting an increase with surface temperature that is less than expected. This behavior is due to the convolution with the rather broad energy width of the experimental incident beam. Calculations assuming a monoenergetic and angularly well-defined incident beam have FWHMs that agree quite well with Eq. (3.2). The experimental data have widths that increase at a substantially slower rate with surface temperature than Eq. (3.2). The theoretical calculations in Fig. 3.2 indicate that part of this deviation may be due to the rather poor energy definition of the incident beam. However, this temperature dependence of the data is unusual. In all other experimental investigations that have been compared with similar theoretical approaches as here, when the initial conditions indicated small Debye-Waller factors based on Eq. (3.1) and hence classical scattering conditions, the expected square-root dependence of the FWHM was quite well obeyed.

3.3.2 Angular Distributions

Examples of angular distributions measured at three incident energies 0.08 eV, 0.56 eV and 1.4 eV are shown in Fig. 3.3. The incident angle is $\theta_i = 60^\circ$ and the surface temperature is 140 K. The lowest energy angular distribution measured shows a relatively sharp peak at the specular position $\theta_f = 60^\circ$ sitting on top of a broad background. This sharp peak is attributed to specular diffraction [82], its width being approximately the same as the experimental angular uncertainty of 2°. This assignment to a quantum mechanical diffraction feature appears to be correct in the light of the present calculations. A simple evaluation of the Debye-Waller exponent gives $2W = 7$ at the specular position for $E_i = 0.08$ eV, which would imply a Debye-Waller factor far to small for a quantum feature to be visible, but with an effective mass of 2.3 Ru atoms $2W$ becomes only 2.8, a value for which quantum effects should be easily measurable. The calculation, shown as a solid curve, should be compared only to the background since it contains no diffraction, and it is seen that it qualitatively agrees with the observed background width [85, 86, 87, 88].

The intermediate energy angular distribution at $E_i = 0.56$ eV in Fig. 3.3 consists of a broad peak, but narrower in angular width, and shows another type of interesting behavior in the vicinity of the specular angle. This double-peaked structure is attributed to a classical rainbow feature [82]. There are no hints of quantum features at this energy, which must clearly be the case since the specular value of $2W$ is about 47. The calculated curve qualitatively agrees with the approximate width of the observed peak, but is not capable of exhibiting the rainbow structure [85, 86, 87, 88].

At the highest energy of 1.4 eV the experimental angular distribution becomes even narrower and no longer exhibits rainbow structure. Interestingly, the calculation predicts an angular distribution that is broader than that of the observations [85, 86,

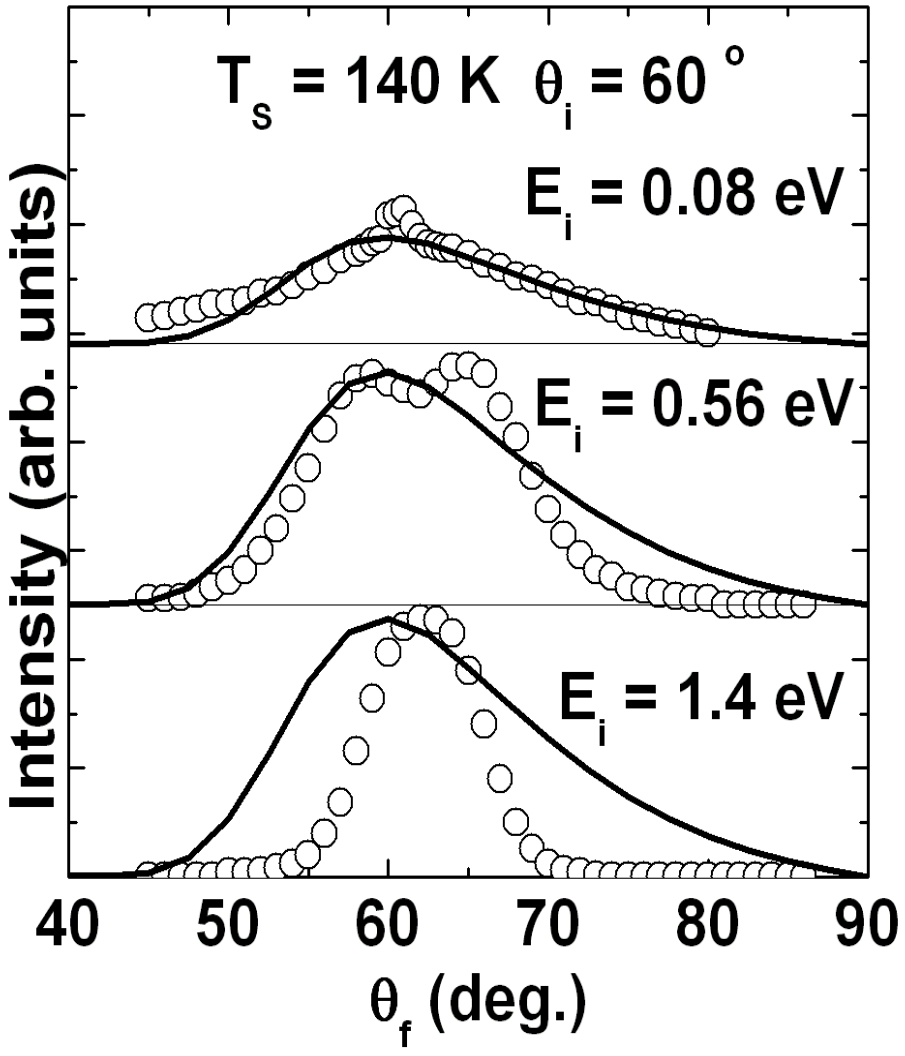

Figure 3.3: Angular distributions for Ar/Ru(0001) with $\theta_i = 60°$, surface temperature 140 K and three different incident energies E_i = 0.08, 0.56 and 1.4 eV as marked. The symbols are experimental data and the solid curves are calculations.

87, 88]. The calculated angular distributions become independent of the incident energy for large values of E_i. This is because the differential reflection coefficient of Eq. (2.2) becomes a very narrow, delta-function-like peak at the positions of the minima in the argument of the exponential.

Fig. 3.4 shows further examples of angular distributions taken for incident energies of 0.44, 1.05 and 1.56 eV with an incident angle of 50° and a relatively high surface temperature of 550 K. In this case the $2W$ values are quite large, the scattering is completely classical and there are no rainbow features. The FWHM at the lowest energy is observed to be about 20° and narrows with increasing energy to about 10° at the highest energy. The calculations have a distinctly larger width at every energy and do not show the narrowing exhibited in the data [85, 86, 87, 88].

In addition to the results reported in Ref. [82] a number of scattering experiments were performed on a Ru(0001) surface with a (1×1) monolayer coverage of hydrogen atoms [83]. On this surface the azimuthal orientation could be determined with LEED measurements and in Fig. 3.5 are shown angular distributions taken with a low incident energy of 0.065 eV, a surface temperature of 140 K and four incident angles from 40° to 70° separated by 10° intervals. At the most normal angle of $\theta_i = 40°$ the experimental points consist of a broad peak with a rather pronounced shoulder at about $\theta_f = 60°$ and for the more grazing incident angles a diffraction feature gradually appears at the specular position. For $\theta_i = 40°$ the value of $2W \approx 12$ at the specular position would seem to preclude the possibility of seeing a quantum peak, because even taking into account the effective mass would reduce this to about 5 which is still a rather large value for observing quantum effects. However, at the larger, more grazing angles the $2W$ value becomes smaller and for $\theta_i = 70°$ where $2W \approx 3$ (evaluated with the effective mass of a single Ru atom) a distinct specular diffraction peak is observed.

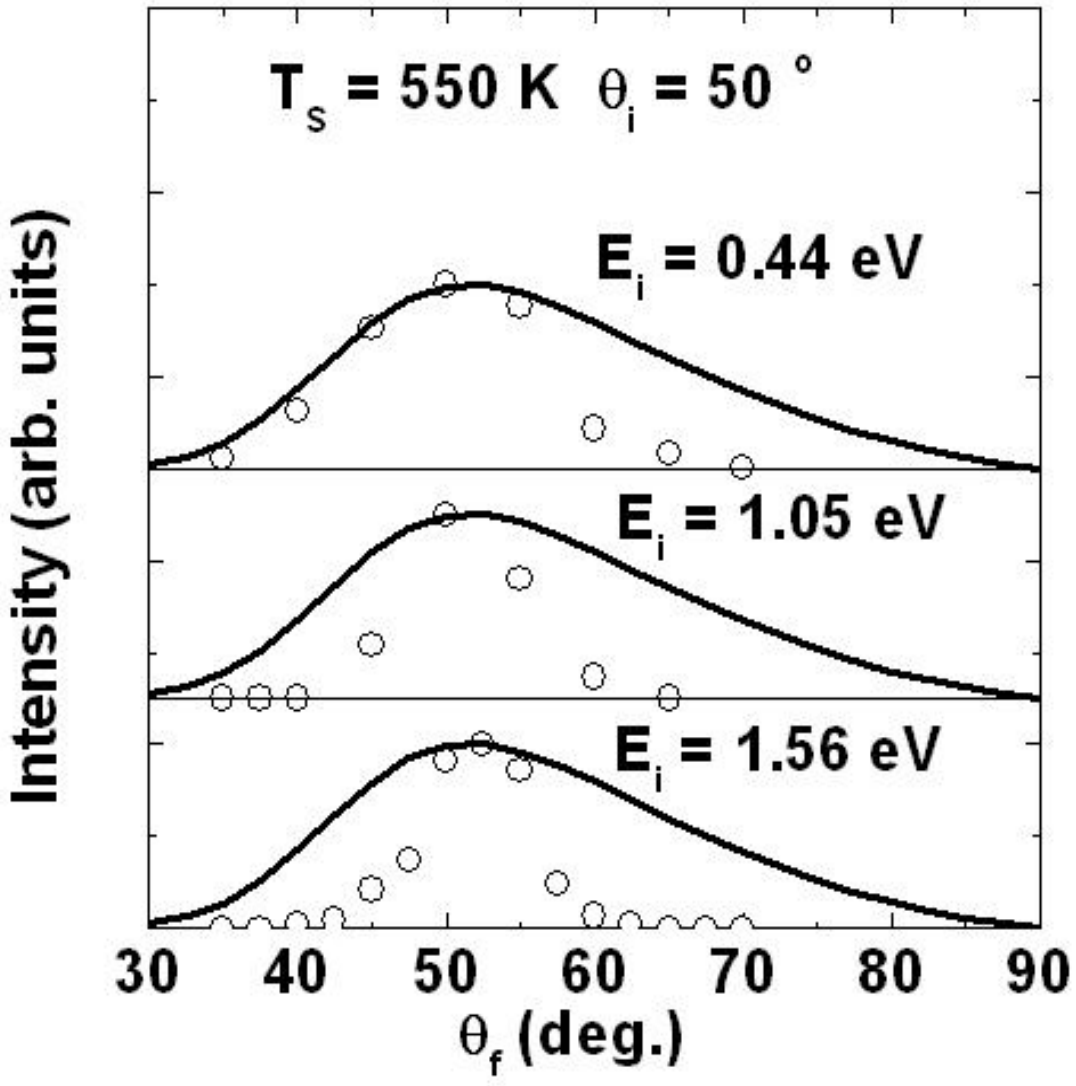

Figure 3.4: Angular distributions for Ar/Ru(0001) with $\theta_i = 50°$, surface temperature 550 K and three different incident energies $E_i = 0.44$, 1.05 and 1.56 eV as marked. The symbols are experimental data and the solid curves are calculations.

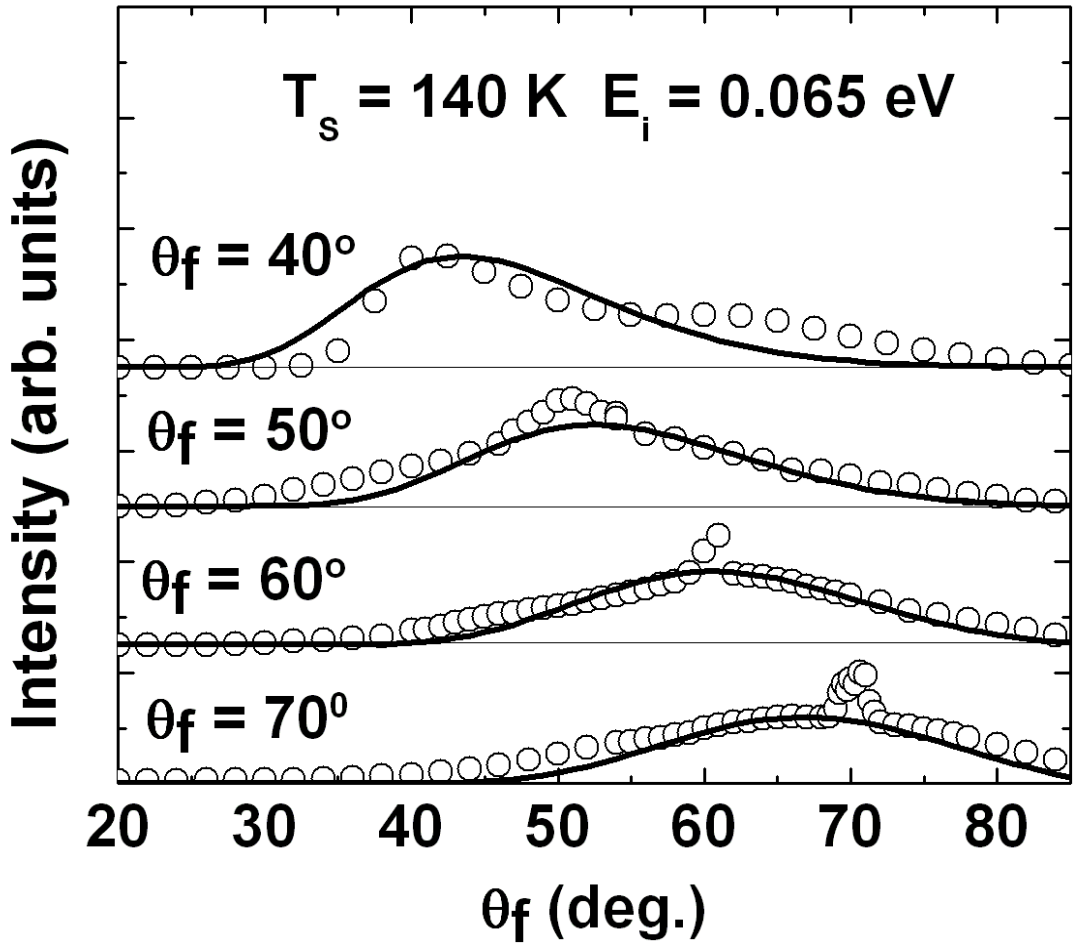

Figure 3.5: Angular distributions for Ar/Ru(0001)-(1×1)H in the $\langle 11\bar{2}0\rangle$ direction with $E_i = 0.065$ eV, surface temperature 140 K and four different incident angles ranging from 40° to 70° as marked. The symbols are experimental data and the dashed curves are calculations. The solid curves are calculations that have been renormalized to match the experimental data in the vicinity of the maximum in the background.

The calculations shown as solid curves in Fig. 3.5 were carried out assuming a clean Ru(0001) surface, i.e., ignoring the adsorbed H atoms. At the most normal incident angle of 40°, where the Debye-Waller evaluation clearly indicates classical scattering conditions, the calculations agree very well with the data [85, 86, 87, 88]. At the more grazing angles, since the exponent $2W$ near the specular position varies approximately as $\cos^2\theta_i$, the Debye-Waller factor quickly increases allowing the specular quantum diffraction to appear. In fact, if the effective mass is used $2W$ becomes approximately 1 at the largest angle of 70°, making this case clearly in the quantum regime. For these larger angles where quantum effects are important, the present classical mechanical calculations are not expected to be valid, and they explain only qualitatively the broad background under the specular peak.

3.4 Conclusions

In this chapter a classical theory of atomic collisions with surfaces has been used to analyze newly available experimental data for the scattered intensities produced by a beam of Ar atoms directed towards a Ru(0001) surface [85, 86, 87, 88]. The measurements consisted of final angular distributions of scattered particles, and energy resolved spectra taken at fixed final detector angles. Both of these types of measurements consisted of single-peaked features with very broad widths, typical of what might be expected for a heavy projectile scattering under classical conditions in which many phonons are transferred at each collision. However, at lower incident energies, there was clear experimental evidence for diffraction peaks, even under conditions for which a simple evaluation of the Debye-Waller factor would exclude any manifestation of quantum effects.

The present theoretical analysis, using a calculational model that has proved

to be useful in explaining scattering under classical conditions for a number of other systems, appears to resolve the question of why diffraction peaks are so readily visible in the Ar/Ru(0001) system. The observed energy resolved spectra and angular distributions can be explained only if the Ar atoms are assumed to be scattering from a collection of more than one Ru atom which has an effective mass of approximately 2.3 Ru atomic masses [85, 86, 87, 88].

This collective effect is most readily seen in the energy resolved spectra shown in Fig. 3.1. These exhibit a very large energy loss if one assumes that the surface mass is that of a single Ru atom. However, with a mass $M_C = 2.3$ Ru atoms the agreement with the theory, both in peak position and in FWHM, is in reasonable agreement with the measurements.

This, together with the fact that agreement between theory and data for the large number of angular distributions could be obtained only with the same larger mass, answers the question of why quantum diffraction effects could be observed. The same effective mass is what appears in the denominator of the Debye-Waller exponent $2W$ of Eq. (3.1), which implies that $2W$ is actually $1/2.3$ time smaller, and consequently the Debye-Waller factor much larger, allowing quantum effects to be readily seen.

This is not the first time that a collective effect requiring a larger effective mass has been noticed in atomic and molecular scattering from metal surfaces. One is a recent experimental investigation of N_2 scattering from the same Ru(0001) surface [89]. When this was analyzed with a mixed quantum-classical theory, agreement with the observed scattering spectra as functions of final translational and rotational energy required an effective surface mass of 2.3 Ru atomic masses, the same as here [90]. Thus, the present experiment is confirmation that the collective effect is due to the Ru surface and not unique to the Ar projectile. The N_2/Ru(0001) scattering experi-

ment was also able to independently measure average energies of the final distributions corresponding to motion parallel and perpendicular to the surface. Analysis of this indicated that the collective effect was with Ru atoms in layers beneath the surface and not with neighboring atoms in the surface layer.

The other experimental measurements whose analysis required a larger mass were for the three rare gases, Ne, Ar and Xe scattering from a molten Ga surface [60]. An analysis using a similar theory as in the present paper required an effective Ga mass for all three different projectiles of 1.65 Ga atoms [51, 57]. However, the same projectiles scattering from two other liquid metals, In and Bi, did not require an effective mass larger than their atomic masses. For Ga, the presence of a collective effect is supported by independent measurements that show that liquid Ga exhibits an anomalously large degree of ordered layering even at temperatures large compared to its melting point, in contrast to other low melting point temperature metals [91].

This observation of collective effects leads to an interesting prediction. The unusual nature of the Ru surface, with its large effective mass for atomic and molecular scattering, means that Ar atoms at subthermal energies, energies that are known to be readily achievable in He scattering experiments [92], can be used for scattering investigations in the quantum mechanical regime. This would, by extension, also imply that neon should also scatter very quantum mechanically since it has an intermediate mass. Thus, ruthenium presents a unique system in which surface structure and dynamics could be studied by quantum mechanical scattering of three quite different rare gas atoms, He, Ne and Ar.

The temperature dependence of the energy resolved spectra was also anomalous in comparison to virtually all other atomic and molecular surface systems that have been measured under classical scattering conditions. Theories such as that of Eq. (2.2) show that the FWHM should increase with the square root of the surface

temperature, as in Eq. (3.2), and this is a consequence of equipartition of energy. The present experiments exhibit a FWHM that increases with temperature, but substantially less strongly than expected as shown in Fig. 3.2. The present analysis shows that at least some of this anomalous behavior is due to the very large energy spread of the incident beam at low energies, because when the differential reflection coefficient of Eq. (2.2) is convoluted with the experimental energy distribution the calculated FWHMs also have a less strong increase with surface temperature.

A series of angular distributions were presented in Figs. 3.3 and 3.4. These also exhibit the rather unusual feature that the measured angular distributions plotted as functions of θ_f are actually narrower in width than the theoretical predictions. However, a reasonable qualitative description of their behavior as functions of the incident energy E_i, the incident angle θ_i and surface temperature surface temperature is provided, and this calculated behavior confirms the need for an effective surface mass.

To conclude, it is of interest to re-iterate the interesting and anomalous features observed in the Ar/Ru(0001) scattering experiments, to review the information that the present theoretical analysis is able to provide, and to make some suggestions for interesting new experiments. The measurements exhibit the following characteristics that are unusual in comparison to other systems that have been measured under similar conditions: (1) the energy losses exhibited in the energy resolved measurements are surprisingly small, (2) the temperature-dependent increase in FWHM of the energy-resolved spectra is weaker than predicted, (3) many of the angular distributions exhibit narrower peaks than expected, and (4) quantum mechanical diffraction was observed under conditions for which it was not expected.

These points are explained, at least qualitatively to some degree, by the present theoretical analysis. All of these features point towards a collective effect in the

Ru crystal that results in an effective mass for the collision of approximately 2.3 atomic masses of Ru. Such a collective effect has also been observed in scattering of N_2 by Ru(0001) [89, 90] and that experiment provided some limited evidence that the collective effect was with Ru atoms in crystal layers below the surface, and not with the other atoms in the outermost surface layer. The present experiment does not provide enough data to test this proposition, but additional experiments could do so if they are carried out for conditions that distinguish the transfer of parallel and perpendicular momentum. What is needed to answer this question is energy resolved measurements under conditions where the transfer of momentum is nearly perpendicular, which implies near normal incident and final angles, contrasted with measurements taken under conditions that favor parallel momentum transfer, which implies that at least one of the incident or final angles should be at a near surface-grazing position. Also helpful would be experiments from which average energies associated with motion parallel and perpendicular to the surface could be measured.

Perhaps the most important observation to come out of this work is the fact that the present calculations support and confirm the observation of quantum mechanical diffraction features in the experiments. On the basis of assuming a surface mass of a single Ru atom, quantum effects would be predicted to be unobservable under most of the experimental conditions in which they definitely were observed. It is now obvious, however, because the present calculations show clearly that the effective mass is that of about 2.3 Ru atoms, that diffraction and other quantum effects are not only observable but are to be expected for Ar/Ru scattering under a broad range of incident conditions at low energies. This leads to the interesting conclusion that Ru is a metal for which scattering experiments in the purely quantum regime could be readily carried out with three different rare gas atoms, Ar, Ne and He. Because of their widely differing masses, quantum diffraction and single phonon measurements

with these three projectiles would provide interesting comparative structural and dynamical information on the surface electron density at different classical turning point distances from the outermost surface layer. For example, a comparative examination of both He and Ne atom diffraction from hydrogen-covered nickel and rhodium surfaces was able to demonstrate clear anticorrugating effects due to the hybridization of the orbitals of the incoming atoms with the unoccupied metal states [93]. The availability of three different but very quantum mechanical projectiles with widely different masses for probing Ru surfaces could lead to similar important comparative studies on this system.

Chapter 4

Scattering of Noble Gases From Liquid Metals

4.1 Introduction

There are many physical and chemical processes that are of fundamental importance that occur at gas-liquid interfaces. These processes are often important in applications such as catalysis, lubrication, gas chromatography, and removing impurities from liquid, or molten metals. Monatomic liquid metals have are described as the ptotypical simple liquids [94]. Most of the physical properties of real fluids are encountered, but few of the complications are present. Some liquid metals have viscosities and densities similar to that of water and are useful as nuclear reactant coolant.

Maxwell, in the late 1800's, studied fluids from a phenomenological point of view [95, 96]. It was not until the development of statistical mechanics that a microscopic description of the dynamics of liquids became possible. The study of simple liquids is valuable because they have the basic behavior of liquids but do not have the

complications that arise with degrees of freedom from vibration and orientation [97].

Various studies have resulted in new insights in the structure of liquid metal surfaces [31, 98, 99, 100], especially layering of atoms at the liquid surface. By use of energy -resolved, in-plane and out-of-plane atom-surface scattering the details of the interaction of the incident atoms and those of the liquid metal surface may be examined. Many scattering experiments have been carried out for argon, neon and xenon scattering from molten indium, gallium and bismuth [59, 60, 101, 102, 103].

Atomic liquid metals, such as those listed above, have a high mass density and very smooth surfaces, thus their surfaces absorb less energy from the incident atoms than the surface of a liquid of a molecular material. Incident gas atoms are scattered into a more narrow range of angular directions. The important process in the scattering event is the transfer of energy between the surface and the incident gas atoms. The use of argon, neon and xenon to examine gallium, indium and bismuth allows the examination of scattering from the metals without complications due to structure in molecular liquids.

All three metals used in these experiments are electrically conducting in the liquid state. They have high mass densities and high heats of vaporization, as well as surface tensions. Studies of the bulk show that indium behaves as would a hard sphere liquid. Gallium seems to exhibit some layering, as may liquid bismuth. Experiment suggests that liquid gallium and indium have layering perpendicular to the surface. This extends to several atomic diameters. The atoms in the outermost layers are arranged similarly to that of hard spheres against a hard wall [100]. Experiments have also been interpreted as indicating that liquids with lower surface tensions scatter incident gas atoms more widely and that surface tension is a measure of the roughness of the liquid surface [60].

4.2 Experiment

In the experiments supersonic beams of neon, argon and xenon were produced by expanding the gas through an aperture of 0.075 mm at a temperature of 298 K. The full widths at half maxima were typically 6 : 1, whereas a Boltzmann distribution would be 1 : 2. The incident beam, at an incident angle of 55°, was chopped by a spinning slotted wheel. When the pulsed beam encounters the liquid metal surface it forms an ellipse with in-plane dimension 4.3 mm and out-of-plane dimension 2.5 mm.

The samples were 0.5 mL volume held in a stainless steel crucible. The indium and bismuth samples were washed in a 10% HCl solution and gallium was dripped through a glass pipette. The surface was then scraped by a steel wire in vacuum. Lastly, Ar^+ was sputtered at 2.0 keV. The sputtering produced a liquid surface that is flat to within 1.5° of the horizontal. Any carbon or oxygen impurities were found to remain below 1% by Auger electron spectroscopy.

Scattered atoms were detected at final angles of 45°, 55°, and 65° in the scattering plane by a double differentially pumped mass spectrometer. Total flux angular distributions were obtained by rotating a flexible, 35 cm long 1.9 cm diameter steel tube about the crucible containing the sample. When the out-of-plane angle was zero, one end of the tube, capped with a 0.32 cm aperture, was 5.4 cm from the region of interaction. The opposite end was connected to the mass spectrometer. When the out-of-plane angle was zero the in-plane angle could be varied from $-30°$ to $+80°$. The angular resolution of the detector was 3°. Atoms that entered the tube underwent multiple collisions with the walls of the tube. This resulted in a thermal velocity distribution independent of the initial velocities of the atoms.

The out-of-plane angular distributions were measured by translating the de-

tector perpendicular to the scattering plane from -0.09 to $+2.3$ cm. With this configuration the final polar angle, θ_f, changes as the detector is translated. The actual final scattering angle is $\theta_{op} = \cos^{-1}(\cos\alpha \cdot \cos\theta_f)$, with α the out-of-plane angle in the plane perpendicular to the scattering plane which is tilted by θ_f, and is equal to $\tan^{-1}(x/d)$. The solid angle for the detector also changes as the device is translated. Since the detector is translated instead of rotated the necessary correction is a multiplication of the intensities by $\left(1 + \frac{x^2}{d^2}\right)^{\frac{3}{2}}$, or $\sin^3\alpha$. This correction has a maximum value of 1.28 when $x = 2.3$ cm, the out-of-plane translation distance.

For final energy resolved distributions the raw data was in the form of time-of-flight data at $\theta_f = 45°, 55°$ and $65°$. The total flux angular distributions were at $\theta_f = -30° to + 80°$ in the scattering plane. The out-of-plane distributions were at $\alpha = -10°$ to $+25°$ perpendicular to the scattering plane. The incident angle was always $\theta_f = 55°$. The flight path length was 37.6 cm when $\theta_f = 45°$ and $65°$, and 28.8 cm when $\theta_f = 55°$.

4.3 Results

4.3.1 Argon on Gallium

A series of measured energy-resolved intensity spectra as functions of final energy for argon scattering from a liquid gallium surface at different temperatures were exhibited in Ref. [60] and an example is shown in Fig. 4.1. The detector is in the plane of scattering with equal incident and final polar angles $\theta_f = \theta_i = 55°$, the incident energy is $E_i = 95$ kJ/mol, or 0.98 eV, and the surface temperatures range from 313 to 673 K. The spectra are characterized by a single broad, asymmetric peak with a very distinct shoulder at low energies and whose full width at half

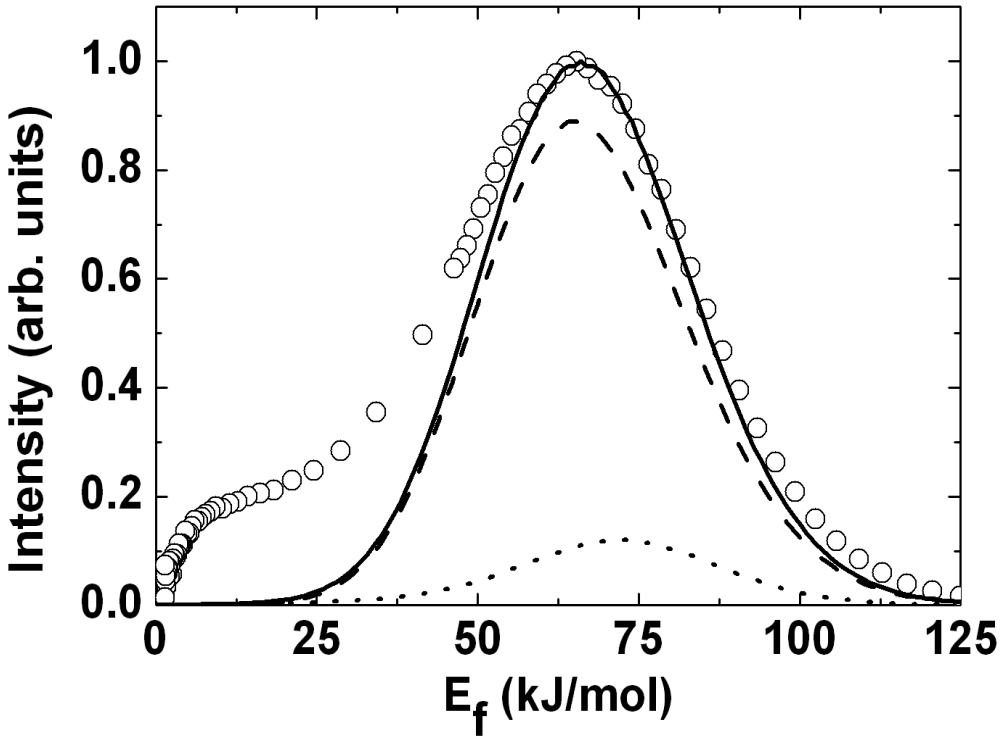

Figure 4.1: Energy resolved spectrum of Ar scattered from a liquid Ga surface with a temperature of 673 K, with $\theta_i = \theta_f = 55°$ and $E_i = 95$ kJ/mol. Experimental data are circles, total scattering calculation is the solid curve, single scattering is the dashed curve and double scattering is the dotted curve.

maximum (FWHM) increases with temperature. The peak position, or most probable final energy, is at about two-thirds of the incident energy indicating a substantial average energy loss to the surface. Calculations using Eq. (2.6) are shown as the solid curve [104]. This is the sum of the single collision contribution of Eq. (2.2) shown as a dashed curve and the double collision contribution which is smaller is shown as a dotted curve.

The low-energy shoulder evident in the data of Fig. 4.1 is not produced by

the smooth-model multiple collision calculation used here because the form factor of Eq. (2.5) becomes too small at very low energies and supresses this feature. This shoulder is due to double back-scattering trajectories in which the incident particle is first scattered backwards nearly parallel to the surface and then scattered forward into the detector by the second collision as has been demonstrated by calculations based on hard-sphere scattering [55] .

The calculations show essentially no shift in position of the most probable final energy with increasing temperature, in agreement with the experiment for which the position varies by no more than 2 kJ/mol over the whole range of temperatures measured. There is a marked increase in width of the peak with increasing temperature and this is discussed further below in connection with Fig. 4.2. The value of $\Delta\Omega/4\pi$, where $\Delta\Omega$ is the solid angle subtended by the second atom as viewed from the initial collision, used in the calculations was 0.162 which was calculated from Eq. (2.7) using the covalent radii of argon $a_{Ar} = 0.126$ nm and gallium $a_{Ga} = 0.098$ nm and an average interatomic spacing of $d = 0.278$ nm for the liquid. The value of v_R was chosen to be 600 m/s for all calculations of the Ar/Ga system, compared to 2740 m/s for gallium at its melting point.

For calculations of all three rare gas probes on gallium it was necessary to choose M_C to be an effective mass equal to 1.65 times the mass of a single Ga atom [104]. The reason for this lies in the sensitivity of the most probable energy to M_C, and if a smaller effective mass is used the calculated most probable final energy becomes significantly smaller than that observed. This need for a larger effective mass with Ga contrasts with the In and Bi results treated below, where M_C was always chosen equal to the atomic mass of the liquid metal.

The temperature dependence of the FWHM for the energy-resolved spectra of Fig. 4.1 for Ar/Ga scattering are shown in Fig. 4.2. The data, shown as open circles,

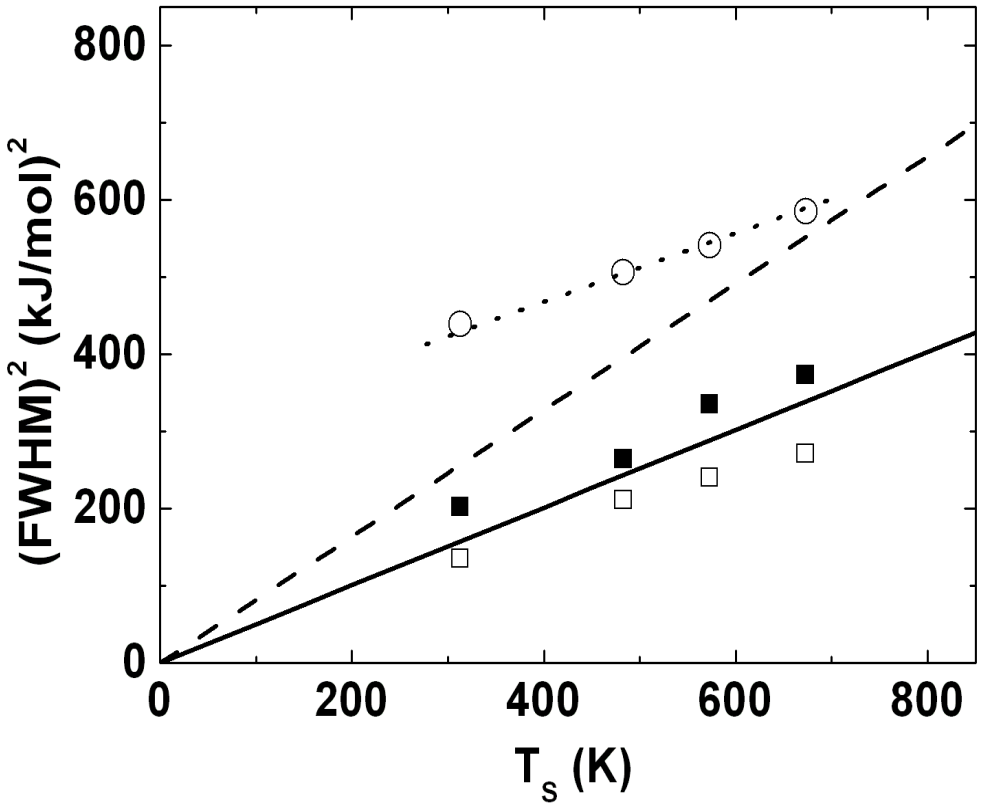

Figure 4.2: Temperature dependence of the squared FWHM for Ar scattered from a liquid Ga surface with $\theta_i = \theta_f = 55°$ and $E_i = 95$ kJ/mol. The solid line is the Gaussian approximation of Eq. (3.2) and the dashed line is the trajectory approximation. Data are circles, calculated single scattering is open squares and total scattering is solid squares. The dotted line is a linear fit to the total scattering with a constant added for comparison with the slope of the data.

show the expected very nearly linear dependence of the squared FWHM with surface temperature. Both single and single plus double scattering calculations, shown as open and filled squares, respectively, show a similar linear dependence with nearly the same slope, but smaller by a constant value over the whole temperature range [104]. The constant difference of about 300 kJ^2/mol^2 between experiment and calculations implies that this must be due to a mechanism that does not involve thermal processes, i.e., it is not due to phonons or low energy electron-hole pair excitation.

In Fig. 4.2 is shown the temperature dependence of the full-width-at-half-maximum for the system [104]. It can be seen that the temperature dependence of the data and calculations agree well for temperatures up to approximately 400 K. For completeness, the approximation of Eq. (3.2) and the trajectory approximation are also shown in Fig. 4.2.

Angular distributions for Ar/Ga are shown in Fig. 4.3. These are compared with calculations, shown as solid curves, which are the integral of Eq. (2.2) over all final energies [104]. Fig. 4.3 shows both in-plane and out-of-plane angular distributions for an incident energy $E_i = 92$ kJ/mol, or 0.954 eV and $\theta_i = 55°$ for three different surface temperatures ranging from 308 to 586 K. In this case, the good agreement between measurement and theory indicates that there is little or no diffuse, equilibrium component in the scattering distributions because this would be expected to appear as a $\cos\theta_f$ contribution. Fig. 4.4 shows as open circles an in-plane angular distribution for Ar/Ga measured at a temperature of 586 K with an incident energy corresponding to a room temperature jet beam with $E_i = 6$ kJ/mol, or 0.062 eV and $\theta_i = 55°$. In this case the scattered intensity is spread over a much larger angular range, indicating that there is significant adsorption with subsequent desorption. It is usually assumed that the desorbed particles leave in equilibrium with the surface, and the filled circles are the same data with a fraction of a Knudsen equilibrium flux

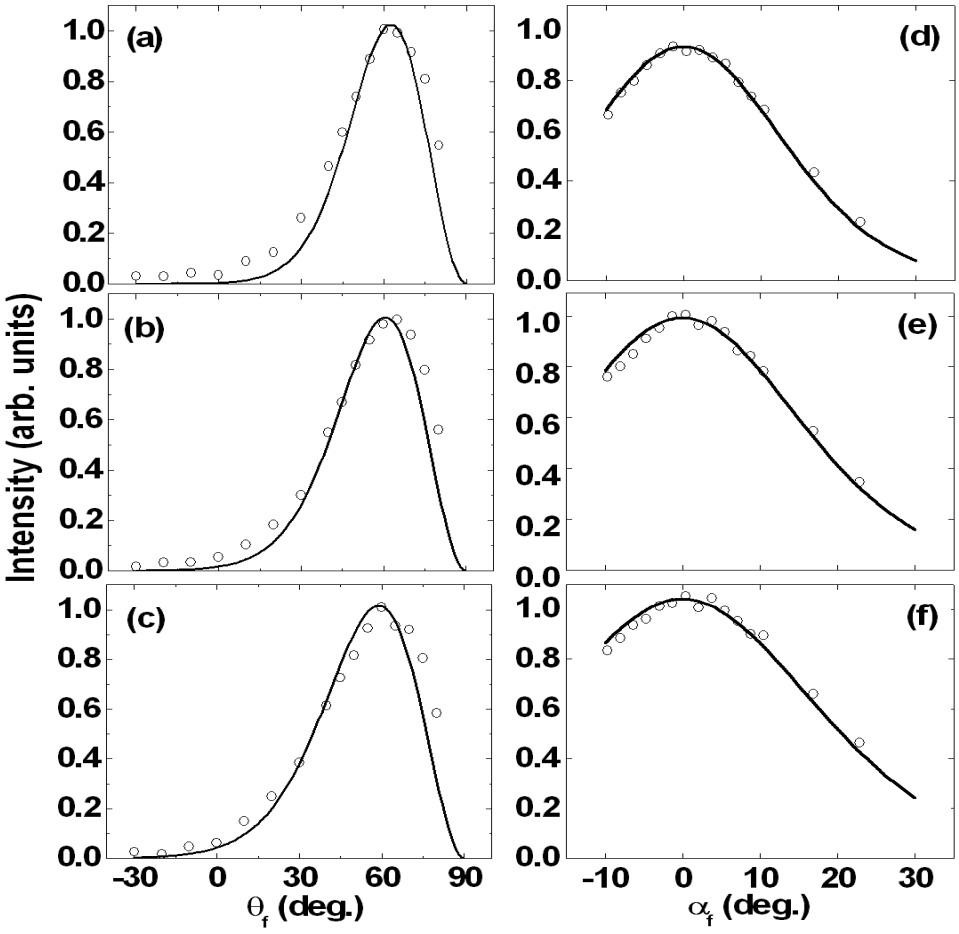

Figure 4.3: In-plane (left panels) and out-of-plane (right panels) angular distributions for Ar/Ga with $\theta_i = 55°$ and $E_i = 92$ kJ/mol for three different values of surface temperature: (a and d) 308 K, (b and e) 436 K, (c and f) 586 K. Data are circles and calculations are the solid curves.

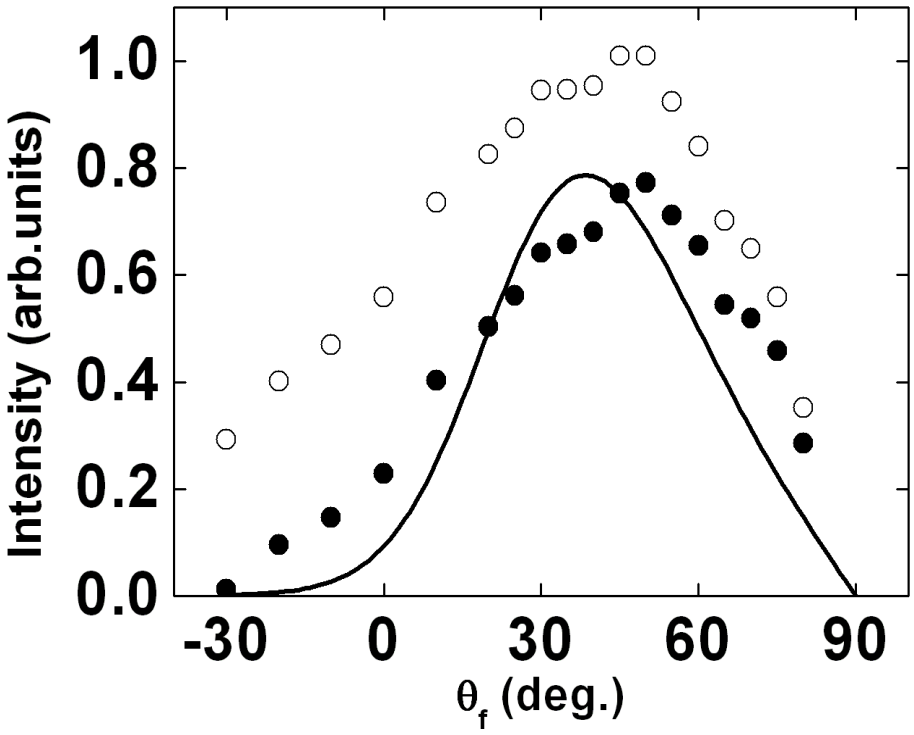

Figure 4.4: In-plane angular distribution for Ar/Ga with $\theta_i = 55°$ and $E_i = 6$ kJ/mol for a surface temperature of 586 K. Data are open circles, data with a fraction of the equilibrium cosine distribution subtracted are filled circles. Theoretical calculations are the solid curve.

distribution subtracted, this fraction being equal to 43% at 308 K, 40% at 436 K, and 35% at 586 K. The solid curve is the calculation, which in this case includes an attractive physisorption well of depth $D = 60$ meV (5.8 kJ/mol). Although the agreement is not as good as for the higher energy case of Fig. 4.3, the position and widths of the peaks at all measured temperatures are reasonably well explained [104]. Fig. 4.5 shows an energy-resolved distribution at the same low energy of $E_i = 6$ kJ/mol, or 0.062 eV with $\theta_i = \theta_f = 55°$ and a surface temperature of 586 K. The calculations for

$D = 60$ meV are shown as a dashed curve and the solid curve is calculated for $D = 0$. The calculations do not fit the low energy part of the data which may be due to a trapping-desorption component which is not calculated [104]. A trapping-desorption component might be expected since the estimated well depth is comparable to the incident energy.

4.3.2 Neon and Xenon on Gallium

Figures 4.6 and 4.7 show examples of angular distributions for neon and xenon scattering from liquid gallium at a surface temperatures of 586 K with $E_i = 6$ kJ/mol and $\theta_i = 55°$. For Ne/Ga of Fig. 4.6 no fraction of a Knudsen distribution was subtracted from the data, a well depth $D = 10$ meV was included in the interaction potential and $v_R = 900$ m/s. This well depth is somewhat smaller than the typical value obtained for Ne adsorption on a range of other metal surfaces where it is measured or estimated to be of order 30 meV [105, 106] . The agreement of calculations with the data for Ne/Ga in Fig. 4.6 is not as good as most of the angular distributions [104]. Subtracting a small Knudsen distribution from the data does not result in better agreement. This implies that if trapping-desorption processes are the reason for this disagreement, and such processes are likely because of the low incident energy, they result in non-equilibrium (non-cosine) component to the scattering. However, the qualitative agreement for Ne/Ga implies that predominantly direct scattering processes are involved in the collision, as has been noted previously for Ne scattering from many metal surfaces [60] .

For Xe scattering the diffuse component was dominant and the subtracted equilibrium fraction measured temperatures was was 96% at 308 K, 92% at 436 K, and 90% at 586 K [104]. The well depth was chosen as 100 meV and $v_R = 300$

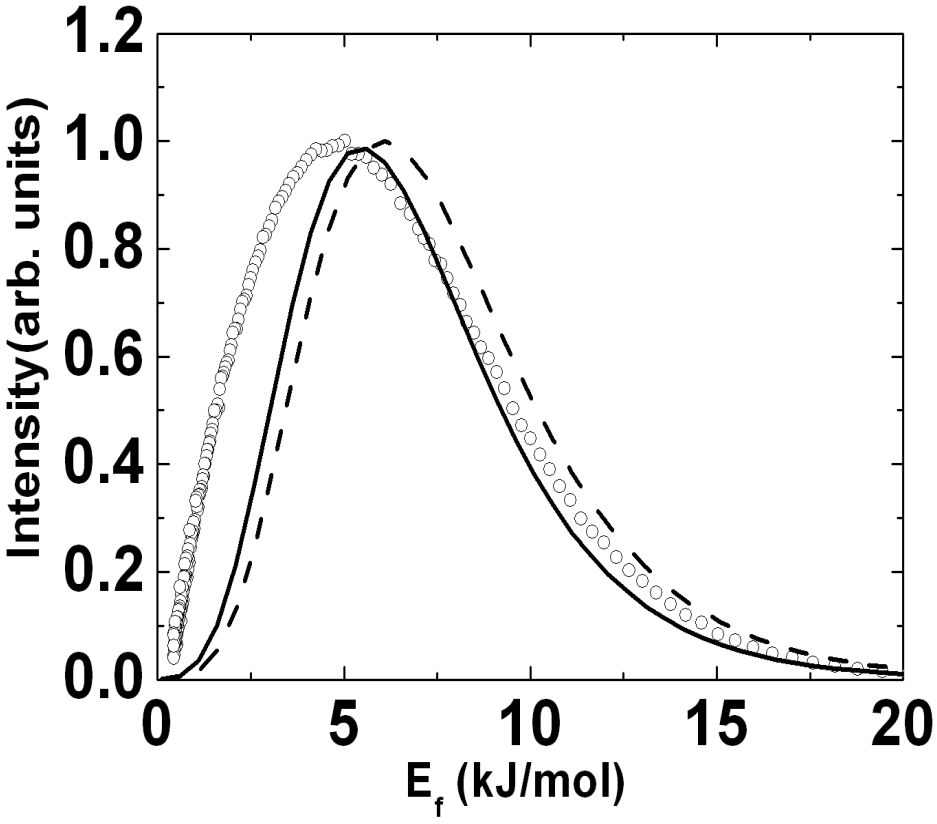

Figure 4.5: Energy resolved spectra for Ar/Ga for $E_i = 6$ kJ/mol, surface temperature 586 K and $\theta_i = \theta_f = 55°$. Calculations for $D = 60$ meV are the dashed curve, calculations for $D = 0$ are the solid curve and data are open circles.

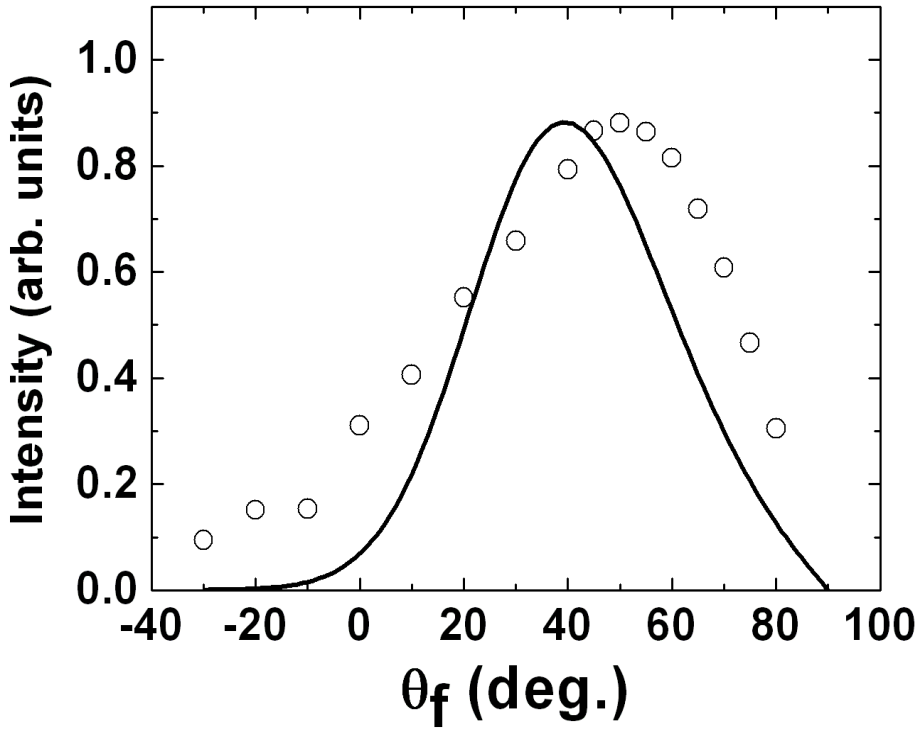

Figure 4.6: In-plane angular distribution spectrum for Ne/Ga at a surface temperature surface temperature 586 K with $\theta_i = 55^\circ$ and $E_i = 6$ kJ/mol. Data are circles and the calculation is the solid curve.

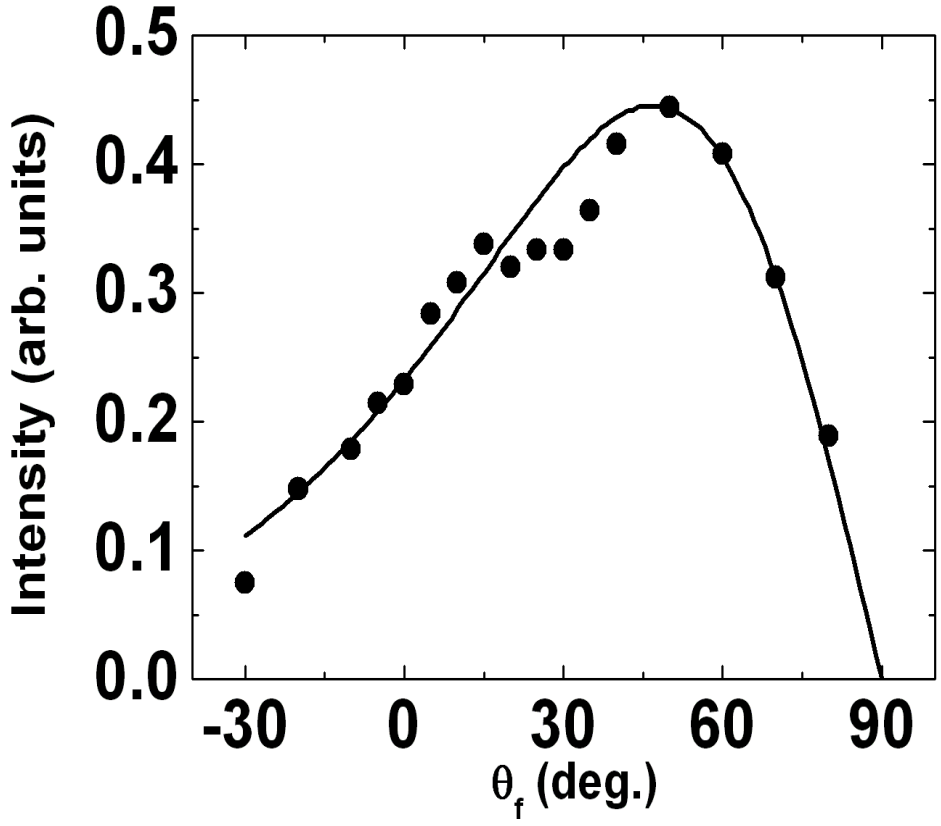

Figure 4.7: In-plane angular distribution spectrum for Xe/Ga for surface temperature surface temperature 586 K with $\theta_i = 55^\circ$ and $E_i = 6$ kJ/mol, $v_R = 300$ m/s and an interaction well depth of 100 meV. Data, after subtraction of an equilibrium component, are shown as filled circles and the calculation is the solid curve.

m/s. This value for the interaction potential well depth is in basic agreement with results for Xe adsorption on many metal surfaces as determined from measurements of sticking coefficients and heats of adsorption [105, 106, 107] in which D ranges approximately from 100 to 300 meV.

For both Ne and Xe, just as for Ar, an effective mass of 1.65 Ga atoms was used. As in the case of Ar scattering, the widths and positions of the large, broad peaks are in reasonable agreement with measurements [104]. For the case of Xe the data exhibit a small shift in the most probable final angle towards the surface normal with increasing temperature that is well explained by the calculations. For the case of Ne a similar shift is predicted by the theory but a somewhat smaller shift appears in the measurements.

4.3.3 Argon on Bismuth

High energy angular distributions and an energy-resolved spectrum for argon scattering from liquid bismuth are presented in Fig. 4.8. The in-plane and out-of-plane angular distributions are for an incident energy of 92 kJ/mol and an incident angle of 55°, while the energy-resolved data are for the slightly higher energy of 95 kJ/mol with both incident and final angles fixed at 55°. The calculations are shown as solid curves, with the single and double scattering contributions denoted as in Fig. 4.1. The value of $v_R = 350$ m/s. In this case the surface effective mass is taken to be the same as a single Bi atom, and the agreement between theory and measurement is equally good as obtained for the Ar/Ga case [104]. Fig. 4.9 gives an in-plane angular distribution and an energy-resolved spectrum for a low energy 6 kJ/mol beam of Ar scattering from liquid Bi. The calculations for the in-plane angular distributions are similar to those for Fig. 4.8 above except that in this

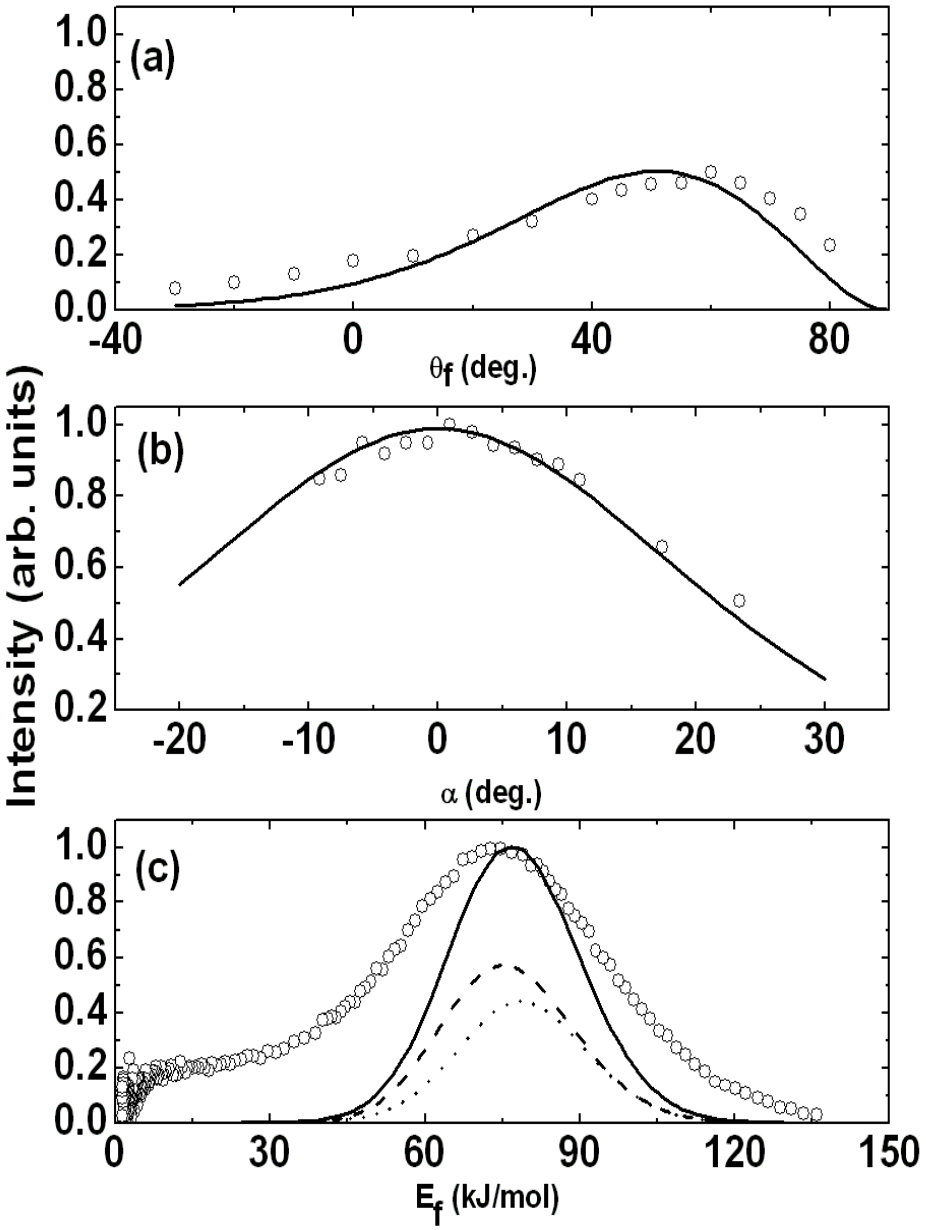

Figure 4.8: In-plane, out-of-plane and energy-resolved spectra for Ar/Bi: (a) In-plane spectra angular distribution with $\theta_i = 55°$, $E_i = 92$ kJ/mol, surface temperature 586 K, (b) out-of-plane angular distribution for $\theta_i = 55°$, $E_i = 92$ kJ/mol, surface temperature 586 K, (c) Energy resolved spectrum for $\theta_i = \theta_f = 55°$, $E_i = 95$ kJ/mol, surface temperature 573 K, with the theory curves as in Fig. 4.1. Data are open circles.

case calculations for three different well depths are presented, $D = 0$, 10, and 100 meV [104]. The relatively small well depth of 10 meV gives reasonable agreement with the energy-resolved spectrum. In the angular distribution, calculations with the smaller well depth do not explain the rather large intensity in the neighborhood of θ_f near the surface normal, but this discrepancy may be due to the presence of an equilibrium $\cos\theta_f$ component [60] which was not subtracted from the data in Fig. 4.9.

4.3.4 Argon on Indium

Examples of all three types of scattering distributions for argon scattering from liquid indium at the higher incident energy are shown in Fig. 4.10. As in previous work on this system [51, 52] the theory, with $v_R = 450$ m/s (2215 m/s at melting), explains the in-plane data reasonably well, and it is seen that this holds true also for the out-of-plane angular distribution [104].

Fig. 4.11 shows additional data and calculations for angular distributions taken at surface temperature 436 K and three different energies. The calculations for the lowest energy of 6 kJ/mol (0.062 eV) include a potential well with $D = 100$ meV [104].

4.3.5 Neon on Indium

Figure 4.12 shows all three types of scattering distributions for the case of neon on indium at low energy. The temperature is surface temperature 436 K, $E_i = 6$ kJ/mol, $\theta_i = 55°$ and the out-of-plane distribution was taken at a final in-plane polar angle also of 55°. The calculations, shown as solid curves, used $v_R = 800$ m/s and a well depth $D = 20$ meV [104]. Also shown in the energy resolved spectrum

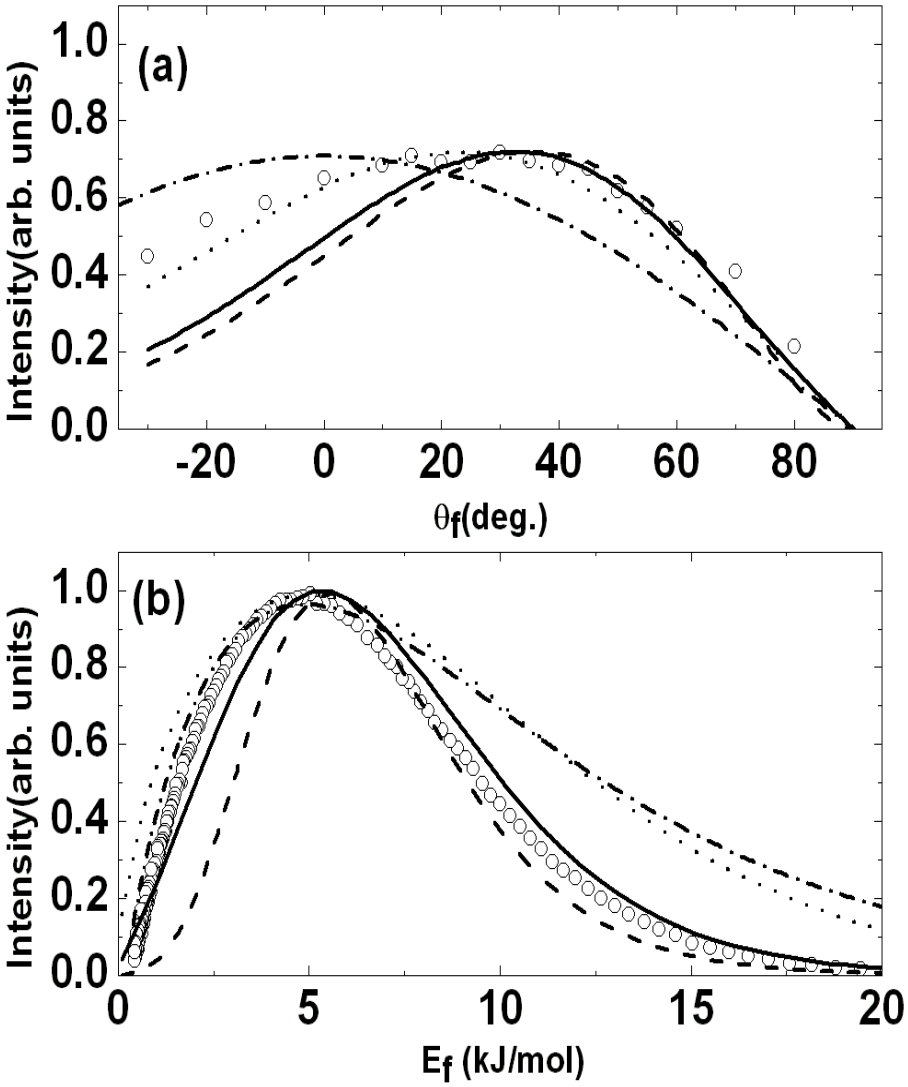

Figure 4.9: In-plane and energy resolved spectra for Ar/Bi for $E_i = 6$ kJ/mol and surface temperature 586 K: (a) in-plane angular distribution for $\theta_i = 55°$, (b) energy resolved spectrum for $\theta_i = \theta_f = 55°$. Data are circles and theory with well depth zero are the dashed curves, theory with well depth 10 meV are the solid curves, theory with well depth 100 meV are the dotted curves. A Knudsen distribution is shown in each panel as the the dash-dot curve.

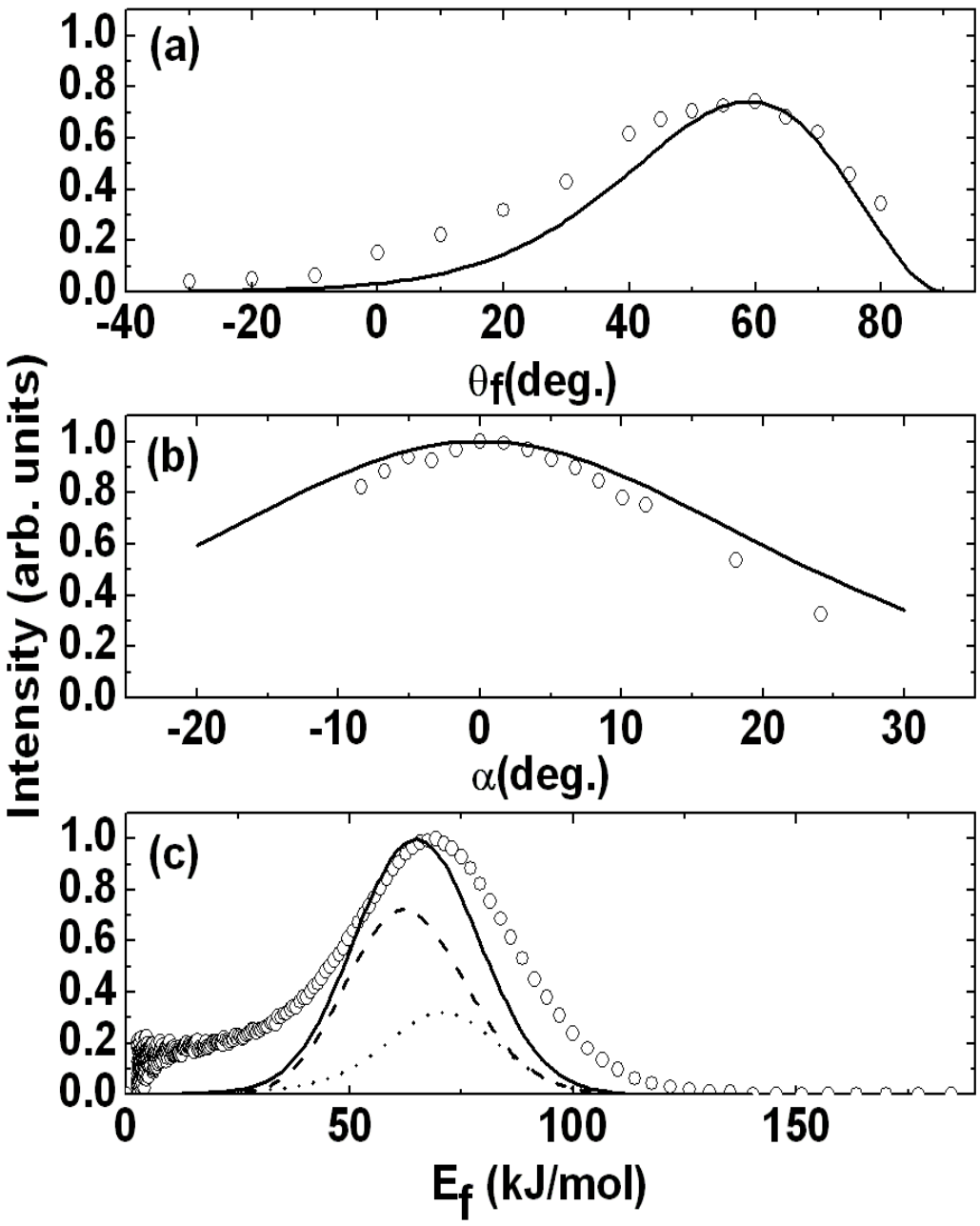

Figure 4.10: Ar/In: (a) in-plane angular distribution, and (b) out-of-plane angular distribution, both for $\theta_i = 55°$, $E_i = 92$ kJ/mol and surface temperature 586 K. (c) energy resolved spectrum for $\theta_i = \theta_f = 55°$, $E_i = 95$ kJ/mol and surface temperature 436 K.

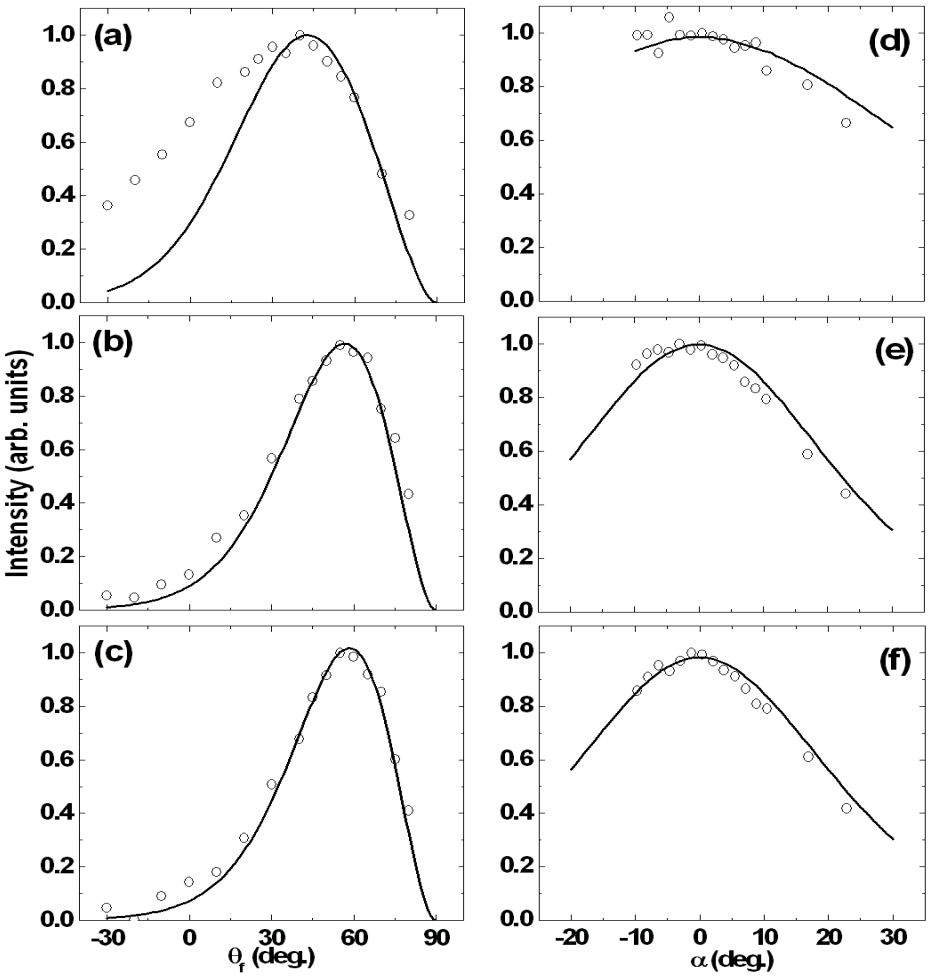

Figure 4.11: Angular distributions for Ar/In for $\theta_i = 55°$, surface temperature 436 K and three different incident energies, (a) 6 kJ/mol , (b) 42 kJ/mol , (c) 92 kJ/mol. On the left are in-plane angular distributions and on the right are out-of-plane distributions measured starting from the in-plane polar angle $\theta_f = 55°$. Data are open circles and calculations are solid curves.

of Fig. 4.12(c) is a calculation for $D = 0$ and the calculation with $D = 20$ meV which is in significantly better agreement with experiment. The in-plane angular distribution of Fig. 4.12(a) is in qualitative agreement with the data in a manner similar to the low-energy case of Ne/Ga of Fig. 4.6, and again the same explanation for the lack of quantitative agreement may apply.

4.4 Conclusions

In this chapter a classical theory of atomic scattering from surfaces has been used to analyze newly available data [60, 108] for the rare gases Ne, Ar and Xe scattering from liquid metal surfaces [104]. Previously, it has been shown that such theories can do a reasonable job of describing the observed features of rare gas scattering from surfaces [51, 52], but the newly available data provides the opportunity to test the theory over a much wider range of scattering systems and initial conditions. Additionally, the new data includes measurements of angular distributions out of the plane of scattering, providing data from a region of phase space that has not been investigated before. One major difference with the theoretical approach taken here is that all scattering is described with a single consistent model. In the previous work total intensity angular distributions were calculated with the smooth surface model [52] of Eq. (2.2) while energy-resolved intensity spectra were calculated with the different classical expression, Eq. (2.1) which is more appropriate for a surface of discrete scattering centers [51].

The energy range over which measurements were made was quite large, from 6 to 100 kJ/mol, while the incident and final angles for energy resolved and out-of-plane measurements were always in the neighborhood of the the specular position with $\theta_i = 55°$. In general, the comparisons of theory with the measurements were

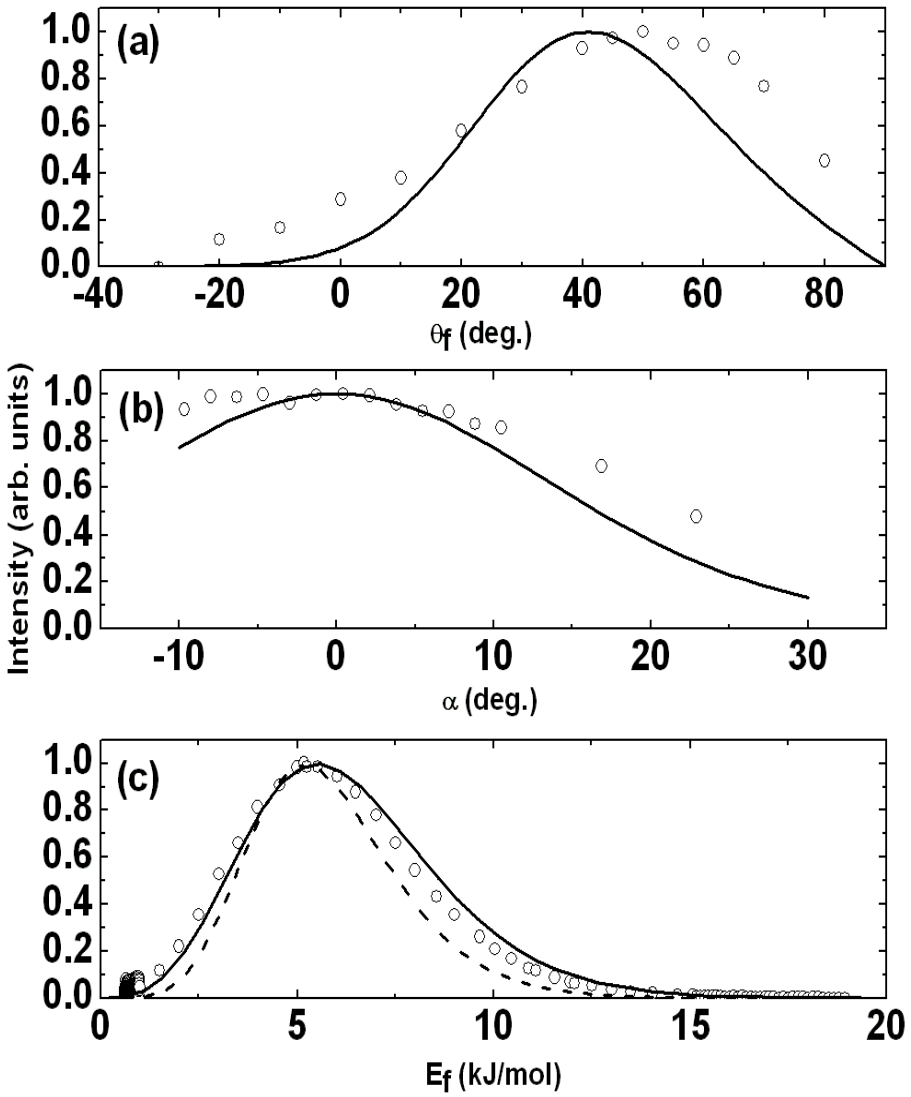

Figure 4.12: Ne/In distributions for $E_i = 6$ kJ/mol, $\theta_i = 55°$ and surface temperature 436 K. (a) in-plane angular distribution, (b) out-of-plane angular distribution, and (c) energy resolved spectrum for $\theta_f = 55°$, showing calculation for $D = 0$ meV with a dashed curve, all other calculations are for $D = 20$ meV shown as solid curves.

good, especially for the higher incident energies. Good agreement was obtained with the new, out-of-plane measurements [104].

The theoretical expression of Eq. (2.2) predicts that the FWHM of the energy resolved spectra should increase very nearly with the square root of the surface temperature, and this is clearly seen in Fig. 4.2.

For the gases Ar and Xe at the low incident energy of 6 kJ/mol there was a diffusive component in the scattered intensity that could be associated with trapping and subsequent desorption from the attractive physisorption well. This component was particularly strong for Xe scattering. Upon assuming that the trapping-desorption fraction escapes with an equilibrium Knudsen flux distribution at the surface temperature, the present theoretical comparisons are in good agreement with measurements [104].

At low energies, the physisorption well of the potential not only gives rise to trapping and desorption, but it can also have a significant effect on both the angular and energy-resolved scattering distributions largely because of the refraction of the projectile towards a more normal incidence angle and its increased energy as it collides with the surface inside the well. In the present theory, the physisorption was modeled by a square well which is adequate for describing the refraction and enhanced energy in classical scattering [104]. Comparisons with the data at low incident energies provides predictions of well depths for many of the gas-metal combinations, and these results are presented in Table 4.1. Although no direct experimental measurements exist for the physisorption well depths for these combinations of rare gases and liquid metals, the values obtained here are quite reasonable with the possible exception of Ar/Bi and are of the same order of magnitude as well depths for the same rare gases measured or predicted for other metal surfaces [105, 106, 107] . For the case of Ar on Bi, the well depth value of 10 meV was obtained from the calculations for the energy-resolved

Table 4.1: Table of adsorption well depths for rare gasses interacting with molten metal surfaces that could be estimated by comparisons with the scattering data, in dimensions of meV.

	Ga	In	Bi
Ne	10	20	–
Ar	60	100	10
Xe	100	–	–

data of Fig. 4.9(b). This value seems small in comparison with expected values of well depths for Ar interacting with metal surfaces. In fact, the comparison of calculations with the angular distribution of Fig. 4.9(a) would indicate a larger well depth that could be as large as 100 meV.

The authors of Ref. [60] made the interesting suggestion that differences in surface tension may be the cause of some of the features observed in the scattering spectra. In particular, for the case of Ar angular distributions they observed that the peak in-plane scattered intensity decreased with the order Ga>In>Bi, and the corresponding peak widths increased with the same ordering. Since this is also the order of decreasing strengths of the surface tensions of the three liquids, they argued that a larger surface tension resulted in a flatter surface, hence a sharper and narrower scattered angular distribution. The present calculations fail to produce the observed ordering in the Ar angular distributions [104]. In fact the calculated order of the peak intensities is exactly the reverse, i.e., they decrease in the order Bi>In>Ga and this behavior can be ascribed to the differences in the liquid atom masses. It is possible to calculate the correct ordering, but only with v_R parameter choices that are quite different from those used here [60] , but these different parameter values do not give rise to the relatively good agreement with all of the scattered spectra shown here.

It is possible to assign a correlation length to the collision through the Gaussian

like term in parallel momentum transfer of Eq. (2.2), which can be regarded as having a decay length R_C whose value is given by $R_C = \hbar v_R/\sqrt{2k_B T_S \Delta E_0}$ [87]. The length R_C is proportional to v_R and it might be considered of interest to try to relate surface tensions to such a correlation length, especially since for the present calculations the v_R parameters for Ar (and hence the correlation lengths) decrease in the order Ga>In>Bi the same as the ordering of the surface tensions. However, for all cases considered here the correlation lengths are very short, less than the average spacing between liquid atoms. Thus, it is unlikely that the present calculations can lend support to arguments based on differences in surface tension. The theory used here is based on a description of the scattering process that involves collisions with only one liquid atom at a time and is highly localized in time and space, as indicated by the very short correlation lengths. However, this suggests that experiments carried out in the quantum mechanical regime such as low energy He atom scattering, which would have much larger correlation lengths, might be sensitive to differences in surface tension.

One interesting result observed here in connection with the liquid Ga surfaces is that the energy resolved spectra for all three rare gases could not be made to agree with measurements unless an effective mass for the surface of 1.65 Ga atoms was used [104]. For In and Bi the surface mass of a single metal atom was satisfactory. This larger effective mass is suggestive of a collective effect, in which the incoming rare gas pushes on a mass involving more than one metal atom. The presence of such a collective effect seems to be supported by independent measurements [91] that show that Ga, in contrast to In and Bi, exhibits an unusually large amount of quasi-ordered layering in the liquid state and this layering persists to relatively large temperatures.

There remains the question of whether this collective effect involves atoms in layers of the liquid beneath the surface, or whether it is with other atoms in the surface

layer. Interestingly, one other metallic surface examined with atomic and molecular scattering has also required a larger effective mass. This is Ru(0001), discussed in Ch. 3 above, where considerable data is available for scattering of Ar [82] and N_2 [89] under incident energy and angular conditions similar to those used here. For both of these systems, in order to obtain agreement between the data and calculations similar to those considered here, it was necessary to choose an effective mass for the Ru surface that was larger than two Ru atomic masses [87, 109].

Interestingly, the experiments on N_2/Ru(0001) were able to make independent measurements of the energy associated with normal and parallel motion of the scattered molecules. Comparisons of calculations with these measurements indicated that the collective effect in that system was with Ru atoms in layers beneath the surface, and not with multiple atoms in the surface layer. Unfortunately, the present rare gas scattering experiments were not taken over a large enough range of initial and final angles to permit investigation of this dependence in the liquid metals. In order to examine the spatial dependence of the effective mass effect the ideal experiments would be to contrast measurements made with near-normal incident and final angles with measurements made at grazing incident and final angles. It would also be possible to explore this more fully using angular combinations in which one of the two angles θ_i and θ_f was alternately located near normal with the other angle close to surface grazing conditions.

One could raise the question of whether detailed calculations, such as molecular dynamics simulations carried out with more realistic and reliable potentials of the molten metal surfaces, could reveal more information about the mass dependence. Two such studies of Ar scattering from molten metal surfaces have already been reported, one using Lennard-Jones potentials [103] and the other using embedded atom potentials [110], but the calculated angular distributions and energy resolved spectra

were no better than those obtained with the methods used here. It is doubtful that atom scattering experiments in the classical, multiphonon regime such as those considered here will be able to adequately sort out the microscopic origins of the effective mass. This would be better addressed through experiments capable of measuring single quantum excitations of vibrational modes such as inelastic He atom scattering or electron energy loss spectroscopy (EELS). Comparisons of theoretical calculations to inelastic scattering spectra using reliable potentials should reveal details of the mass dependence and should also reveal the importance of surface tension, especially if evidence for surface capillary waves could be found.

There is also a second reason for suggesting experiments over a large range of incident and final angles and this has to do with the determination of the velocity parameter v_R. This parameter is completely defined in terms of a weighted average over all phonon modes parallel to the surface. Thus measurements of v_R could, in principle, provide useful information about the surface phonon spectral density and hence about the dynamics of the atoms at the liquid surface. It has been pointed out [57], as discussed above in Ch. 2, that a much better way of determining accurate values of v_R would be through comparisons of calculations with experimental data taken, first at nearly specular conditions such as is the case in the experiments considered here, and then compared with measurements taken at angles that differ significantly from specular conditions.

Chapter 5

Corrugation

5.1 Introduction

Over the years several models of the gas-surface interaction have been used to study experimental data. The simple hard-cubes model [111, 112], an improvement on the calculations of Goodman [113], has been used often. It assumes an impulsive atom-surface interaction. The generalization to the soft-cube [112], which includes an interaction potential well and a harmonic binding force on the cube, achieves reasonably good results. Other improvements include the replacement of the spherical incident gas particle by an ellipsoid [114, 115] and a rigid rotator [116]. These modifications were to account for rotational excitation of scattered molecules. In-plane forces have been included by means of hard-sphere [113], capped-sphere and frictional cubes [117]. For some time the corrugation of surfaces has been studied by means of the washboard model developed by Tully [118, 119] as an extension of the simple hard-cubes model by inclusion of a surface corrugation, and an effective surface object modelled as an ellipsoid. One may question the need for another model of surface attempting to account for surface corrugation in the gas-surface interaction.

All of the above models have been used with moderate, though often only qualitative success, and the washboard model is still used. More quantitative success is desirable.

Relatively recently the washboard model has been used to analyze data from argon scattering from ruthenium with modest success [82, 83]. In order to improve upon this situation, the classical Wigner formalism has been used to examine the angular scattering from corrugated surfaces and its temperature dependence with good qualitative results [120, 121]. This approach results in a theory with three free parameters. The scattering of argon from hydrogen saturated tungsten has been examined with an extension of this theory based on the Wigner formalism [122], resulting in a theory with six free parameters. A theory with a minimum number of uncontrolled parameters is desirable.

Roughness of the surfaces of liquids and liquid metals and its effect on gas-surface interactions has been examined in experiments [59, 102, 123]. While most of this work involved molecular liquids, such as perfluorinated polyether and squalene [102, 123, 124], atomic liquids of molten indium, gallium and bismuth have been examined by means of atomic scattering of neon, argon and xenon [59, 60, 101, 103]. The most complete set of data is for the argon-gallium system. In this chapter the model of Eq. (2.47) is used to examine the argon-gallium data [60]. While this data is from scattering from a liquid metal and is not expected to be appropriate for analysis with the one-dimensional theory used here, it is used to provide a benchmark for the behavior of the theory. It is seen that the temperature dependence of the most probable intensity of energy-resolved data may be used to estimate the surface corrugation. The present theory is an improvement over the earlier empirical $1/T_S$ temperature dependence [51]. The peak-to-trough distance of the corrugated surface is seen to be reasonably close to the expected 10% of the interparticle spacing, often used as an estimate of the rms value of the vibrational displacement necessary in order to achieve

melting [125, 126, 127]. The corrugation experienced by the incident atom is seen to increase with increasing incident energy. This is to be expected because the locus of classical turning points is farther from the surface for lower incident energies. Double scattering reproduces the low energy feature seen in the energy-resolved scattering data. In-plane and out-or-plane scattering agree well with the data for reasonable values of surface corrugation amplitude.

5.2 Results

The temperature dependence of the most probable intensity of energy-resolved scattering of argon from liquid gallium at incident energy of 95 kJ/mol and $\theta_i = \theta_f = 55°$ is shown in Fig. 5.1. Calculations are the solid curve for corrugation amplitude $h = 0.08$. Data are open circles. For comparison the temperature dependence of the smooth surface and discrete, uncorrelated scatterers are shown. The calculations are normalized to agree at $T_S = 313$ K. The theory is seen to agree well with the temperature dependence of the data for $h = 0.08$. Using an interparticle spacing for gallium of 2.78 Å, this value of the corrugation amplitude gives a peak-to-trough distance of 0.44 Å, and the rms value of the height above the surface plane is 0.16 Å. In either case, the value agrees well with the expected value for melting, 0.28 Å. As the corrugation amplitude approaches zero the temperature dependence become that of the smooth surface model.

The temperature dependence of the most probable intensity of energy-resolved scattering of argon from liquid gallium at incident energy of 42 kJ/mol, $\theta_i = \theta_f = 55°$ is shown in Fig. 5.2. The calculations are normalized to agree at $T_S = 309$ K. Calculations are seen to agree well with data. The corrugation amplitude of 0.07 gives a peak-to-trough distance of 0.38 Å, and the rms value of the height above the surface

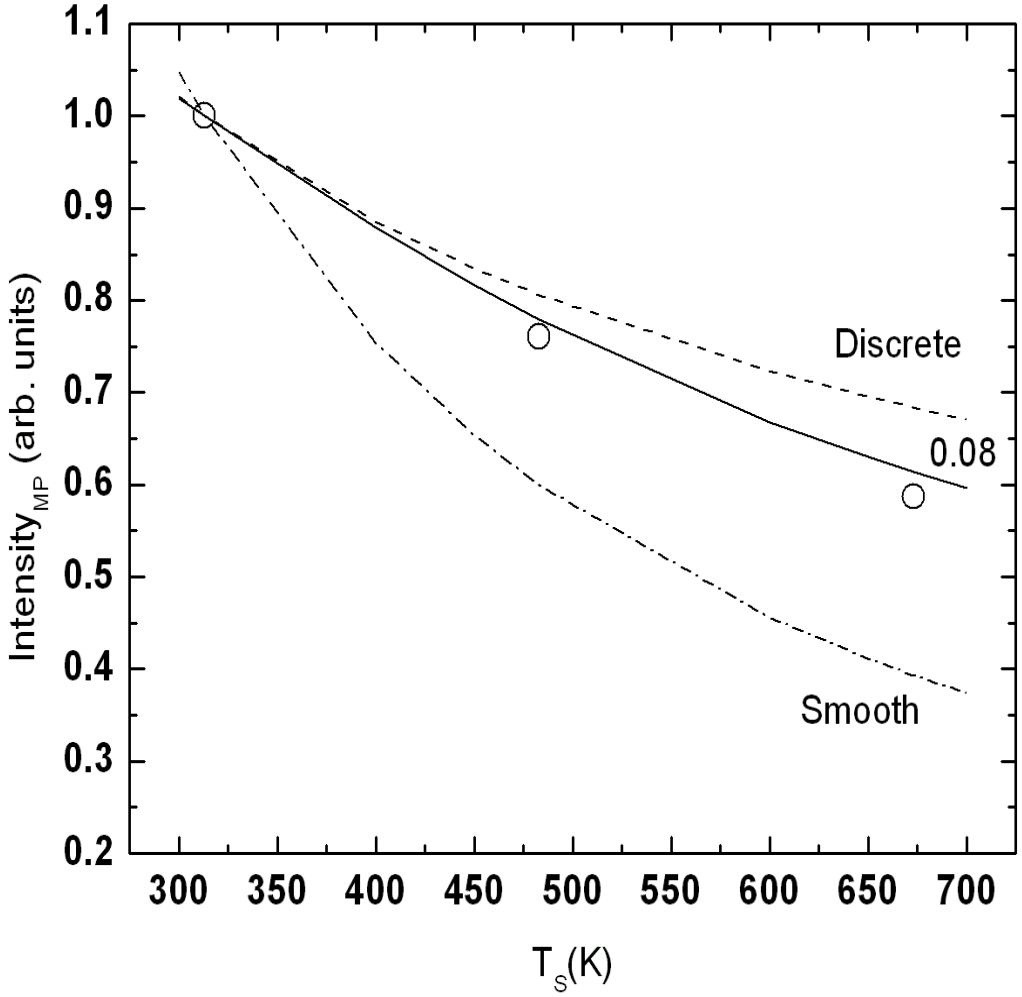

Figure 5.1: The temperature dependence of most probable intensity of energy-resolved spectra for Ar/Ga with $\theta_i = \theta_f = 55°$, $E_i = 95$ kJ/mol, $T_S = 313, 483, 673$ K. Calculations are the solid curve for corrugation amplitude $h = 0.08$. Data are open circles. For comparison, the temperature dependence of the smooth surface (dash dot) and discrete, uncorrelated scatterers (dash) are also shown.

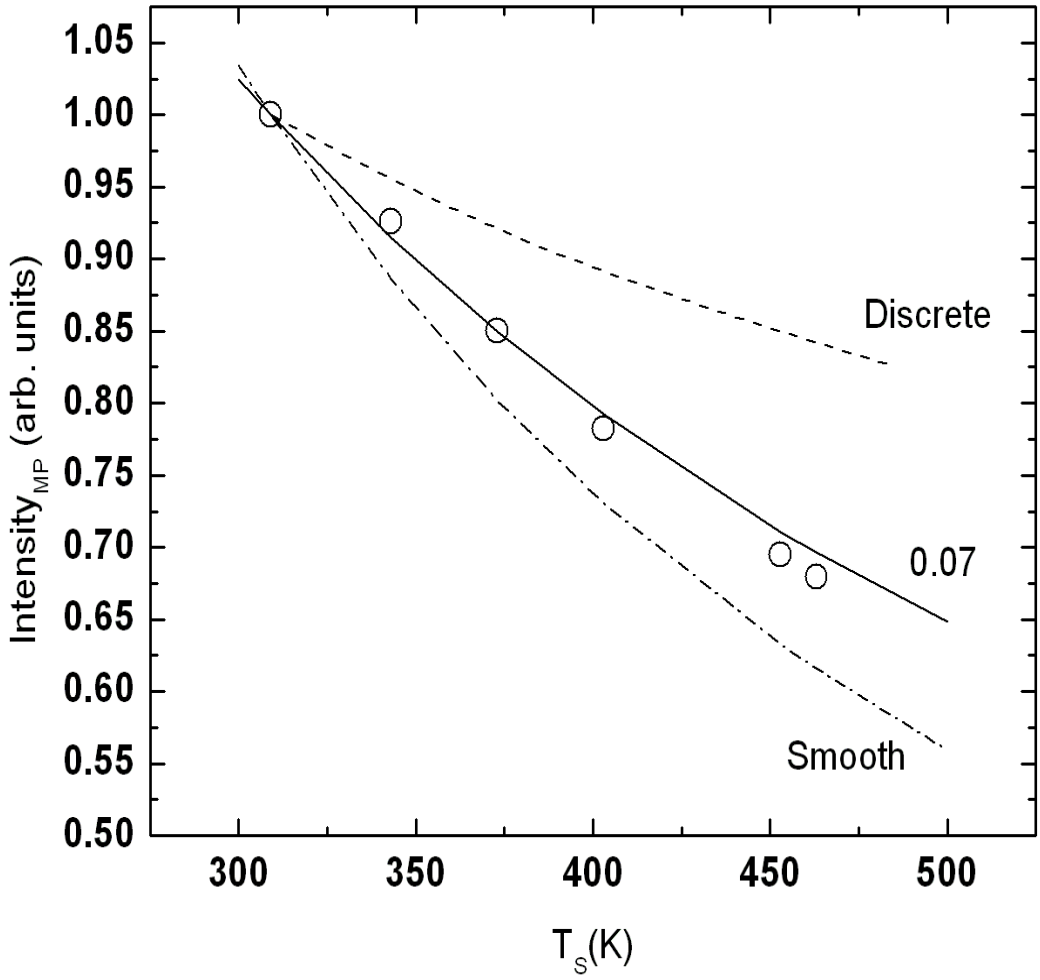

Figure 5.2: The temperature dependence of the most probable intensity of energy-resolved spectra for Ar/Ga with $\theta_i = \theta_f = 55°$, $E_i = 42$ kJ/mol, $T_S = 309, 343, 373, 403, 453, 463$ K. Calculations are the solid curve for corrugation amplitude $h = 0.07$. Data are open circles. For comparison, the temperature dependence of the smooth surface (dash dot) and discrete, uncorrelated scatterers (dash) are also shown.

plane is 0.13 Å. This smaller value of h is in agreement with the expectation that the incident atom encounters a weaker interaction with the surface due to a smaller incident energy. This results in a relatively smoother locus of classical turning points.

The case showing the importance of double collisions is shown in Fig. 5.3 for argon scattering from gallium at incident energy $E_i = 95$ kJ/mol, $\theta_i = \theta_f = 55^\circ$ and $T_S = 673$ K. Calculations are the solid curve for corrugation amplitude $h = 0.08$. Data are open circles. The single collision results are a dashed curve, the double collision a dotted curve and the results of single plus double a solid curve. Equation (2.6) was used with the single collision term, $dR^{(1)}(\mathbf{p}_f, \mathbf{p}_i)/d\Omega_f dE_f$, from the differential reflection coefficient of the combination model and in the differential reflection coefficient in the double collision term the differential reflection coefficient for the discrete model was used. Noticeable is the fact these new calculations produce a reasonable agreement for the low energy features of the data, as opposed to that of Fig. 4.1 which used the smooth surface model for both single and double collisions. It can be seen that the double collision component in Eq. (2.6) is responsible for the low energy agreement with the data. The calculated results for the sum of the single and double components in Fig. 5.3 is more narrow than in the case of Fig. 4.1, but with equally good agreement for the position of the most probable intensity.

An example of an in-plane angular scattering distribution for Ar/Ga with $\theta_i = 55^\circ$ and $E_i = 92$ kJ/mol for a surface temperature of 586 K. are shown in Fig. 5.4. The value of $v_R = 600$ m/s. Data are open circles. Theoretical calculations are the solid curve. The calculations are broader than the the data and the most probable intensity for the calculations occurs at a final angle that is approximately 10° smaller than for the data. An example of out-of-plane calculations is shown in Fig. 5.5

for Ar/Ga with $\theta_i = 55^\circ$ and $E_i = 92$ kJ/mol for a surface temperatures of

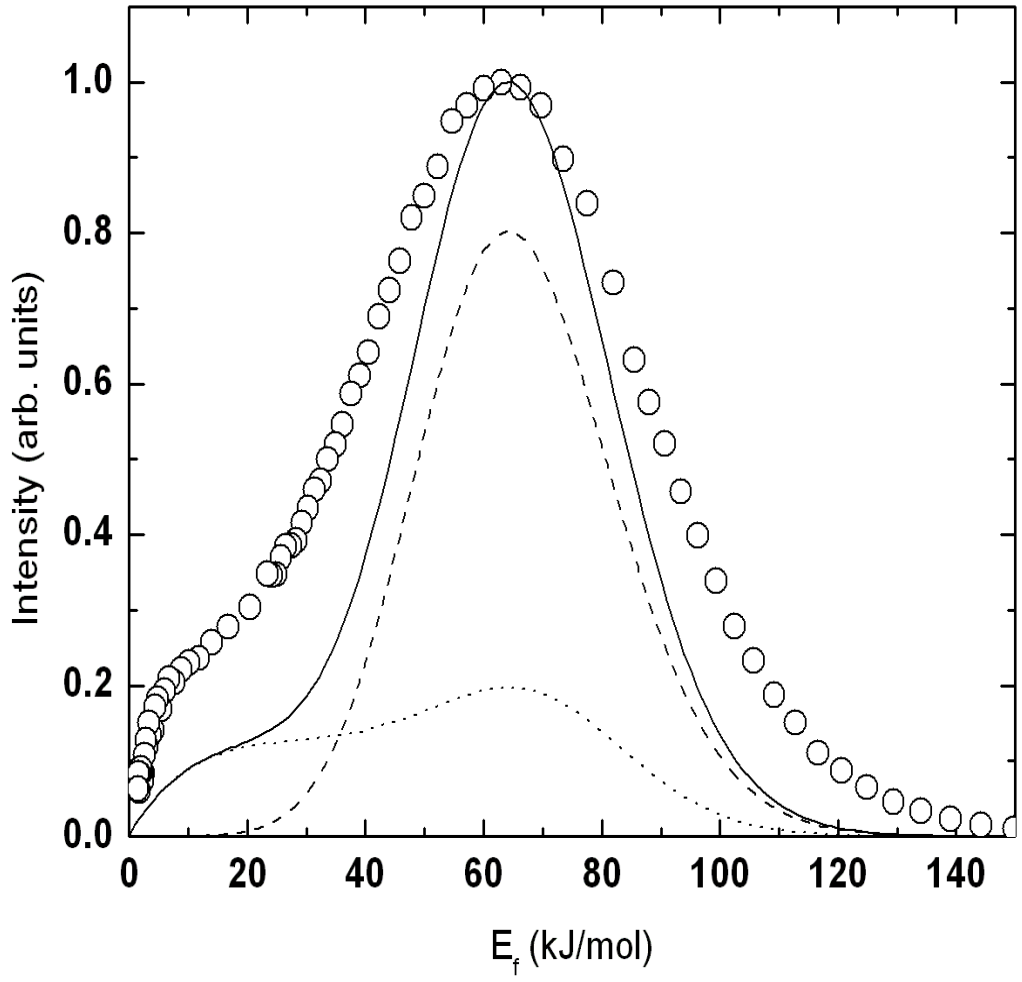

Figure 5.3: Energy-resolved spectra for Ar/Ga with double collisions for $\theta_i = \theta_f = 55°$, $E_i = 95$ kJ/mol and $T_S = 673$ K. Calculations are the solid curve for corrugation amplitude $h = 0.08$. Data are open circles. The single collision results are a dashed curve, the double collision a dotted curve and the results of single plus double the solid curve.

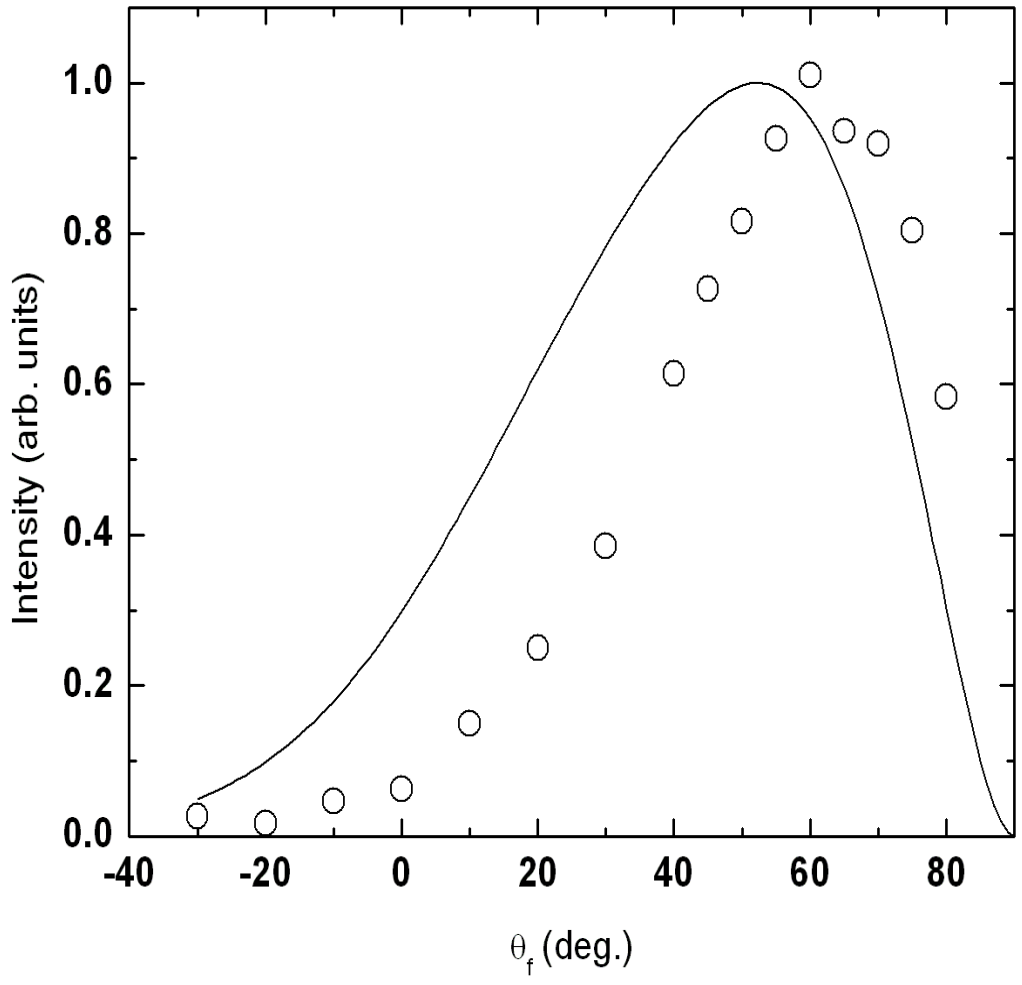

Figure 5.4: In-plane angular distribution for Ar/Ga with $\theta_i = 55°$ and $E_i = 92$ kJ/mol and $h = 0.08$ for a surface temperature of 586 K. Data are open circles. Theoretical calculations are the solid curve.

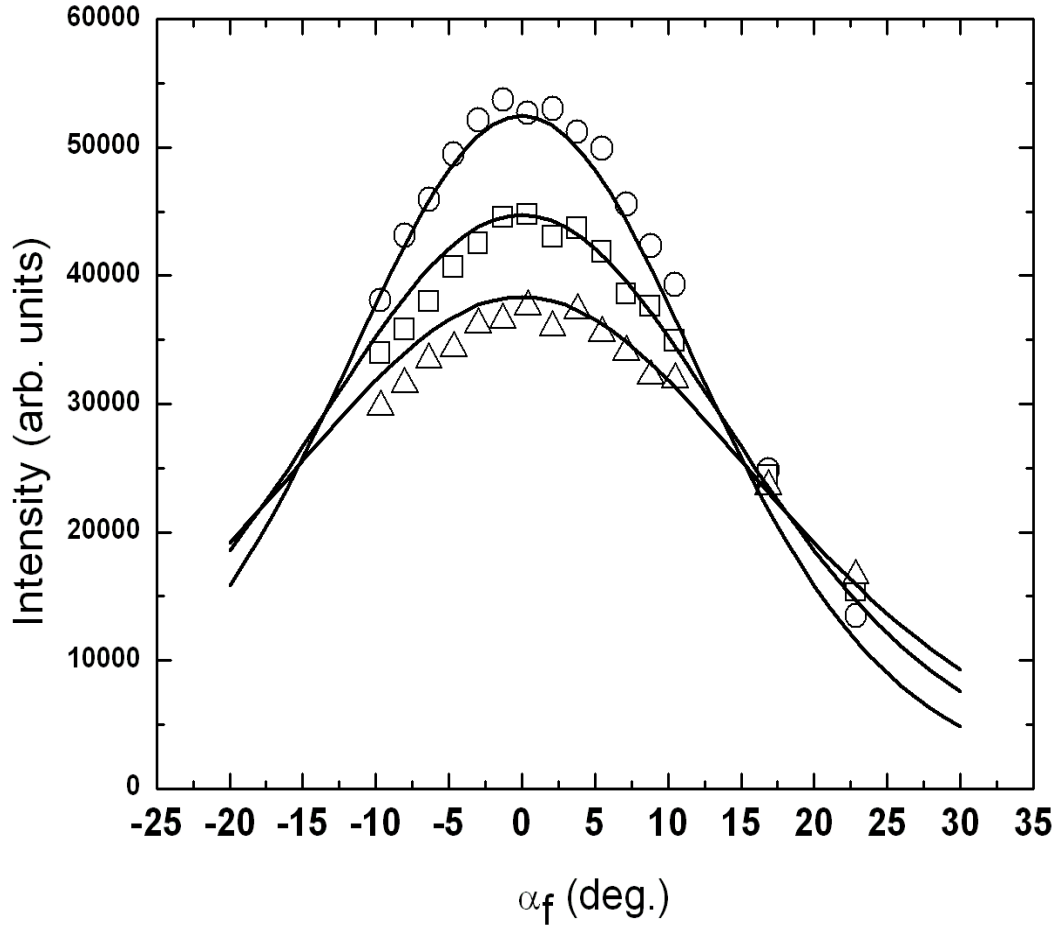

Figure 5.5: Out-of-plane angular distribution for Ar/Ga with $E_i = 92$ kJ/mol for surface temperatures of $308, 436$ and 586 K. The value of $v_R = 600$ m/s and $\theta_i = \theta_f = 55°$ and $h = 0.08$. Data are for 308 K (circles), 436 K (squares) and 586 K (triangles). Theoretical calculations are the solid curves.

308, 436 and 586 K. The value of $v_R = 600$ m/s and $\theta_i = \theta_f = 55°$. Data are open circles for surface temperature 308 K, squares for 436 K and triangles for 586 K. The theoretical calculations are solid curves. The calculations are normalized to the 436 K data. It can be seen that calculation agrees very well with the data. The calculation increases in FWHM with temperature increase, and decreases in maximum intensity as does the data.

5.3 Conclusions

In this chapter the model of Eq. (2.47) was used to examine the argon-gallium data [60]. While this data was from scattering from a liquid metal and not expected to be appropriate for analysis with the one-dimensional theory used here, it was seen to yield results in reasonable agreement even in the case of scattering from a liquid metal. It was seen that the temperature dependence of the most probable intensity of energy-resolved data may be used to estimate the surface corrugation. The peak-to-trough distance of the corrugated surface was seen to be close to the expected 10% of the interparticle spacing which is the estimate often used for the rms vibrational displacement necessary to achieve melting. The corrugation experienced by the incident atom was seen to increase with increasing incident energy, as was to be expected because the locus of classical turning points is farther from the surface for lower incident energies. Double scattering reproduced the low energy feature seen in the energy-resolved scattering data. In-plane and out-or-plane scattering agreed well with the data for reasonable values of surface corrugation amplitude.

Appendices

Appendix A Classical Rainbow Scattering in the Ar/2H-W(100) System

In the case of scattering at very low incident energies the classical turning point will be far from the surface. The corrugation experienced by the incident atom is essentially flat. Scattering will then be almost entirely specular. If the incident energy is high the atom approaches close enough to the surface to experience a significant corrugation in the locus of classical turning points. Classical elastic scattering is specular relative to the local normal. This results in classical rainbow scattering; a result of the classical mechanical interaction of incident atoms and the two-dimensional periodicity of the interaction potential. The maximum possible scattering occurs at the inflection points of the corrugated surface of the locus of classical turning points, thus making a local extremum in the scattering angle at the inflection points. Steep corrugations tend to give large maximum angles. What distinguishes classical rainbow scattering from other classical scattering phenomena is that the orientation of crystallographic directions relative to the scattering plane have a strong effect on the rainbow scattering patterns. This is similar to the case of diffraction. It goes without saying that classical rainbow scattering could be used to explore the directional-dependent properties of the surface and the interaction potential.

In studying the scattering of argon from 2H−W(100) at low beam energies and low surface temperatures, it was found that rainbow distributions appeared [128]. Recently, that same data has been analyzed using a six-parameter theory [120, 121, 122, 129]. In this appendix the two-parameter theory of Eq. (2.47) is applied to the data from the 2H−W(100) system of [128]. Good agreement is obtained for the rainbow distributions.

The geometry for the classical rainbow angle is shown in Fig. 6.

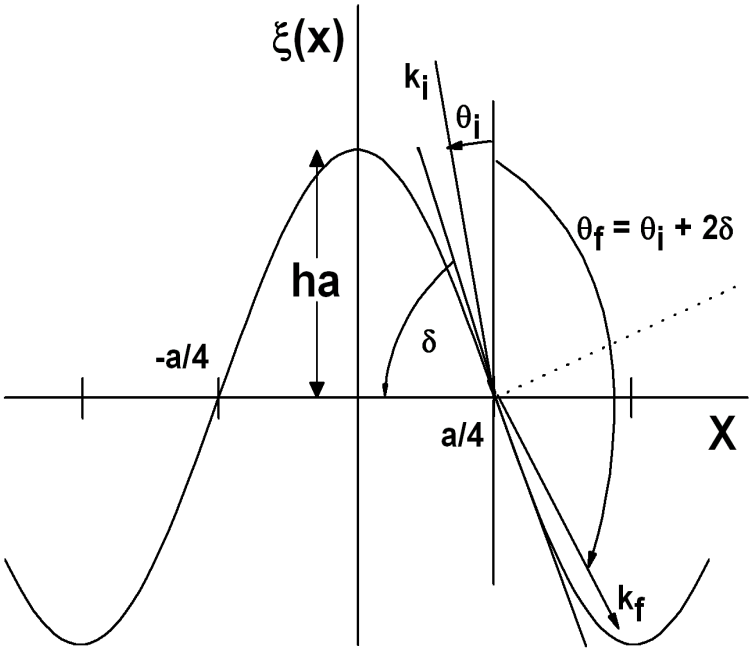

Figure 6: Geometry of the rainbow angle for a sinusoidal corrugation function. The dotted line is the local normal. The δ is the angle between the tangent line at the inflection point and the x-axis, or the angle between the surface normal and the local normal.

From this the rainbow angle is found to be:

$$\begin{aligned} \tan\delta &= \left|\frac{d\xi\,(x)}{dx}\right| \\ &= 2\pi h \\ \theta_f &= \theta_i \pm 2\delta. \end{aligned} \tag{1}$$

The rainbow angle from Eq. (1) is for purely elastic scattering. Energy transfer to or from the surface strongly affects rainbow scattering by shifting the rainbow angle and broadening the peaks in final angle resolved scattering distributions. The theory resulting in Eq. (2.47) includes the effects of energy transfer.

The dependence of the rainbow scattering upon incident energy for the 2H−W(100) system is seen in the following figures, for which the energy range is 0.065 to 220 meV. All results have been normalized to match the data peak intensity for the supraspecular rainbow. For comparison, from Eq. (1) the rainbow angles for purely elastic rainbow scattering are 10° and 49° for the subspecular rainbow and supraspecular rainbow, respectively.

In Fig. 7 it is seen that the theory, shown as a smooth curve, gives reasonable agreement with data, circles, for $E_i = 65$ meV and $\theta_i = 30°$. The corrugation amplitude is $h = 0.027$ and $v_R = 850$ m/s. Agreement for the subspecular rainbow is somewhat better than for that of the supraspecular rainbow at approximately 35° with the theoretical results being broader then the data. There appears to be a further feature at approximately 50°. In Fig. 8 it is seen that, for $E_i = 130$ meV and $\theta_i = 30°$, with corrugation amplitude $h = 0.027$ and $v_R = 850$ m/s reasonable agreement is again obtained. It is seen that the subspecular rainbow peak is more pronounced than in Fig. (7) meV and is at approximately the same $\theta_f = 20°$ as in Fig. 7. The supraspecular peak is shifted to approximately 37°. The feature at 50° is

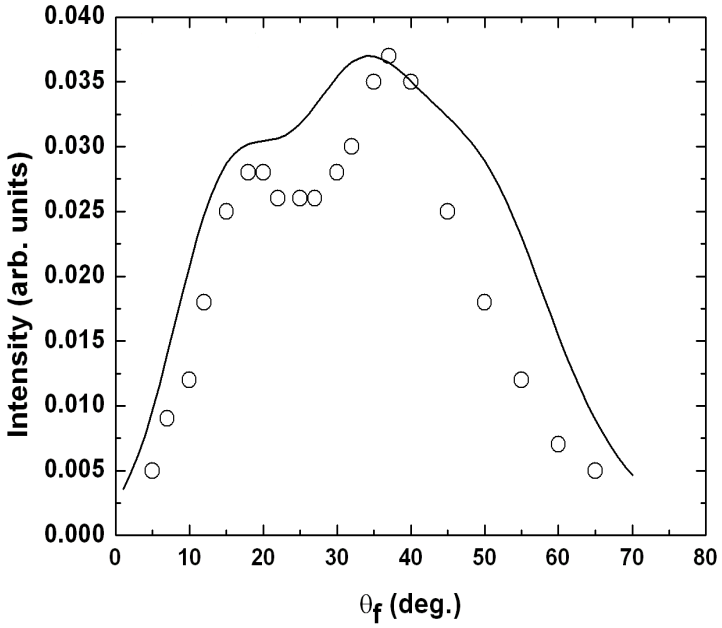

Figure 7: Rainbow scattering for the 2H−W(100) system at $E_i = 65$ meV and $\theta_i = 30°$. The corrugation amplitude is $h = 0.027$ and $v_R = 850$ m/s.

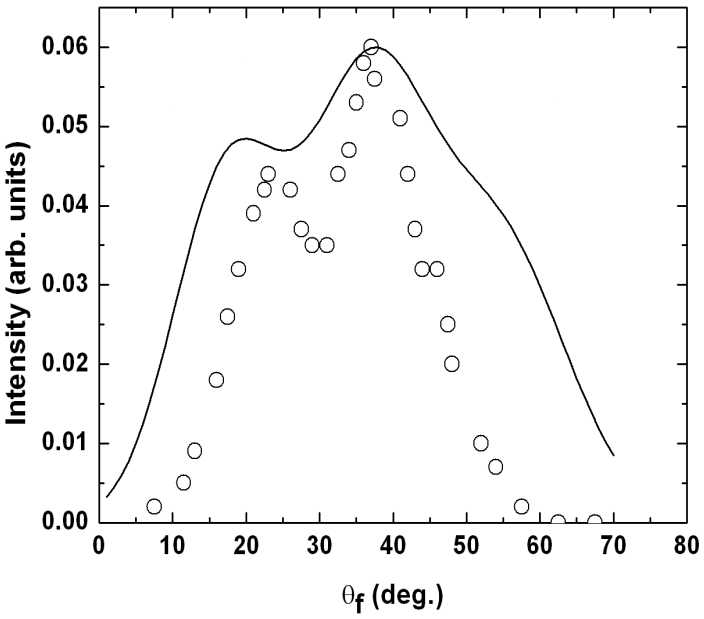

Figure 8: Rainbow scattering for the 2H−W(100) system at $E_i = 130$ meV and $\theta_i = 30°$. The corrugation amplitude is $h = 0.027$ and $v_R = 850$ m/s.

somewhat more pronounced. In Fig. 9 it is seen that, for $E_i = 220$ meV and $\theta_i = 30°$, with corrugation amplitude $h = 0.027$ and $v_R = 850$ m/s reasonable agreement is again obtained. It is seen that the subspecular rainbow peak is more pronounced than in Fig. 7 meV and is at approximately the same $\theta_f = 19°$ as compared to $\theta_f = 20°$ as in Fig. 7. The supraspecular peak is shifted to approximately 39°. The feature at 50° is yet more pronounced as compared with the lower energies. At this highest incident energy the data is much more symmetrical. It is seen that the rainbow peaks in the theory become more defined as incident energy increases. The data become more symmetrical as the incident energy increases. Theory also becomes more symmetrical with increasing energy. The calculations show a feature at approximately 50° which becomes progressively more defined as the incident energy increases. This feature is

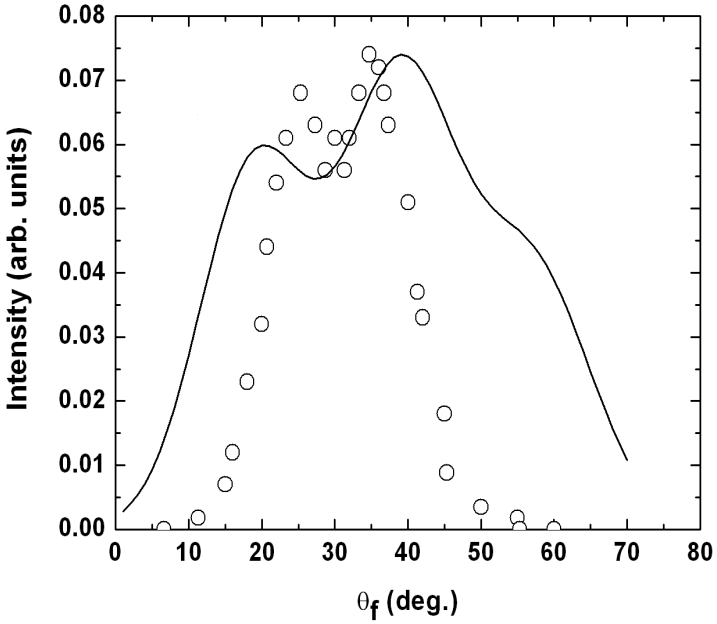

Figure 9: Rainbow scattering for the 2H−W(100) system at $E_i = 220$ meV and $\theta_i = 30°$. The corrugation amplitude is $h = 0.027$ and $v_R = 850$ m/s.

not manifest in the data.

It is of interest to examine the dependence of the theoretical calculations upon the corrugation amplitude. This is shown in Fig. 10. As the corrugation parameter, h increases the angular distribution begins as the smooth surface result and quickly begins to exhibit the rainbow features. The supraspecular rainbow peak is subtly present at $h = 0.02$ and becomes significantly more prominent as h increases and shifts toward higher final angles. The peak intensity also decreases with increasing corrugation amplitude for the supraspecular peak. The subspecular peak only begins to be seen at corrugation amplitude of 0.03 and shifts gradually toward lower final angles with increases values of h.

Also of interest, in Fig. 11 is shown an example of contributions from the several parts of the combination model. It is seen that the supraspecular rainbow peak is due to scattering from the negative slope component of Eq. (2.47) and has a lower peak intensity, while the subspecular, peak is due to the positive slope component of Eq. (2.47), which has a higher peak intensity. The smooth surface component has the highest peak intensity and has this peak intensity very near the same value of θ_i as that of the data, approximately 37°.

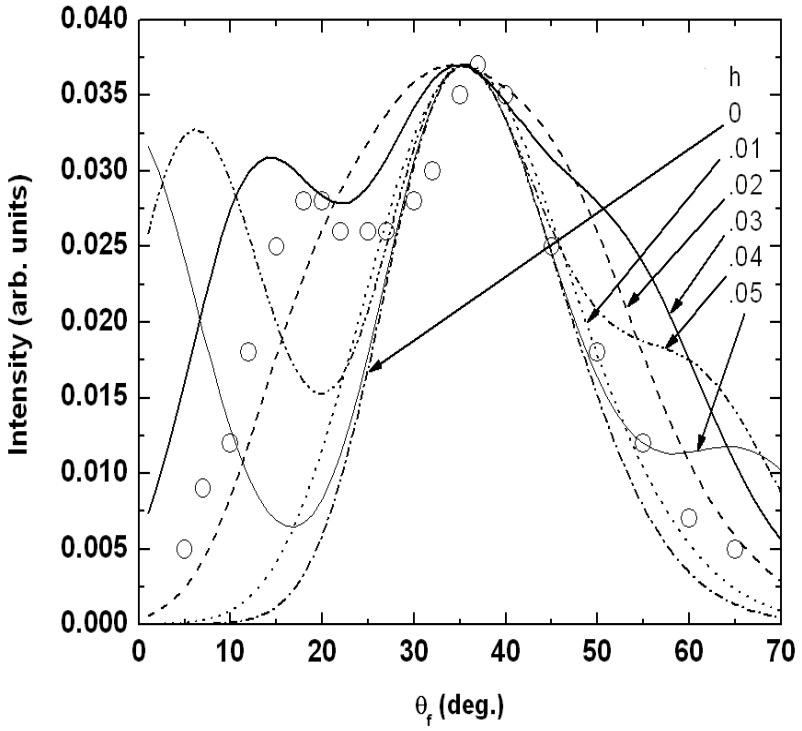

Figure 10: Rainbow scattering for the 2H−W(100) system at $E_i = 65$ meV and $\theta_i = 30°$, and $v_R = 850$ m/s for corrugation amplitude $0.0 \leq h \leq 0.05$.

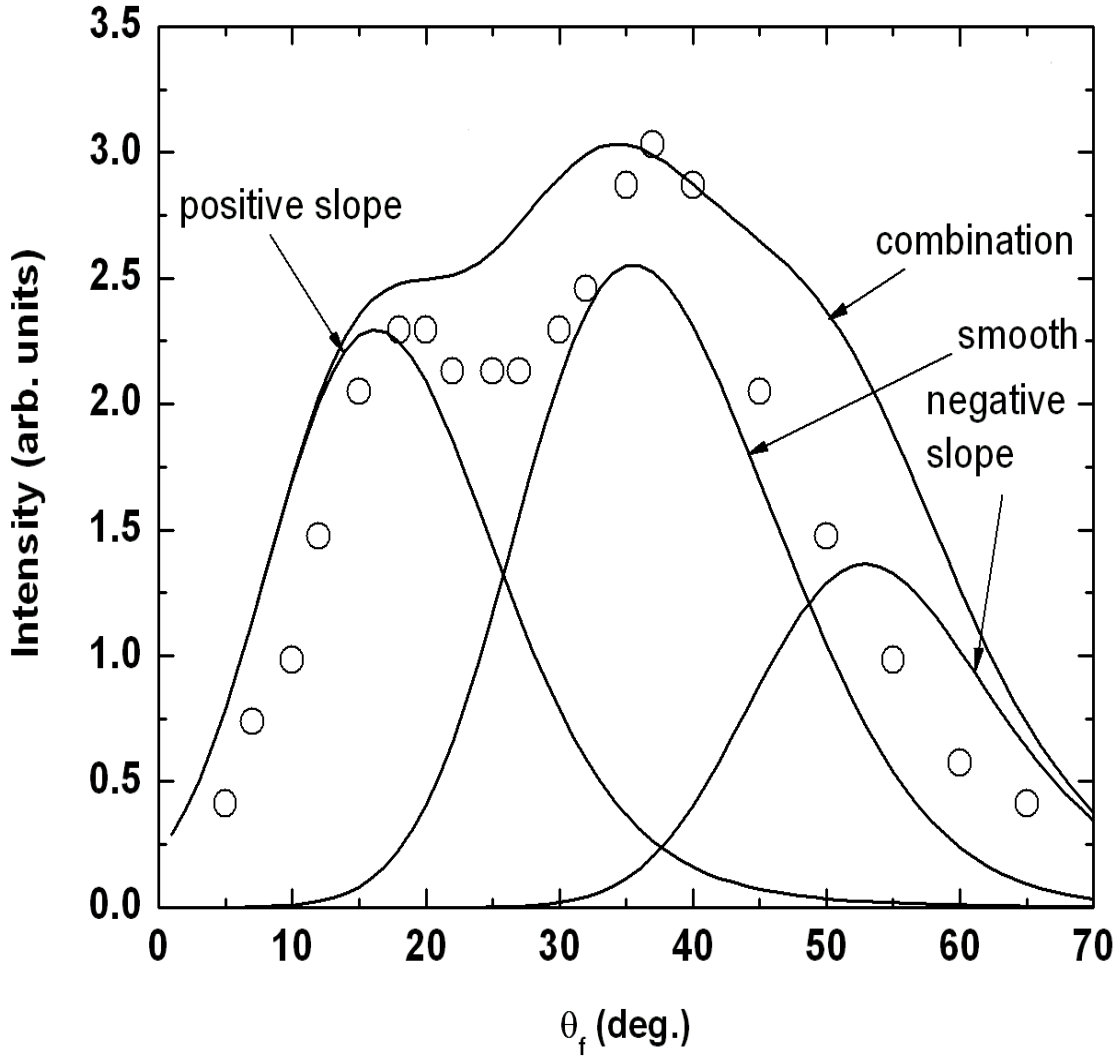

Figure 11: Rainbow scattering for the 2H−W(100) system at $E_i = 65$ meV and $\theta_i = 30°$, and $v_R = 850$ m/s for corrugation amplitude $h = 0.027$. The contributions of the three components of Eq. (2.47) are shown.

Appendix B Reduction of the Integral of Eq. (2.38)

It is possible, with the use of elementary identities and polar coordinates to reduce the integral of Eq. (2.38) to a form integrable in one of the azimuthal variables. Starting with Eq. (2.38),

$$\begin{aligned} S\left(\triangle \underline{K}\right) = \frac{1}{L^4} \int d\underline{R}_1 \int \underline{R}_2 \exp(-\imath \triangle \underline{K} \cdot (\underline{R}_1 - \underline{R}_2)) \exp(-\imath \triangle k_z [\xi \underline{R}_1) - \xi(\underline{R}_2)]) \\ \exp\left(-\alpha^2 \left(\underline{R}_1 - \underline{R}_2\right)^2\right). \end{aligned} \tag{2}$$

Transforming to polar coordinates gives

$$\begin{aligned} S\left(\triangle K\right) = \frac{1}{L^4} \int_0^{\frac{a}{2}} dR_1 \int_0^{\frac{a}{2}} dR_2 R_1 R_2 \int_0^{2\pi} d\phi_1 \int_0^{2\pi} d\phi_2 \exp\left[\imath \left(-\triangle K R_1 \cos\left(\phi_1\right)\right) + \triangle K R_2 \cos\left(\phi_2\right)\right] \\ \exp(-\imath \triangle k_z [\xi\left(\underline{R}_1\right) - \xi\left(\underline{R}_2\right)]) \\ \exp\left(-\alpha^2 \left(R_1^2 + R_2^2 - 2R_1 R_2 \cos\left(\phi_1 - \phi_2\right)\right)\right). \end{aligned} \tag{3}$$

Using the identity

$$\cos(\phi_1 - \phi_2) = \cos(\phi_1)\cos(\phi_2) + \sin(\phi_1)\sin(\phi_2) \tag{4}$$

results in

$$\begin{aligned} S\left(\triangle K\right) = \frac{1}{L^4} \int_0^{\frac{a}{2}} dR_1 \int_0^{\frac{a}{2}} dR_2 R_1 R_2 \int_0^{2\pi} d\phi_2 \exp\left(-\alpha^2 \left(R_1^2 + R_2^2\right)\right) \\ \exp\left(\imath \triangle K R_2 \cos\left(\phi_2\right)\right) \\ \int_0^{2\pi} d\phi_1 \exp\left(2\alpha^2 R_1 R_2 \left(\cos\left(\phi_1\right)\cos\left(\phi_2\right) + \sin\left(\phi_1\right)\sin\left(\phi_2\right)\right)\right) \\ \exp\left(-\imath\ \triangle K R_1 \cos\left(\phi_1\right)\right). \end{aligned} \tag{5}$$

Using the identity

$$\exp\left(-\imath\triangle K R_1\cos\left(\phi_1\right)\right)=\cos\left(\triangle K R_1\cos\left(\phi_1\right)-\imath\sin\left(\triangle K R_1\cos(\phi_1)\right)\right., \tag{6}$$

leads to

$$\begin{aligned}S\left(\triangle K\right)=\frac{1}{L^4}\int_0^{\frac{a}{2}}dR_1\int_0^{\frac{a}{2}}dR_2R_1R_2\int_0^{2\pi}d\phi_2\exp\left(-\alpha^2\left(R_1^2+R_2^2\right)\right)\exp\left(\imath\ \triangle K R_2\cos\left(\phi_2\right)\right)\\ \int_0^{2\pi}d\phi_1\exp\left(2\alpha^2R_1R_2\left(\cos\left(\phi_1\right)\cos\left(\phi_2\right)+\sin\left(\phi_1\right)\sin\left(\phi_2\right)\right)\right)\\ \left(\cos\left(\triangle K R_1\cos\phi_1\right)-\imath\sin\left(\triangle K R_1\cos\phi_1\right)\right).\end{aligned} \tag{7}$$

The azimuthal angular integral over $d\phi_1$ may be calculated by use of known results [130] to obtain an integral over modified Bessel functions of complex argument:

$$\begin{aligned}S\left(\triangle K\right)=\int_0^{\frac{a}{2}}dR_1\int_0^{\frac{a}{2}}dR_2R_1R_2\int_0^{2\pi}d\phi_2\exp\left(-\alpha^2\left(R_1^2-R_2^2\right)\right)\\ \exp\left(\imath\triangle k_z2\pi h\left(R_1-R_2\right)\right)\exp\left(\imath\left(\triangle K R_2\cos\left(\phi_2\right)\right)\right)\\ \Big\{I_0\big(\sqrt{4\alpha^2R_1^2R_2^2-\triangle K^2R_1^2+\imath4\triangle K\alpha^2R_1^2R_2\cos\phi_2}\big)\\ -I_0\big(\sqrt{4\alpha^2R_1^2R_2^2-\triangle K^2R_1^2-\imath4\triangle K\alpha^2R_1^2R_2\cos\phi_2}\big)\\ +I_0\big(\sqrt{4\alpha^2R_1^2R_2^2-\triangle K^2R_1^2+\imath4\triangle K\alpha^2R_1R_2^2\cos\phi_2}\big)\\ -I_0\big(\sqrt{4\alpha^2R_1^2R_2^2-\triangle K^2R_1^2-\imath4\triangle K\alpha^2R_1R_2^2\cos\phi_2}\big)\Big\}.\end{aligned} \tag{8}$$

Bibliography

[1] D. Tabor. *J. Colloid Interface Sci.*, **75**:240, 1980.

[2] M. Faraday. *Experimental Researches in Chemistry and Physics*. Richard Taylor and William Francis, 1859.

[3] M. Bergstein, J.F. Rinke, and C.M. Gutheil. *Phys. Rev.*, **36**:587, 1930.

[4] J.W. Orton. *Theory of Semi-Conductors*. Oxford, New York, USA, 2004.

[5] J.W. Gibbs. *The Colleted Works of J. Willard Gibbs, vol. 1*. Longmans, Green and Co., New York, USA, 1928.

[6] J.C. Maxwell. In W.D. Niven, editor, *Scientific Papers of J.C. Maxwell*, page 706. Dover, 1952.

[7] O. Stern. *Naturwissenshaften*, **17**:391, 1929.

[8] I. Easterman and O. Stern. *Zeitschrift fur Physik*, **61**:95, 1930.

[9] I. Easterman, R. Frisch, and O. Stern. *Zeitschrift fur Physik*, **73**:348, 1931.

[10] R. Frisch and O. Stern. *Zeitschrift fur Physik*, **84**:430, 1933.

[11] T.H. Johnson. *J. Franklin Inst.*, **210**:135, 1930.

[12] T.H. Johnson. *Phys. Rev.*, **37**:847, 1931.

[13] J.K. Roberts. *Proc. Roy. Soc.*, **A129**:146, 1930.

[14] J.M. Jackson and N.F. Mott. *Proc. Soc. London. A*, **137**:703, 1932.

[15] J.E. Lennard-Jones and A.F. Devonshire. *Proc. Roy. Soc. Lond. A*, **158**:253, 1937.

[16] I. Langmuir. *Phys. Rev.*, **8**:149, 1916.

[17] I. Langmuir. *J. Amer. Chem. Soc.*, **40**:1361, 1918.

[18] I. Langmuir. *Trans. Faraday Soc.*, **17**:111, 1921.

[19] J.E. Lennard-Jones and C. Strachan. *Proc. Roy. Soc. Lond. A*, **163**:132, 1937.

[20] J. Bardeen. *Phys. Rev.*, **49**(9):653, 1936.

[21] N.F. Mott. *Proc. Camb. Phil. Soc.*, **34**:221, 1938.

[22] B. Davydov. *J. Phys. USSR*, **1**:167, 1939.

[23] W. Schottky. *Z. Physik*, **113**:367, 1939.

[24] C.B. Duke. *J. Vac. Sci. Technol. A*, **21**:S34, 2003.

[25] C.B. Duke and R.L. Park. *Physics Today*, **25**:23, 1972.

[26] E.K. Schweizer, t.t. Rettner, and S, Holloway. *Surface Science*, **249**:335, 1971.

[27] B. Webb and M.G. Legally. *Solid State Physics*, **28**:301, 1973.

[28] M. von Laue. *Physikalische Zeitschrift*, **14**:421, 1913.

[29] W.L. Bragg. *Proc. Cambridge Phil. Soc.*, **17**:37, 1912.

[30] P.M. Chaiken and T.C. Lubensky. Cambridge, Cambridge, UK, 1995.

[31] T. Scopigno, U. Balucani, G. Roucco, and F. Sette. *J. Phys.: Condens. Matter*, **12**:8009, 2000.

[32] C.B. Duke. *Surface Science: The First Thirty Years*. North Holland, 1994.

[33] J.M. Jackson and N.F. Mott. *Proc. Soc. London. A*, **137**:703, 1932.

[34] J.M. Jackson. *Proc. Camb. Phil. Soc.*, **28**:136, 1932.

[35] J.P. Toennies. In *Vol. 21 Springer Series in Surface Sciences*, page 111, Heidelberg, August 1991. Springer-Verlag.

[36] C.A. DiRubio, D.M Goodstein, B.H. Cooper, and K. Burke. *Phys. Rev. Lett.*, **73**:2768, 1994.

[37] C.T. Rettner, J.A. Barker, and D.S. Bethune. *Phys. Rev. Lett.*, **67**:2183, 1991.

[38] B. Feuerbacher. In *Vol. 21 Springer Series in Chemical Physics*, page 267, Berlin, August 1991. Springer-Verlag.

[39] A. Sjölander. *Ark. Fys.*, **14**:315, 1959.

[40] J.C. Tully. *Surf. Sci.*, **111**:461, 1981.

[41] M.H. Shapiro and T.A. Tombrello. *Nucl. Int. Methods Phys. Res. B*, **90**:277, 1995.

[42] M.T. Robinson. *K. Dan. Vidensk. Selsk. Mat. Fys. Medd.*, **43**:27, 1983.

[43] D.E. Harrison and M.M. Jackas. *Nucl. Int. Methods Phys. Res. B*, **15**:25, 1986.

[44] D.A. Micha. *J. Chem. Phys.*, **74**:2054, 1981.

[45] R. Brako and D.M. Newns. *Phys. Rev. Lett.*, **48**:1859, 1982.

[46] R. Brako and D.M. Newns. *Surf. Sci.*, **123**:439, 1982.

[47] H.D. Meyer and R.D. Levine. *Chem. Phys.*, **85**:189, 1984.

[48] J.R. Manson. *Phys. Rev. B*, **43**:6924, 1991.

[49] A. Muis and J.R. Manson. *Phys. Rev. B*, **54**:2205, 1996.

[50] J. Powers, J.R. Manson, C.E. Sosolik, J.R. Hampton, A.C. Lavery, and B.H. Cooper. *Phys. Rev. B*, **70**:115413, 2004.

[51] A. Muis and J.R. Manson. *J. Chem. Phys.*, **107**:1655, 1997.

[52] A. Muis and J.R. Manson. *J. Chem. Phys.*, **111**:730, 1999.

[53] M. Bertino, J.R. Manson, and W. Silvestri. *J. Chem. Phys.*, **108**:10239, 1998.

[54] F. Hoffman, J.P. Toennies, and J.R. Manson. *J. Chem. Phys.*, **106**:1234, 1997.

[55] J. Dai and J.R. Manson. *J. Chem. Phys.*, **119**:9842, 2003.

[56] F. Hoffman, J.P. Toennies, and J.R. Manson. *Surf. Sci. Lett.*, **349**:184, 1996.

[57] W.W. Hayes and J.R. Manson. *Phys. Rev. B*, **74**:07413–1, 2006.

[58] V. Celli, G. Benedek, U. Harten, J. P. Toennies, R. B. Doak, and V. Bortolani. *Surf. Sci.*, **143**:376, 1984.

[59] W.R. Ronk, D.V. Kowalski, M. Manning, and G.M. Nathanson. *J. Chem. Phys.*, **104**:4842, 1996.

[60] Michelle Manning, Jason A. Morgan, David J. Castro, and Gilbert M. Nathanson. *J. Chem. Phys.*, **119**:12593, 2003.

[61] T. Tomii, T. Kondo, T. Hiraoka, T. Ikeuchi, S. Yagu, and S. Yamamoto. *J. Chem. Phys.*, **112**:9052, 2000.

[62] T. Kondo, T. Sasaki, and S. Yamamoto. *J. Chem. Phys.*, **118**:760, 2003.

[63] I. Moroz and J. R. Manson. *Phys. Rev. B*, **69**:205406, 2004.

[64] I Moroz and J. R. Manson. *Phys. Rev. B*, **71**:113405, 2005.

[65] Guoqing Fan and J.R. Manson. *Phys. Rev. B*, **79**:045424, 2009.

[66] Guoqing Fan and J.R. Manson. *J. Chem. Phys.*, **130**:064703, 2009.

[67] Guoqing Fan and J.R. Manson. *Phys. Rev. Lett.*, **79**:063202, 2008.

[68] Guoqing Fan and J.R. Manson. *Phys. Rev. B*, **79**:085413, 2005.

[69] J.R. Manson. *Phys. Rev. B*, **78**:155408, 2008.

[70] G. Baym. *Lectures on Quantum Mechanics*. Benjamin/Cummings, Reading, USA, 1981.

[71] P.A.M. Dirac. *Proc. Soc. London. A*, **114**:243, 1927.

[72] L. Van Hove. *Phys. Rev.*, **95**:249, 1954.

[73] R. Glauber. *Phys. Rev.*, **98**:1692, 1955.

[74] V. Bartolani and A.C. Levi. *Riv. Nuovo Cimento*, **9**:1, 1986.

[75] J.W. Strutt(Lord Rayleigh). *Proc. Roy. Soc. Lond., Ser. A*, **79**:399, 1907.

[76] A.A. Maradudin, E.W. Montroll, and G.H. Weiss. *Theory of Lattice Dynamics in the Harmonic Approximation*. Academic, New York, USA, 1963.

[77] John P. McKelvey. *Solid State and Semiconductor Physics*. Harper and Row, New York, USA, 1966.

[78] R. Brako and D.M. Newns. *Surf. Sci.*, **48**:1859, 1982.

[79] J.R. Manson. *Phys. Rev. B*, **58**:2253, 1998.

[80] J. Braun, K.L. Kostov, G. Witte, L. Surnev, J.G. Skofronick, S.A. Safron, and Ch. Wöll. *Surf. Sci.*, **372**:132, 1997.

[81] D.A. Butler, B. Berenbak, S. Solte, and A.W. Kleyn. *Phys. Rev. Lett.*, **78**:4653, 1997.

[82] B. Berenbak, S. Zboray, B. Riedmuller, D.C. Papageorgopoulos, S. Solte, and A.W. Kleyn. *Phys. Chem. Chem. Phys.*, **4**:68, 2002.

[83] B. Berenbak. PhD thesis, Vrije Universiteit, Amsterdam, 2000.

[84] A. Raukema, A.P. de Jongh, H.P. Alberda, R. Boddenberf, E. de Haas, H. Neerings A.W. Kleyn, R. Schafsma, and H Veerman. *Meas. Sci. Technol.*, **8**:9253, 1997.

[85] W.W. Hayes and J.R. Manson. *Phys. Rev. B*, **75**:113408–1, 2007.

[86] W.W. Hayes and J.R. Manson. *Phys. Rev. B*, **77**:089904–1, 2008.

[87] W.W. Hayes, H. Ambaye, and J.R. Manson. *J. Phys.: Condens. Matter*, **19**:305007–1, 2007.

[88] W.W. Hayes, H. Ambaye, and J.R. Manson. *J. Phys.: Condens. Matter*, **19**:376203–1, 2007.

[89] M. Mortensen, E. Jensen, L. Diekhöner, A. Baurichter, A.C. Luntz, and V.V. Perunin. *J. Chem. Phys.*, **118**:11200, 2003.

[90] H. Ambaye and J.R. Manson. *J. Chem. Phys.*, **125**:084717, 2006.

[91] M.J. Regan, E.W. Kawamoto, S. Lee, P.S. Pershan, M. Maskil, M. Deutsch, O.M. Magnussen, B. Ocko, and L.E. Berman. *Phys. Rev. Let.*, **75**:2498, 1995.

[92] E. Hulpke. *Helium Atom Scattering*. Springer-Verlag, Heidelberg, 1992.

[93] R.H. Rieder, G. Parshau, and B. Burg. *Phys. Rev. Lett.*, **71**:1059, 1993.

[94] U. Balucani and M. Zoppi. *Dynamics of the Liquid State*. Oxford, New York, USA, 1983.

[95] J. Maxwell. *Philos. Trans. R. Soc. London*, **156**:249, 1866.

[96] J. Maxwell. *Philos. Trans. R. Soc. London*, **157**:49, 1867.

[97] T. Scopigno, G. Roucco, and F. Sette. *Rev. Mod. Phys.*, **77**:881, 2005.

[98] E.B. Flom, Z. Cai, A. Acero, B. Lin, N. Maskil, and S.A. Rice. *J. Chem. Phys.*, **96**:4743, 1993.

[99] N. Lei, Z. Huang, and S.A. Rice. *J. Chem. Phys.*, **104**:4802, 1996.

[100] H. Tostmann, E. DiMasi, P. Pershan, B. Osko, O.G. Shpyrko, and M. Deutsch. *Phys. Rev. B*, **59**:783, 1999.

[101] D. Chase, M. Manning, J.A. Morgan, G.M. Nathanson, and R. Benny Gerber. *J. Chem. Phys.*, **104**:4842, 1996.

[102] Mackenzie E. King, Mary E. Saecker, and Gilbert M. Nathanson. *J. Chem. Phys.*, **101**:2539, 1994.

[103] L. Tribe, M. Manning, J. Morgan, M. D. Stephens, W.R. Ronk, E. Treptow, G. Nathanson, and J.L. Skinner. *J. Phys. Chem.*, **102**:206, 1998.

[104] W.W. Hayes and J.R. Manson. *J. Chem. Phys.*, **127**:164714–1, 2007.

[105] A.R. Miedema and B.E. Nieuwenhuys. *Surf. Sci.*, **104**:491, 1981.

[106] Gianfranco Vidali, G. Ihm, Hye-Young Kim, and Milton W. Cole. *Surf. Sci. Rep.*, **12**:133, 1991.

[107] H. Schlichting, D. Menzel, T. Bruner, and W.Brenig. *J. Chem. Phys.*, **97**:4453, 1992.

[108] Jason A. Morgan and G. Nathanson. *J. Chem. Phys.*, **114**:1958, 2001.

[109] H. Ambaye and J.R. Manson. *J. Chem. Phys.*, **125**:084717, 2006.

[110] D. Chase, M. Manning, J. Morgan, G. Nathanson, and R. Benny Gerber. *J. Chem. Phys.*, **113**:9279, 2000.

[111] R.M. Logan and R.E. Stickney. *J. Chem. Phys.*, **44**:195, 1966.

[112] R.M. Logan and J.C. Keck. *J. Chem. Phys.*, **49**:860, 1968.

[113] F.O. Goodman. *J. Phys. Chem. Solids*, **26**:85, 1965.

[114] W.L. Nichols and J.H. Weare. *J. Chem. Phys.*, **62**:3754, 1975.

[115] W.L. Nichols and J.H. Weare. *J. Chem. Phys.*, **66**:1075, 1977.

[116] J.D. Doll. *J. Chem. Phys.*, **59**:1038, 1973.

[117] G.O. Sitz, A.C. Kummel, R.N. Zare, and J.C. Tully. *J. Chem. Phys.*, **89**:2572, 1988.

[118] John C. Tully. *J. Chem. Phys.*, **92**:680, 1990.

[119] Tianying Yan, William L. Hasse, and John C. Tully. *J. Chem. Phys.*, **120**:1031, 2004.

[120] Eli Pollack, Santanau Sengupta, and Slavador Miret-Artés. *J. Chem. Phys.*, **129**:054107, 2008.

[121] Eli Pollack and Slavador Miret-Artés. *J. Chem. Phys.*, **130**:194710, 2009.

[122] Eli Pollack and Jörg Tatchen. *Phys. Rev. B*, **80**:115404, 2009.

[123] Mackenzie E. King, Gilbert.M. Nathanson, Mark A. Hanning-Lee, and Timothy K. Minton. *Phys. Rev Lett.*, **70**:1026, 1993.

[124] N. Lipkin, R.B. Gerber, N. Moiseyev, and G.M. Nathanson. *J. Chem. Phys.*, **100**:8408, 1994.

[125] David Pines. *Elementary Excitations in Solids*. W. A. Benjamin, Inc., New York, USA.

[126] F. Lindemann. *Phys. Z.*, **11**:609, 1910.

[127] A.C. Lawson. *Phil. Mag.*, **89**:1757, 2009.

[128] E.K. Schweizer, C.T. Rettner, and S. Holloway. *Surf. Sci.*, **249**:335, 1991.

[129] Eli Pollack, Jeremy M. Moix, and Slavador Miret-Artés. *Phys. Rev. B*, **80**:165420, 2009.

[130] I.S. Gradshteyn and I.M. Ryzhik. *Table of Integrals, Series and Products*, page 488. Academic, 1980.